Variable-delay Polarization Modulators for the CLASS Telescopes

by

Kathleen M. Harrington

A dissertation submitted to The Johns Hopkins University

in conformity with the requirements for the degree of

Doctor of Philosophy

Baltimore, Maryland

July 2018

Abstract

The search for inflationary primordial gravitational waves and the measurement of the optical depth to reionization, both through their imprint on the large angular scale correlations in the polarization of the cosmic microwave background (CMB), has motivated the creation of the Cosmology Large Angular Scale Surveyor (CLASS). CLASS is a four telescope array sited in the Chilean Atacama desert, specifically designed to achieve the sensitivity and stability necessary to observe the CMB large angular scale polarization from the ground. One of the most unique aspects of the CLASS design is a front-end variable-delay polarization modulator (VPM) that uses a wire grid in front of a movable mirror to rapidly modulate the incoming polarization and enable a "lock-in" style measurement of polarization from the sky. This thesis covers the design, fabrication, and performance of the VPMs for the CLASS telescopes as well as theoretical modeling of the polarization modulation by the VPM and analysis techniques for the resulting detector timestreams.

Primary Reader: Tobias A. Marriage

Secondary Reader: Charles L. Bennett

Acknowledgments

First, I would like to thank Toby Marriage for the time, effort, and care he has put into advising me and guiding my grad school career. Your dedication to your students is inspiring and I look forward to continuing to work with you in the future. I'd also like to thank Chuck Bennett, Dave Chuss, and Joseph Eimer for their advise and support throughout the years; you all have always been happy to talk about science or life and truly appreciate everything you've done for me.

To the rest of the CLASS group, thank you for the fun, hard work, and camaraderie. CLASS is made of an amazing group of people who care about good science and each other, I will miss the lab and site shenanigans. Joseph C. and Matthew, thanks for all your help getting the VPMs going and good luck on the next ones!

All of my friends here at JHU, especially Devin, Alex, Schuyler, Rachael, Carolyn, Zhilei, Duncan and Raymond, thank you for the laughs, companionship, parties, and support. You all kept me sane and happy.

On the money side, I'd to thank the NASA Space Technology Research Fellowship that has funded me throughout the last four years of grad school, the opportunities this fellowship afforded me has significantly impacted my career and this work.

Table of Contents

List of Tables

List of Figures

Chapter 1

Cosmology

1.1 The ΛCDM Universe

The standard model of cosmology, called ΛCDM , describes the evolution of a homogeneous and isotropic universe made of dark energy, dark matter, radiation, and baryonic matter. In ΛCDM , the assumptions of homogeneity and isotropy are combined with the contents of the universe and applied to general relativity to derive the time evolution of the universe. This derivation starts with Einstein's field equation:

$$R_{\mu\nu} - \frac{1}{2} g_{\mu\nu} R = \frac{8\pi G}{c^4} T_{\mu\nu} \tag{1.1}$$

where the left side of the equation depends solely on $g_{\mu\nu}$, the metric describing homogeneous and isotropic spacetime, and its derivatives. The right side of the equation contains the stress-energy tensor that describes the energy and matter in the universe. The stress-energy tensor consists of contributions from dark energy, dark matter, baryonic matter, and radiation. In order to describe the expansion of the universe, a scale factor $a(t)$ is defined such that the spacetime metric for a

homogeneous and isotropic universe is

$$ds^2 = -c^2dt^2 + a^2(t)\delta_{ij}dx^i dx^j. \tag{1.2}$$

With this metric, $a(t)$ parameterizes the size of the universe as a function of time.

Plugging the metric from equation 1.2 into the left side of equation 1.1 and the contents of the universe, the ith component of which is described by energy density ϵ_i and momentum p_i, into the right side of equation 1.1 leads to the Friedmann equations:

$$\left(\frac{\dot{a}}{a}\right)^2 = \frac{8\pi G}{3c^2}\sum_i \epsilon_i - \frac{kc^2}{a^2} \tag{1.3}$$

$$\frac{\ddot{a}}{a} = -\frac{4\pi G}{3}\sum_i \left(\epsilon_i + \frac{3p_i}{c^2}\right). \tag{1.4}$$

Here, k is the curvature of the universe. All measurements to date have indicated that the universe is flat ($k = 0$) with $H = \frac{\dot{a}}{a} > 0$. H is the Hubble parameter that describes the rate of expansion of the universe, the fact that it is positive indicates a is increasing with time and the universe is expanding.

In cosmological work, the different types of energy and matter are distinguished by how their energy density is related to their pressure, $p = w\epsilon$. For dark energy[1], non-relativistic matter and relativistic matter $w = -1, 0$, and $1/3$, respectively. Using the two Friedmann equations, the variation of the energy density of the various contents of the universe with respect to the scale factor can be calculated as

$$\epsilon_i = \epsilon_{0,i} a^{-3(w_i+1)}. \tag{1.5}$$

[1]Dark energy in this setup is assumed to be a "cosmological constant" where $w = -1$. There are extensions to standard ΛCDM where the energy density of dark energy varies with time or scale factor.

The density of universe and its contents are often parameterized by the critical density, ϵ_c, the density which would result in a flat universe at a particular point in time,

$$\Omega_i = \frac{\epsilon_i}{\epsilon_c} \quad \text{where} \quad \epsilon_c = \frac{3H^2}{8\pi G}. \tag{1.6}$$

Figure 1.1 shows how the contents of the universe have varied as a function of scale factor and redshift, z ($z + 1 = 1/a$). The earliest times of the universe were radiation dominated, where the vast majority of the energy density was in the form of radiation (Ω_γ) and neutrinos (Ω_ν). The universe during this era was a hot, dense plasma where photons and elementary particles were in thermal equilibrium.

As the universe expands, the density of radiation falls as a^{-4} and the density of matter falls as a^{-3}, so matter, consisting of baryons (Ω_b) and cold dark matter (Ω_c) surpasses radiation and begins to dominate the universe at an age of about 47,000 years. The temperature also as the universe expands, so that after 378,000 years the universe cools enough for the protons and electrons to combine into neutral hydrogen, a period known as recombination. The universe remains largely neutral until the first stars and galaxies ignite and reionize the universe beginning when the universe is about 500 million years old. At $t \sim 10$ Gyr, dark energy (Ω_Λ), which has a constant energy density, begins to dominate the energy content of the universe, causing the expansion of the universe to accelerate.

The ΛCDM model of the universe fits remarkably well with observations and no extensions to the model have been found to be required. Observations of the cosmic microwave background (CMB, section 1.3,Planck Collaboration et al. (2016a)), baryon acoustic oscillations (Ata et al., 2018), and local measurements of the Hubble parameter (Riess et al., 2016) all favor a flat universe that is currently dominated by

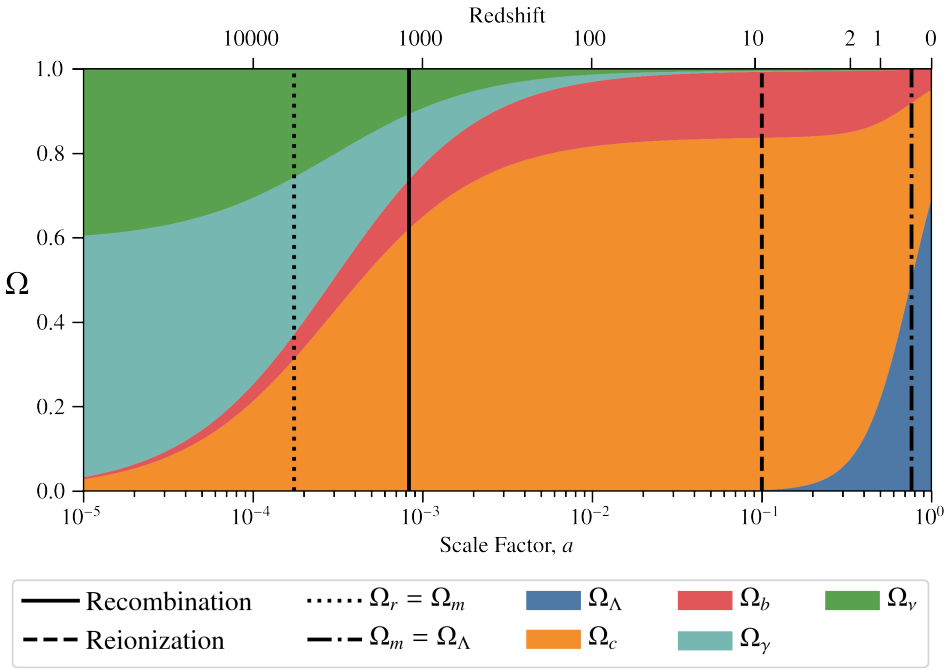

Figure 1.1: The fractional content of the universe as a function of the scale factor and redshift. Time also increases from left to right on this plot. Ω_γ, Ω_ν, Ω_c, Ω_b, and Ω_Λ mark the energy density as a fraction of the critical density of the radiation, neutrinos, cold dark matter, baryons, and dark energy, respectively. Vertical lines mark the time periods of recombination, when protons and electrons combined to form neutral hydrogen, reionization, when the first stars and galaxies reionized that neutral hydrogen, and the periods of matter-radiation equality and matter-dark energy equality. Created using the Astropy software package (The Astropy Collaboration et al., 2018).

dark energy and dark matter. However, ΛCDM does not require a specific set of initial conditions for the universe, nor does it explain the flatness, homogeneity, and isotropy of the universe. These mysteries are left to other theories to describe; the most compelling of these theories is Inflation.

1.2 Theory of Inflation

Inflation is a postulated period of time in the early universe where an excited scalar field causes the universe to expand at an exponential rate, $a \propto e^{Ht}$ (Guth, 1981; Linde, 1982; Albrecht et al., 1982). If this period of inflation lasts long enough, a volume of space smaller than an atom could expand to encompass the entirety of the observable universe. This exponential expansion explains the homogeneity and isotropy observed in the universe today by providing a mechanism for the entire observable universe to have once been in causal contact. This exponential expansion also explains the flatness of the universe, because expansion as $a \propto e^{Ht}$ drives the curvature of the universe to zero.

Inflation also predicts and explains the initial conditions of the ΛCDM universe. Observations by WMAP (Hinshaw et al., 2013), Planck (Planck Collaboration et al., 2016a), and many other experiments point to a nearly scale-invariant scalar perturbations as the initial conditions to ΛCDM evolution. These perturbations would be produced by quantum fluctuations of spacetime during inflation which are "frozen" into space by the exponential expansion of the universe. These quantum fluctuations would produce perturbations on the spacetime metric as

$$ds^2 = -c^2dt^2 + h_{ij}dx^i dx^j \quad h_{ij} = a^2(t)[e^{2\zeta}\delta_{ij} + \gamma_{ij}]. \tag{1.7}$$

(Abazajian et al., 2015) In this equation, ζ describes scalar perturbations and γ describes tensor perturbations. The scalar perturbations source the density perturbations of the early universe that evolve and collapse into the stars and galaxies that now permeate the universe. The tensor perturbations, which are expected to be smaller than the scalar perturbations, create primordial gravitational waves. The ratio of tensor to scalar perturbations is parameterized by r, (Abazajian et al., 2015)

$$r = \frac{\langle \gamma\gamma \rangle}{\langle \zeta\zeta \rangle} = \frac{A_t}{A_s}. \tag{1.8}$$

The amplitude of the tensor-to-scalar ratio encodes the energy scale at which inflation occurs and is related to the type of scalar field that could cause the exponential expansion. The detection of primordial gravitational waves ($r > 0$) is considered the "smoking gun" for determining if an inflationary phase of expansion occurred in the early universe (Committee for a Decadal Survey of Astronomy and Astrophysics, National Research Council, 2010). A non-zero value of r would be the first detection of quantum mechanical fluctuations of the spacetime metric and would indicate the presence of super-horizon gravitational waves at the beginning of ΛCDM evolution, one of the predictions of inflation not present in other theories describing the initial conditions of the universe. The amplitude of these gravitational waves is predicted to be small enough that they will not be directly detectable with gravitational wave detection instruments, however, it is still possible we can detect them via their influence on the polarization of the cosmic microwave background.

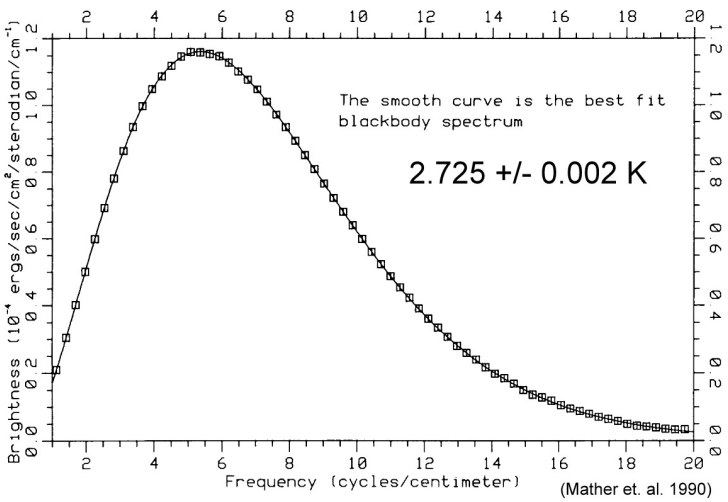

Figure 1.2: The spectrum of the CMB observed by the COBE satellite mission (Mather et al., 1990). The CMB spectrum is the best naturally occurring blackbody ever observed. The uniformity and isotropy of the temperature across the sky is proof of the homogeneity and isotropy of the universe.

1.3 The Cosmic Microwave Background

The cosmic microwave background (CMB) is blackbody radiation that was created during the early universe when the universe was filled with a hot and dense plasma. The radiation was in thermal equilibrium with the protons and electrons until radiation decoupled from the baryonic matter as the universe expanded and cooled. Today the CMB is at 2.725 Kelvin and its uniformity across the sky is evidence of the homogeneity and isotropy of the universe. Figure 1.2 shows the CMB spectrum measured by the COBE satellite mission (Mather et al., 1990), the spectrum of the CMB is the best naturally occurring blackbody ever observed. There are small (part in 10^{-5}) fluctuations in the temperature of the CMB, shon, in figure 1.3, that are primarily caused by the density perturbations that existed in the universe when radiation and matter decoupled.

The scale-invariant scalar (density) perturbations that exist at the end of inflation

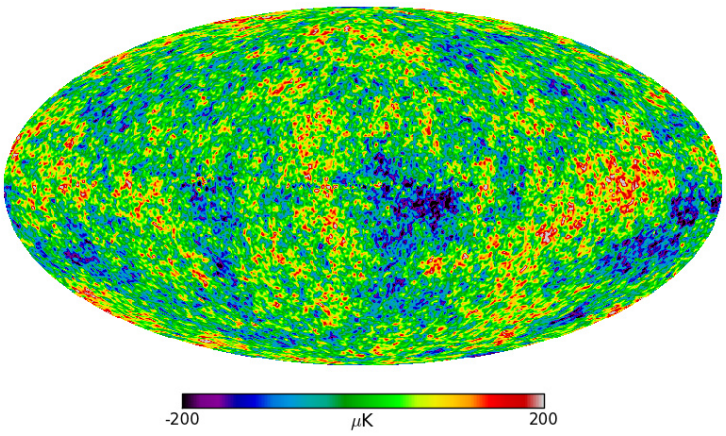

Figure 1.3: The temperature fluctuations of the cosmic microwave background across the sky. The emission from the galaxy has been removed to illustrate the range of just the CMB fluctuations. The temperature fluctuations are primarily caused by density perturbations in the early universe. The data from this map was taken from Bennett et al. (2013).

evolve, and features are created in the power spectrum of the CMB anisotropies based on the content of the universe. For example, the primordial plasma acts as a fluid, and the initial density perturbations create pressure waves that grow and decay at the speed of sound for the fluid. When the baryons and photons decouple, the modes which are at their peak amplitude cause peaks in the CMB power spectrum, with an amplitude proportional the the amount of matter in the universe.

The power spectrum of the temperature anisotropies of the CMB is calculated from an expansion of the temperature anisotropies into spherical harmonics,

$$a_{T,\ell m} = \int d\hat{n}\, \Delta T(\hat{n}) Y^*_{\ell m}(\hat{n}), \tag{1.9}$$

where $\Delta T(\hat{n})$ is the map of the temperature fluctuations across the sky and $Y_{\ell m}$ are the spherical harmonics (Weinberg, 2008). Since the density perturbations seeding the temperature fluctuations of the CMB are sourced by a Gaussian random field, it is expected that the $a_{\ell m}$'s will be a Gaussian random variable. Different angular

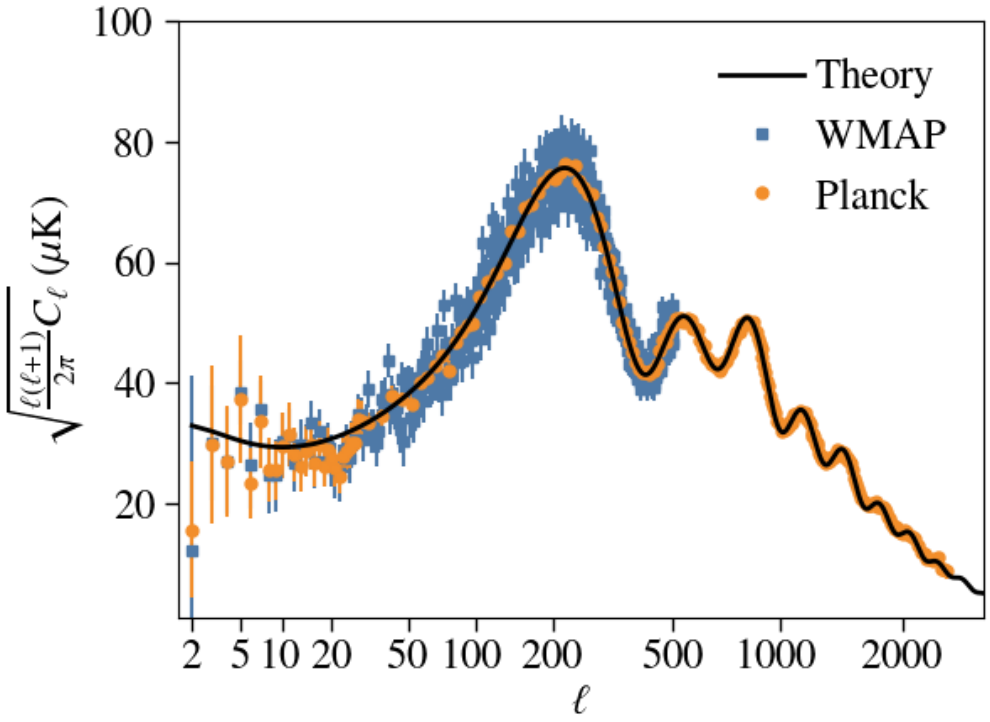

Figure 1.4: The power spectrum of the temperature fluctuations of the CMB. The data from WMAP and Planck (Hinshaw et al., 2013; Planck Collaboration et al., 2016a) all show good agreement with the ΛCDM theory curve (using Planck 2015 parameters). The angular position of the peaks gives a measure of the angular diameter of the sound horizon at recombination, this can be combined with other measurements to constrain the curvature of the universe. The amplitude of the peaks constrain the amplitude of the primordial scalar power spectrum A_s and the ratio of the peak amplitudes are an indication of the fraction of the non-relativistic matter that is composed of baryons. The fall off at higher ℓ is due to damping from radiation diffusion and, since the photon density is well constrained though measurements of the temperature of the CMB, creates a constraint on the energy density of relativistic neutrinos in the early universe.

ℓ modes evolve separately in the early universe, so the $a_{\ell m}$'s for each ℓ will have a different mean value equal to

$$C_\ell^{TT} = \frac{1}{2\ell+1} \sum_m a_{T,\ell m}^* a_{T,\ell m}. \tag{1.10}$$

Figure 1.4 shows the power spectrum of the CMB anisotropies as measured by WMAP and Planck (Hinshaw et al., 2013; Planck Collaboration et al., 2016a). The measurements show extraordinary agreement between the different experiments and the black theory curve (drawn with Planck 2015 parameters). The angular position of the peaks gives a measure of the angular diameter of the sound horizon at recombination, this can be combined with other measurements to constrain the curvature of the universe. The amplitude of the peaks constrain the amplitude of the primordial scalar power spectrum A_s[2] and the ratio of the peak amplitudes are an indication of the fraction of the non-relativistic matter that is composed of baryons. The fall off at higher ℓ is due to damping from radiation pressure and, since the photon density is well constrained though measurements of the temperature of the CMB, creates a constraint on the energy density of relativistic neutrinos in the early universe.

In addition to the CMB temperature anisotropy, there is also a CMB polarization anisotropy. The polarization anisotropy is caused by local quadrupole moments at the surface of last scattering. These quadrupoles can be created by either gradients in the density field (scalar perturbations) or gravitational waves (tensor perturbations)[3]. Polarization is created through the CMB photos scattering off electrons through

[2]There is actually a degeneracy between the amplitude of the scalar fluctuations and the optical depth to reionization, so the heights of the peaks are really a function of $A_s e^{-2\tau}$. This degeneracy is broken on larger angular scales where τ has less affect on the temperature fluctuations.

[3]Quadrupole moments could be created by vector perturbations in addition to scalar and tensor perturbations, however, vector perturbations are quickly damped out in the early universe.

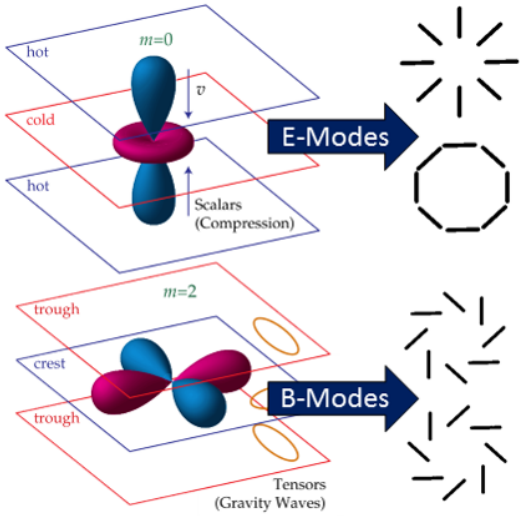

Figure 1.5: Sketches of scalar (top) and tensor (bottom) quadrupole moments. Scalar quadrupoles in the metric of spacetime are produced by density fluctuations while tensor quadrupoles come from gravitational waves. Photons scattering off electrons in local scalar quadrupole moments result in E-mode polarization patterns in the CMB. Scatting of photons and electrons in local tensor quadrupole moments create E- and B-modes and are the only source of primordial B-mode polarization. Quadrupole sketches from Hu et al. (1997)

Compton scattering. Compton scattering is inherently a polarized process, however, in a completely isotropic photon distribution the net polarization is zero; local quadrupole moments are required to produce net linear polarization along some direction. Subsequent scattering events will erase the polarization from previous interactions, so any polarization observed in the CMB is from the last interaction the photons had with electrons.

As with the temperature anisotropy, the polarization anisotropy can be expanded into spherical harmonic space, however, since polarization is a spin-2 field, spin-2 spherical harmonics are required to complete this expansion. If $Q(\hat{n})$ and $U(\hat{n})$ are

maps of the linear Stokes parameters[4] across the sky, this expansion is

$$Q(\hat{n}) - iU(\hat{n}) = \sum_{\ell=2}^{\infty} \sum_{m=-\ell}^{\ell} a^*_{P,\ell m} \mathcal{Y}^m_\ell(\hat{n})^*, \tag{1.11}$$

where $\mathcal{Y}^m_\ell(\hat{n})^*$ describes the set of spin-2 spherical harmonics (Weinberg, 2008). Due to the spin-2 nature of the polarization field and the definitions of Stokes parameters on a sphere, Q, U, and thus $a_{P,\ell m}$ are not rotationally invariant on a sphere, meaning rotations mix Q and U. However, it is possible to split $a_{P,\ell m}$ into two modes which are both rotationally invariant, called E- and B-modes,

$$a_{E,\ell m} \equiv \frac{-\left(a_{P,\ell m} + a^*_{P,\ell -m}\right)}{2} \quad \text{and} \quad a_{B,\ell m} \equiv \frac{i\left(a_{P,\ell m} - a^*_{P,\ell -m}\right)}{2}. \tag{1.12}$$

Shown in figure 1.5, E-modes are a curl-free polarization pattern have reflection symmetry and B-modes are a divergence free pattern which is anti-symmetric with reflection. It is now possible to define power spectra C^{EE}_ℓ and C^{BB}_ℓ analogous to the temperature anisotropies in equation 1.10. Cross spectra, such as C^{TE} are possible as well.

When the polarization patterns imprinted on the CMB from local quadrupole moments are traced through to their affect on C^{EE}_ℓ and C^{BB}_ℓ, it can be found that E-modes are produced by both scalar and tensor quadrupole moments while B-modes are solely produced by quadrupole moments (Hu et al., 2002). This means that observation of B-modes produced by tensor quadrupole moments (gravitational waves) in the early universe is a mechanism for detecting primordial gravitational waves created during an epoch of inflationary expansion during the early universe.

Figure 1.6 shows a compilation of the theoretical power spectra describing the temperature and polarization anisotropy present in the CMB as well as the published

[4] see Appendix A for details on Stokes Parameters

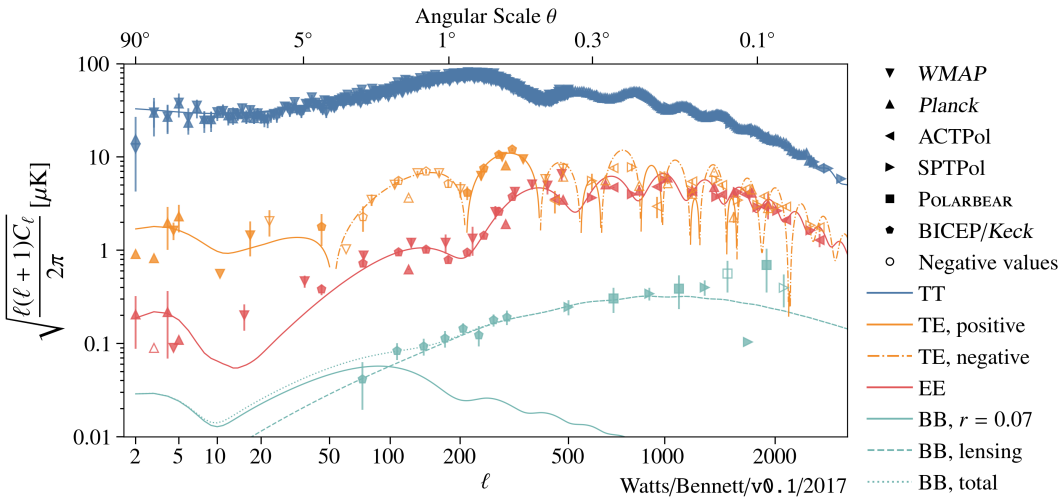

Figure 1.6: The current status of CMB angular power spectrum measurements. The temperature anisotropies (TT) are constrained to the cosmic variance limit down to very low ℓ by the WMAP and Planck satellites and are constrained at the high end by the larger telescopes of ACTPol and SPTpol. The E-mode anisotropies (EE) are well understood at small angular scales but the error bars are much larger at large angular scales. B-mode polarization (BB) has been detected at smaller angular scales in a region where the gravitational lensing of E-modes is the dominate source but the inflationary B-modes at larger angular scales are still undetected.(Figure from Duncan Watts, data from Bennett et al. (2013), Planck Collaboration et al. (2016a), Naess et al. (2014), Keisler et al. (2015), Crites et al. (2015), Polarbear Collaboration et al. (2014), and BICEP2/Keck Array Collaborations et al. (2016))

measurements to date. The blue curve, denoting the temperature anisotropy, is the same curve as that shown in figure 1.4. At degree angular scales and smaller, the EE power spectra shows the effect of density gradients at the surface of last scattering during recombination. These acoustic peaks allow another measurement of the various cosmological parameters available in the TT power spectra. The E-mode polarization at these angular scales was first observed by DASI (Kovac et al., 2002) and have since been measured by many other experiments.

E-mode polarization at angular scales much larger than a degree on the sky ($\ell \lesssim 20$) is mostly produced through the re-scattering of CMB photons after the universe re-ionized. The amplitude and angular location of this effect provides a direct measurement of the optical depth to reionization that is defined as

$$\tau = \int_{t_{\rm lss}}^{t_0} n_{\rm e}(t)\sigma_T c\, dt, \tag{1.13}$$

where $n_e(t)$ is the number density of free electrons, σ_T is the electron-photon cross section, and $t_{\rm lss}$ is the last scattering surface. A high sensitivity measurement of τ constrains the redshift of reionization and thus the star formation history of the universe. The top row in figure 1.7 shows the effect of varying τ, while keeping the well constrained value of $A_s e^{-2\tau}$ constant, on the power spectra of the CMB. Due to the difficulty of achieving high sensitivity polarization measurements across large fractions of sky, the E-modes on the largest angular scales are still in need of an improved measurement.

The lowest lines on figure 1.6 show the B-mode power spectrum in the CMB, which is several orders of magnitude lower in temperature than the temperature anisotropies. At angular scales smaller than about a degree on the sky, the BB spectra

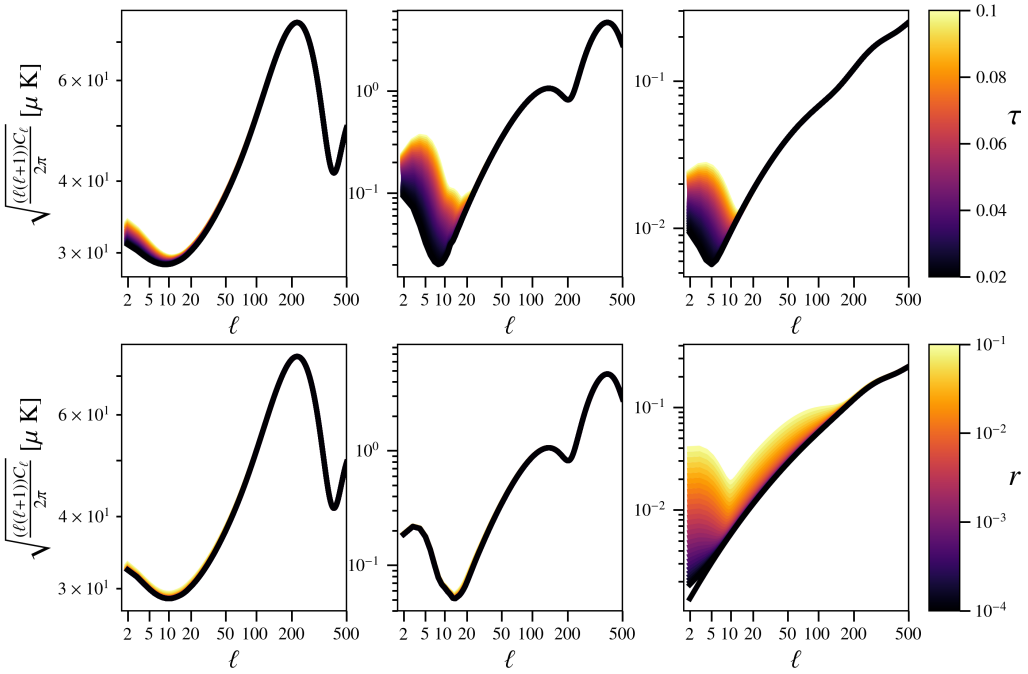

Figure 1.7: Top row: The effect of changing the value of the optical depth to reionization, τ, while holding $A_s e^{-2\tau}$ constant on the TT (left) EE (center) and BB (right) power spectra of the CMB. A higher optical depth the reionization leads to more power on the largest scales of the E- and B-modes of the CMB. With the exception of τ, power spectra in the top row of plots assumes Planck 2015 parameters and $r = 0.02$. Bottom row: The effect of changing the value of the tensor-to-scalar ratio, r, on the TT (left) EE (center) and BB (right) power spectra of the CMB. The amplitude of the BB power spectra decreases with decreasing r, but is bounded by the gravitational lensing of E-modes into B-modes at higher angular scales.

is due to the gravitational lensing of E-modes into B-modes by large scale structure. These gravitationally lensed B-modes were first detected via cross correlation by the South Pole Telescope (Hanson et al., 2013) and directly by the POLARBEAR Collaboration at higher ℓ (Polarbear Collaboration et al., 2014) and the BICEP/Keck collaboration at lower ℓ (BICEP2/Keck Array Collaborations et al., 2016)

The B-modes sourced by inflationary gravitational waves are highest at the largest angular scales ($\ell \lesssim 150$) and the amplitude of this signal depends on the tensor-to-scalar ratio, r. The two peaks in this signal are due to the changing ionization state of the universe at reionization ($\ell \sim 10$) and recombination ($\ell \sim 100$). The two time periods are the two eras in the universe when there are free electrons for the CMB photons to scatter off *and* the photons are not likely to re-scatter. The bottom row of figure 1.7 shows how the CMB power spectra changes for various values of r, the amplitude scales with r but is bounded from below by the gravitational lensing of E-modes into B-modes.

The measurement of B-mode polarization by the BICEP/Keck team provides the best polarization-only constraint on the tensor-to-scalar ratio of $r < 0.09$ which decreases to $r < 0.07$ when other observations are added (BICEP2/Keck Array Collaborations et al., 2016). These B-mode measurements have only been on angular scales of about a degree and smaller, the largest angular scale B-modes remain undetected. The most compelling models of inflation predict $r \sim 0.01 \rightarrow 0.001$ (Abazajian et al., 2015) and differentiating between r on that level would significantly impact our understanding of physics at the highest energies.

1.4 Thesis Overview

The rest of this thesis will cover the work I have done with the Cosmology Large Angular Scale Surveyor (CLASS), a telescope array aiming to map the largest angular scales of the CMB polarization. Chapter 2 provides a detailed overview of the CLASS scientific goals and instrument design. Significant portions of this chapter are taken from Harrington et al. (2016) but they have been updated to include advances in the work over the last two years. Chapter 3 covers various projects I completed for the cryogenic plastic optics for the Q-band and W-band CLASS telescopes. Chapters 4, 5, and 6 are all on my main PhD work, the variable-delay polarization modulators for the CLASS telescopes. Chapter 4 is taken nearly verbatium from Harrington et al. (2018) and covers the design requirements, the mechanical and control system designs and implementation, and the performance of the first two CLASS VPMs. Chapter 5 is a detailed look at the electromagnetic modeling of the VPMs, encompassing modulation functions for ideal and realistic VPMs in the CLASS telescopes and a mechanism for calculating the emission from a VPM. Chapter 6 describes work I have completed on data structures for the CLASS telescope, characterization of the detectors enabled by the VPM, and the demodulation of the VPM data to increase the long-time-scale stability of data from the CLASS telescopes.

Chapter 2

Cosmology Large Angular Scale Surveyor

This chapter is an expanded version of the CLASS overview paper Harrington et al. (2016).

The Cosmology Large Angular Scale Surveyor (CLASS) is a four telescope array uniquely suited to mapping the largest angular scales of the polarization of the CMB from the ground. By specifically targeting $\ell \lesssim 150$, CLASS will make a cosmic variance limited measurement of the optical depth to reionization through the large angular scale E-modes and measure or set limits on the amplitude of primordial gravitational waves to a level of $r \lesssim 0.01$(95% C.L.) through the large angular scale B-modes.

Observing the CMB polarization at the largest angular scales requires a high sensitivity measurement of the polarization at multiple frequencies and across large fractions of sky. This necessitates instrument stability and systematic rejection at unprecedented levels. CLASS, sited in the Chilean Atacama Desert, is currently the only telescope designed to recover the largest angular scales of the CMB polarization from the ground (Essinger-Hileman et al., 2014; Harrington et al., 2016). The CLASS telescopes cover four frequency bands, one telescope at 40 GHz (Q-band), two at

90 GHz (W-band), and one high frequency dichroic at 150/220 GHz. These frequency bands span the galactic foreground minimum and enable foreground cleaning at the level necessary to extract cosmological parameters from the CLASS maps(Watts et al., 2015; Watts et al., 2018). Each CLASS telescope has a $\sim 20^{\circ}$ field of view and executes constant elevation scans with daily boresight rotations to map $\sim 70\%$ of the sky every day. Daily maps and boresight rotations provide a large variety of null tests and systematics checks which are used to track instrument stability and verify the content of the final maps.

2.1 Science Objectives

2.1.1 Inflation

As discussed in chapter 1, one of the current goals in the field of cosmology is to observe evidence of super-horizon primordial gravitational waves (PGW) seeded by the inflationary expansion of the early universe. The only known method of detecting these PGWs is through their imprint on the large angular scale B-modes in the CMB polarization. Shown in figure 2.1, the amplitude of the PGW signal depends on the tensor-to-scalar ratio r, however, with the current constraints on r, gravitational lensing of E-modes into B-modes surpasses the amplitude of the PWGs, at angular scales of $\ell \gtrsim 100$.

Figure 2.1 also shows progress to date for the field of B-mode measurements and forecasts for the CLASS B-mode measurement. The left plot shows that SPT, Polarbear, and BICEP2/*Keck* have detected B-mode polarization due to gravitational lensing of E-mode polarization (Keisler et al., 2015; Polarbear Collaboration et al., 2014; BICEP2/Keck Array Collaborations et al., 2016). The BICEP2/*Keck* polarization

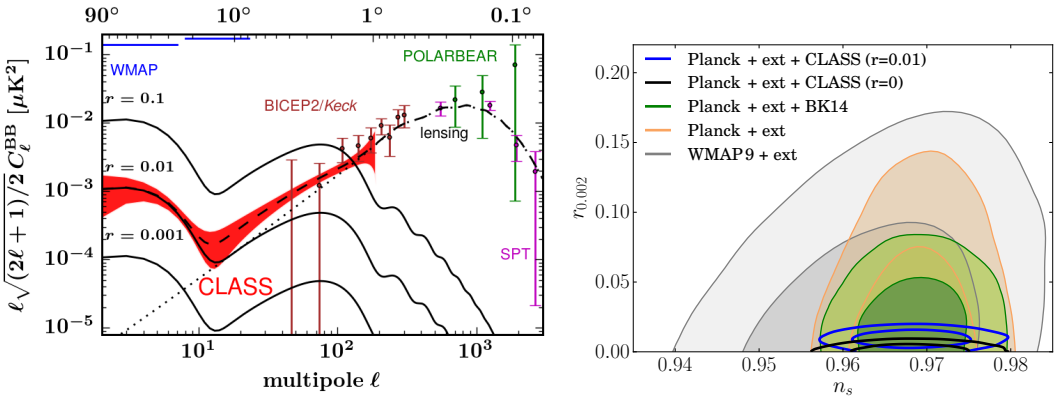

Figure 2.1: The CLASS B-mode Measurement. The **left figure** shows power spectra for B-mode amplitudes of $r = 0.1$, 0.01, and 0.001 with peaks at multipole moments $\ell < 10$ (the "reionization peak") and $\ell \approx 100$ (the "recombination peak"). The dashed curve shows the lensing of E-modes dominates the B-modes at small angular scales. The level was confirmed by SPT, POLARBEAR, and BICEP2/*Keck* (Keisler et al., 2015; Polarbear Collaboration et al., 2014; BICEP2/Keck Array Collaborations et al., 2016). The lensing B-modes have higher amplitude than the primordial signal for $r = 0.01$ except at $\ell < 20$, where the lensing foreground is negligible. With the exception of CLASS, all on-going measurements are designed to focus on the recombination peak and thus do not reach the largest scales (Figure 2.4). Due to its unique design CLASS probes all angular scales where the B-modes are strongest with sensitivity per $\log(\ell)$ shown in red. Multi-frequency measurements will be used to clean the Galactic foregrounds. *WMAP* measurements limit the B-mode amplitude at low-ℓ (Bennett et al., 2013). The **right figure** shows upper limits on r and measurements of n_s as deduced from datasets primarily based on *WMAP* (Hinshaw et al., 2013), *Planck* (Planck Collaboration et al., 2016c), and BICEP2/*Keck* (BK14) with *Planck* (BICEP2/Keck Array Collaborations et al., 2016). Forecasted CLASS constraints from simulations that include pessimistic effects of Galactic foregrounds are shown for two different simulated B-mode levels (Watts et al., 2015). CLASS will substantially reduce the upper limits on r or determine r in a reliable and robust manner.

measurements at $\ell \sim 100$ offer the most stringent polarization-only constraint on r to date with $r < 0.09$ (95% C.L.) (BICEP2/Keck Array Collaborations et al., 2016). Constraints improve to $r < 0.07$ (95% C.L.) if *Planck* temperature data are included (BICEP2/Keck Array Collaborations et al., 2016). The CLASS sensitivity per $\log(\ell)$ for $r = 0.01$ is shown in the left plot of figure 2.1 by the red envelope, indicating sensitivity to both the recombination and reionization peaks. Measuring both peaks in the B-mode spectrum is an important confirmation that a systematic error is not masquerading as the faint primordial B-mode signal, especially if the recombination

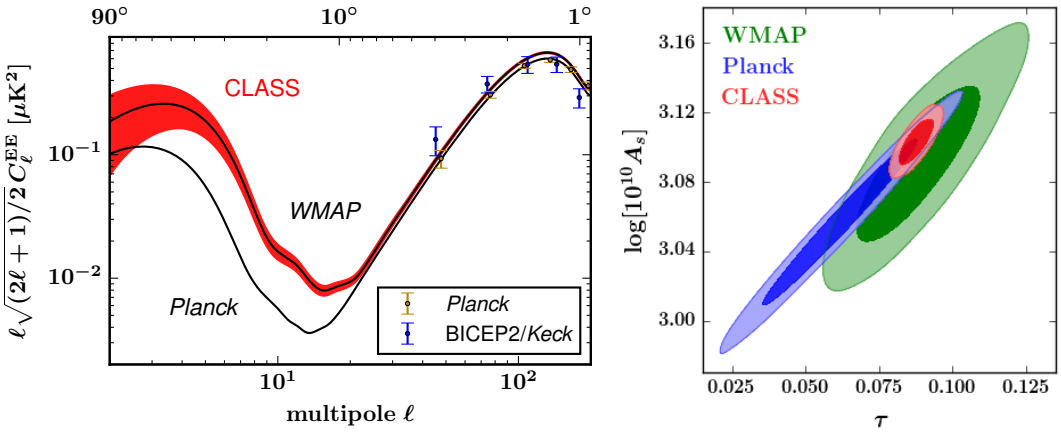

Figure 2.2: Large-scale E-mode Science. The **left figure** shows measurements and best-fit models for the low-ℓ E-mode polarization spectrum. The model for the upper black curve derives from WMAP 9-year (+SPT+ACT+SNLS3+BAO+H0) data, corresponding to $\tau = 0.083$, whereas the model for the lower black curve shows the *Planck* "pre-2016 lowE" result, corresponding to $\tau = 0.055$ (Planck Collaboration et al., 2016e). The red envelope, which represents the CLASS survey noise per $\log(\ell)$, shows that CLASS will discriminate between the *WMAP* and *Planck* best fit models, a result with implications for high-z galaxy formation. The data at $\ell \geq 50$ are the latest from the *Planck* HFI and BICEP2/*Keck*. CLASS is stable enough to reach lower ℓ and complete the E-mode measurement. The **right figure** shows constraints on τ and $\log(10^{10}A_s)$ from *WMAP* (green) and *Planck* (blue) temperature and polarization (Hinshaw et al., 2013; Planck Collaboration et al., 2016c). The *Planck* contours are based on the 2015 release instead of the more recent "pre-2016" results(Planck Collaboration et al., 2016e) because likelihoods were not released for the latter. The uncertainty is dominated by degeneracy between the two parameters. The CLASS τ measurement breaks this degeneracy. (The WMAP9 value for τ has been assumed in the CLASS constraint.)

peak is significantly below the level of lensing B-modes. The right plot of figure 2.1 shows that CLASS will provide roughly an order-of-magnitude improvement in raw sensitivity to r (Watts et al., 2015; Miller et al., 2016).

2.1.2 Reionization

Observing the E-mode polarization at the largest angular scales will allow CLASS to further constrain the epoch of reionization. The CLASS survey will make a nearly cosmic variance limited measurement of the E-mode spectrum below $\ell \approx 100$ (Figure 2.2, left panel), with a corresponding error on the optical depth to reionization of

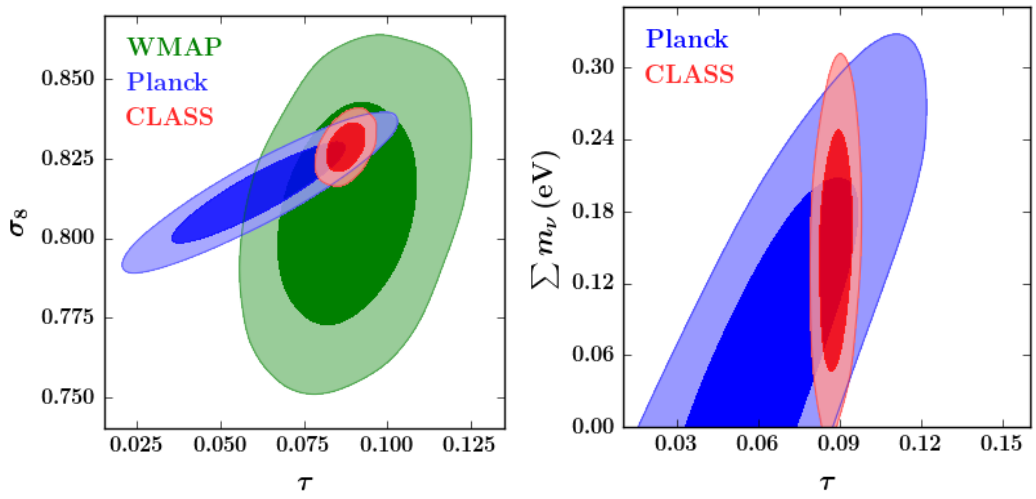

Figure 2.3: Improving CMB-based ΛCDM Predictions for LSS. The ΛCDM model fit to the primary CMB provides predictions for LSS that can be compared to direct probes, such as galaxy weak lensing, galaxy cluster counts, and CMB lensing. However the CMB-based LSS predictions are now strongly limited by degeneracies, especially between A_s and τ (Figure 2.2). The **left figure** shows how the CLASS E-mode measurement will improve predictions for σ_8. Reconciling the CMB LSS predictions with those from direct LSS probes will provide tight constraints on the sum of neutrino masses $\sum m_\nu$. The **right figure** shows improvement to the *Planck* 2015 and BAO (Planck Collaboration et al., 2016c) constraints on $\sum m_\nu$. (The *Planck* contours are based on the 2015 data (Planck Collaboration et al., 2016c))

$\sigma_\tau \sim 0.002$ (Watts et al., 2018). This is a factor of five bettter than the current precision from Planck (Planck Collaboration et al., 2016f). Furthermore, because the CLASS measurement will be nearly cosmic variance limited, the next generation polarization experiments, including future possible space missions, will not significantly improve the CLASS E-mode measurement(Watts et al., 2018). This measurement will be an important complement and crosscheck to the current and next generation of 21-cm measurements of the epoch of reionization (Clesse et al., 2012; Liu et al., 2016).

2.1.3 Neutrino Physics

A cosmic variance limited measurement of the optical depth to reionization will have "down-stream" effects on constrains of other cosmological parameters due to

degeneracies between τ and these parameters. For example, the CMB constraints on large scale structure (LSS) are based on A_s and are therefore limited by a degeneracy between the A_s and τ that is present in the TT CMB power spectrum. CMB temperature fluctuations, which increase with A_s, are suppressed by reionization such that the amplitude of the temperature spectrum constrains the parameter combination $A_s e^{-2\tau}$. This A_s vs τ degeneracy is apparent in the right panel of Figure 2.2. The uncertainty on A_s is dominated by this degeneracy, so the CLASS τ constraint reduces the *Planck* 2015 or *WMAP*-based uncertainty on $\log(10^{10} A_s)$ by a factor of three. Figure 2.3 shows the corresponding 2.5 times improvement in precision over the *Planck* 2015 estimate of σ_8 (two-fold improvement relative to *Planck* "pre-2016", (Planck Collaboration et al., 2016f)).

Such an improvement will sharpen or resolve discrepancies arising between the predictions of the CMB-based ΛCDM models and direct probes of LSS, such as galaxy cluster measurements (Planck Collaboration et al., 2016d). These discrepancies could be due to systematic errors in measurements; however, there *are* physical effects, such as the finite neutrino mass, that should produce discrepancies detectable with the sensitivity of the next generation of CMB lensing (e.g., by Advanced ACTPol, Simons Array, and SPT3G or Simons Observatory surveys) and Baryon Acoustic Oscillation (BAO) measurements (e.g., DESI).[1] Future LSS measurements will be limited by our uncertainty on A_s without an improved τ measurement.

Neutrino oscillation measurements, which are sensitive to the difference of the neutrino masses, put a lower bound of $\sum m_\nu \geq 60$ meV on the sum of the neutrino masses (100 meV for an inverted mass hierarchy with two heavy neutrinos) (Feldman

[1] Other probes of LSS associated with galaxy and galaxy cluster surveys, such as cluster counts and the matter power spectrum, will also constrain $\sum m_\nu$. CMB lensing with BAO has the advantage of being relatively immune to systematics associated with baryonic processes.

et al., 2013). The authors of Allison et al. (2015) investigate the power of the primary CMB in combination with the next generation of CMB lensing and BAO measurements to constrain $\sum m_\nu$. They show that without an improvement in the current low-ℓ E-mode measurement, the future experiments will be limited to $\sigma(\sum m_\nu) \approx 27$ meV (22 meV if *Planck* reaches it's ultimate low-ℓ sensitivity), which would provide only 2σ evidence if $\sum m_\nu = 60$ meV. With a cosmic variance limited E-mode measurement, the parameter-covariance-dominated error reduces to $\sigma(\sum m_\nu) \approx 15$ meV, giving a 4σ detection of the minimum-allowed $\sigma(\sum m_\nu)$. Thus the CLASS E-mode measurement is a key ingredient in pursuit of a cosmological measurement of the sum of neutrino masses.

2.2 Survey Strategy

Observing the polarization of the CMB on the largest angular scales requires mapping large fractions of the sky while maintaining the stability and control over systematics necessary to reconstruct the largest angular scales. Figure 2.4 shows the ℓ range accessible to the CLASS survey, limited by beam width at the high end and sky fraction on the low end, as well as the ℓ range targeted by contemporary experiments. CLASS is sited in the Chilean Atacama desert where it can make daily maps over 70% of the sky (-78° $< \delta <$ +32°)[2] by scanning in great circles at a constant 45° elevation. This scan pattern cross-links the maps, meaning each point in the sky is observed with the telescope at many different orientation angles. In addition, daily 15° boresight rotations[3] provide further polarization angle rotations. The combination of daily full sky coverage, scan crosslinking, and boresight rotations enable a large suite of

[2]This fraction takes into account CLASS's large 200 deg^2 field of view.

[3]Boresight rotations are rotations around the optical axis of the telescope, effectively rotating the polarization angles of the detectors on the sky.

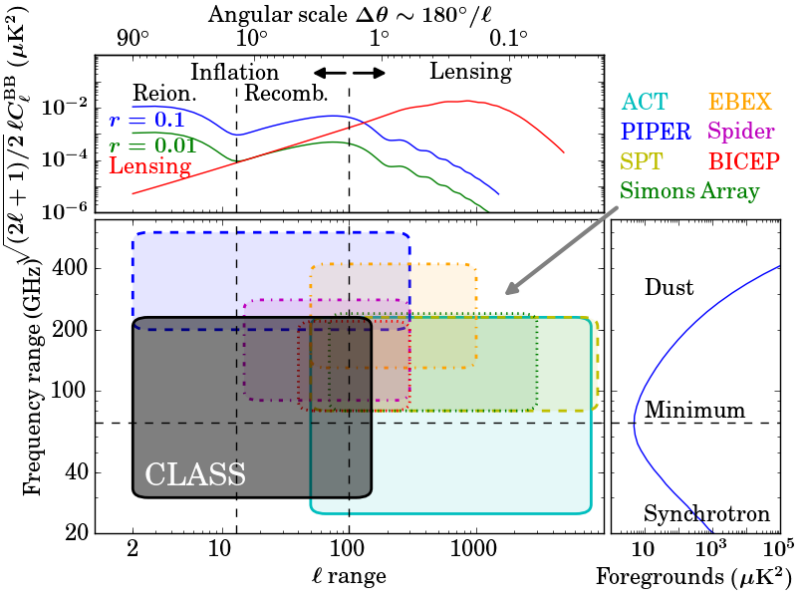

Figure 2.4: We display schematically the regions of purview corresponding to balloon-borne and ground-based CMB polarization experiments. CLASS is unique in measuring both the reionization and recombination peaks while straddling the foreground minimum. As upper limits on r decrease, inflationary B-modes will dominate over lensing at increasing larger scales. The foreground model shown comes from (Planck Collaboration et al., 2016b) using measurements of 73% of the sky. We plot the frequency dependence of foregrounds in thermodynamic temperature units. Figure and caption from (Watts et al., 2015).

systematics checks and degeneracy breaking while solving for the polarization map from the raw bolometer timestreams.

One of the main challenges with recovering the largest angular scales in the CMB polarization is the presence of polarized Galactic foregrounds from synchrotron emission at lower frequencies and thermal dust emission at higher frequencies. Figure 2.4 shows the amplitude of the combined polarized Galactic foreground signal using models from Planck Collaboration et al. (2016b) assuming 73% of the sky. CLASS has four frequency bands at 40 GHz, 90 GHz, 150 GHz, and 220 GHz, which surround the foreground minimum and enable the removal of foregrounds from the sky maps. Figure 2.5 shows simulated maps of Stokes Q of the CMB compared to foreground

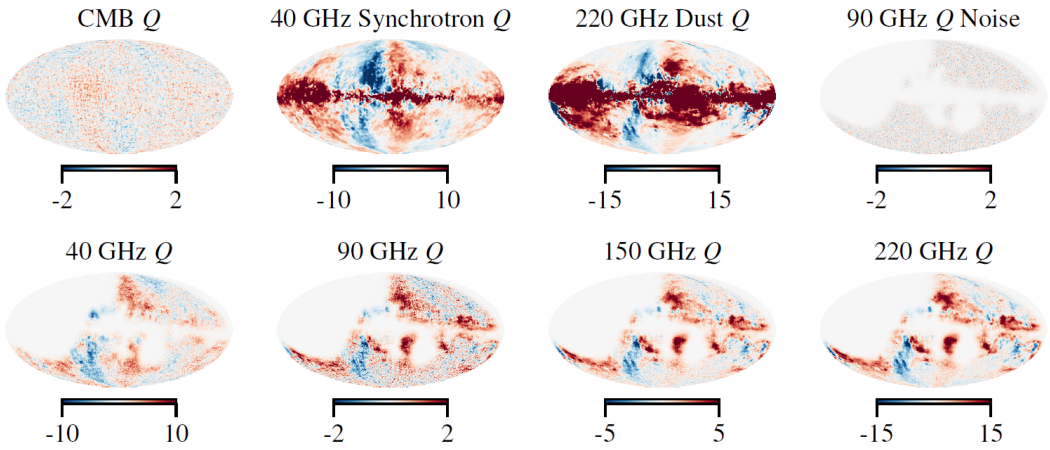

Figure 2.5: The simulated CLASS maps include a realization of the CMB, polarized synchrotron and thermal dust emission, and Gaussian white noise. The top panels show the individual Stokes Q components of the simulation, while the bottom show the simulated multifrequency Stokes Q CLASS maps, with the Galactic plane masked and parts of the celestial Northern Hemisphere and celestial Southern Hemisphere excluded by the survey boundary. All maps are displayed in Galactic coordinates with units of μK. Figure and caption from (Watts et al., 2018).

signals from synchrotron and thermal dust emission as well as simulated maps for all the CLASS frequency bands. Watts et al. (2015) and Watts et al. (2018) demonstrated that these frequency bands at the predicted final CLASS sensitives are sufficient to recover the large angle scale E-modes and B-modes at the level required to make a nearly cosmic variance limited measurement of τ and measure or set limits on inflationary PGWs down to $r < 0.01$ (95% C.L.).

Table 2.1 lists the parameters for each of the four CLASS telescopes. To achieve the combined sensitivity requirements and foreground coverage, CLASS has one telescope at 40 GHz (Q-Band), two telescopes at 90 GHz (W-band), and one dichroic high frequency (HF) array at 150/220 GHz. Each 90 GHz telescope will be co-mounted with one of the foreground focused telescopes to achieve two completely independent 90 GHz maps for significant systematics checks at the galactic foreground minimum.

Telescope	Frequency Range (GHz)	Beamwidth (arcmin)	N_{det}	Array NEP (aW$\sqrt{s}$)
Q	33-43	90	72	16[a]
W1	77-108	40	518	2.1[b]
W2	77-108	40	518	
HF	127-163	24	$\sim$ 510	
	200-234	18	$\sim$ 510	

Table 2.1: Summary of parameters of the four CLASS telescopes.

[a] Appel et al., 2014.
[b] Dahal et al., 2018.

The total survey time is five years (2016–2021) with a staged deployment of the CLASS telescopes over the first two years. The 40 GHz telescope and the first 90 GHz telescope are now in the field and will be followed by the second 90 GHz telescopes and finally the 150/220 GHz telescope.

2.3 Experiment Design

2.3.1 Site and Operations

CLASS measures the CMB polarization from 5200 m in the Atacama Desert of northern Chile. The site, shown in Figure 2.6, provides access to 70% of the sky and allows observation through low atmospheric water vapor and oxygen column densities. This results in reduced atmospheric brightness in the CLASS frequency bands(Essinger-Hileman et al., 2014). The left plot in figure 2.7 shows the atmospheric brightness temperature as a function of frequency for various levels of precipitable water vapor (PWV) in the atmosphere. The atmosphere is one of the main sources of loading and therefore detector noise. Reducing this loading by observing from the highest and driest site possible significantly increases the sensitivity of the telescopes. The right

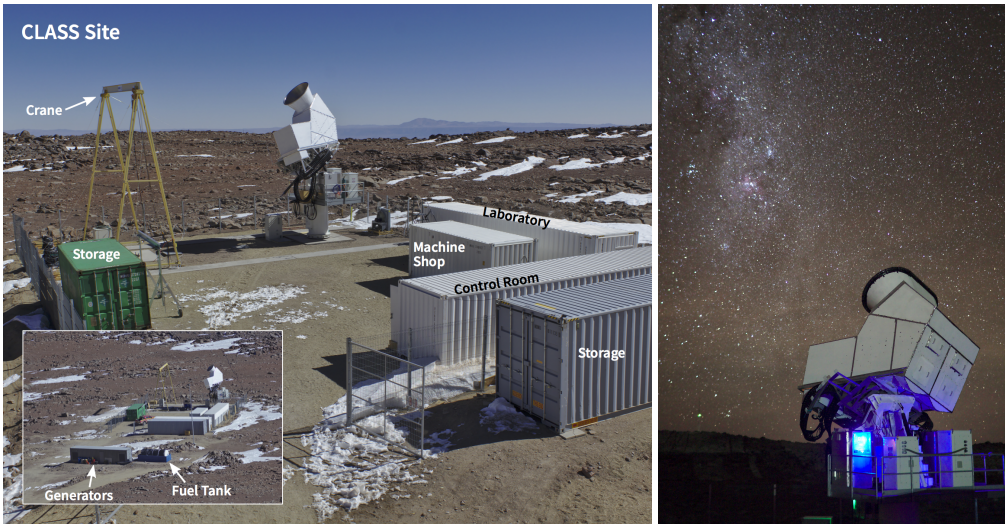

Figure 2.6: Left Figure: The CLASS site as it was in October 2016. The Q-band telescope is installed on the first CLASS mount and the control, laboratory, and machine shop containers are inside the fenced area. **Right Figure:** June 2018. The co-pointed 40 and 90 GHz telescopes installed at the CLASS site. Visible in the photograph are the co-moving ground screen, forebaffle, and platform containing the gas handling system for the receiver and the mount drive system.

plot in figure 2.7 shows the PWV at the CLASS site, as measured by the nearby APEX experiment, during our first observing era. The median PWV during this era was 1.015 mm, verifying the CLASS is observing from one of the driest high altitude sites in the world.

Construction on the site began in early 2015. The flattened, fenced site contains two concrete pedestals for the two CLASS mounts. Power is provided by two redundant, 100 kW (derated), diesel powered generators, and a 400 Mb/s radio link to the base of operations in San Pedro de Atacama allows communication with the site. A custom data packaging system transmits the telescope data via the radio link to San Pedro, where it is stored. Currently, the telescope data is transferred via the Internet to North America.

The control room, laboratory, and machine shop containers, shipped with the

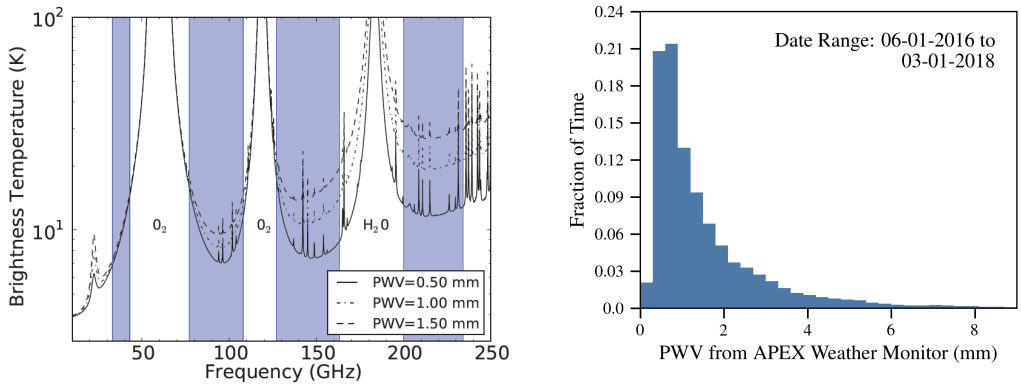

Figure 2.7: (Left) Estimated mean atmospheric brightness temperature (Rayleigh-Jeans) versus frequency for precipitable water vapor (PWV) levels of 0.5, 1.0, and 1.5 mm along with the CLASS bandpasses in blue, for an atmosphere at physical temperature of 250 K. The CLASS bands were chosen to avoid the prominent oxygen and water emission lines. As PWV increases, the broad water line at 183 GHz contaminates the 93, 148, and 217 GHz bands in particular. Figure and caption from Essinger-Hileman et al. (2014). (Right) The PWV at the CLASS Site, as measured but the neighboring APEX experiment, during our first observation era. The median PWV during this time was 1.015 mm.

first CLASS mount and 40 GHz receiver packed inside, arrived at the CLASS site in December 2015. The telescope mount was installed in January 2016 and the 40 GHz receiver was installed in the spring of 2016, where it achieved first light on May 8th 2016.

The Q-band CLASS telescope was on sky between June 2016 and March 2018, when it was taken down, refurbished and re-installed with the first W-band telescope installed beside it on the same mount. This time range has been designated "Era 1" and figure 2.8 shows the observation efficiencies achieved during this era. The Q-band focal plane was cold ($T < 100$ mK) for 91% of the time, and we were observing the CMB with the VPM running for 58% of the time, slightly above the goal observation efficiency of 50%. 72.6% of the data taken during these CMB observations is flagged as "good" data, meaning it passes all our current cut metrics (more details in chapter 6). This amounts to 17,296 detector days of data. The bottom right inset of figure 2.8

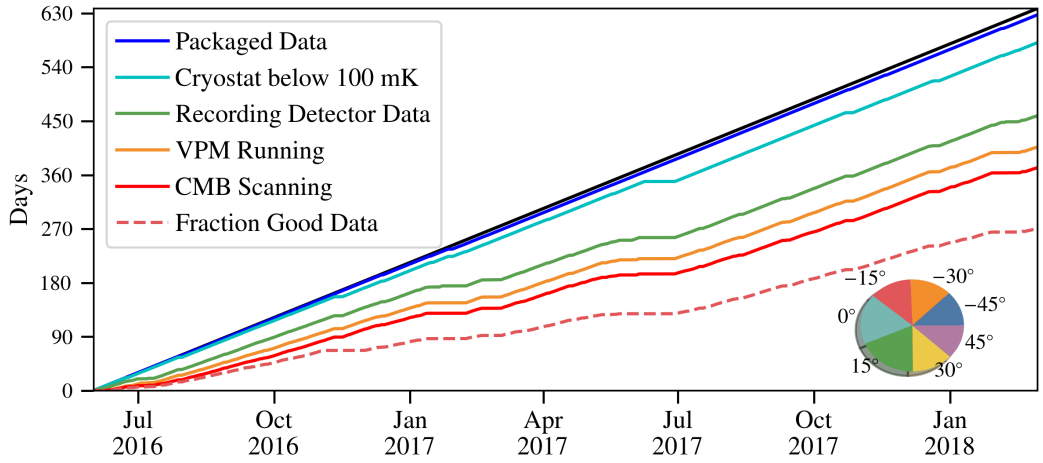

Figure 2.8: Various observation efficiency parameters for the first era of observing with the Q-band telescope. The cryostat remained cold for 91% of the time, while we were observing the CMB with the VPM running for 58% of the era (higher than the goal of 50%). The differences between the times spent recording data, the times the VPM was running, and the times the telescope was observing the CMB can primarily be accounted for by time spent on targeted calibration observations. The fraction of good data is calculated based on the number of live detectors passing all of the current cut metrics for the Q-band telescope.

shows the distribution of boresight angles when with telescope was observing the CMB.

Before deploying the W-band telescope, we acquired a new crane to significantly simplify the telescope assembly process and built a highbay work space to assemble more of the telescope components indoors. A new observation era began in June 2018, when the Q-band and first W-band telescopes commenced concurrent observations.

2.3.2 Mounts

The four CLASS telescopes share two telescope mounts that each have three axes of rotation: azimuth, elevation, and boresight. The boresight rotation is a key ingredient for rejecting systematic effects. The mounts are optimized to perform constant elevation scans where the mount slews in azimuth at 1°/s while pointed at 45° elevation.

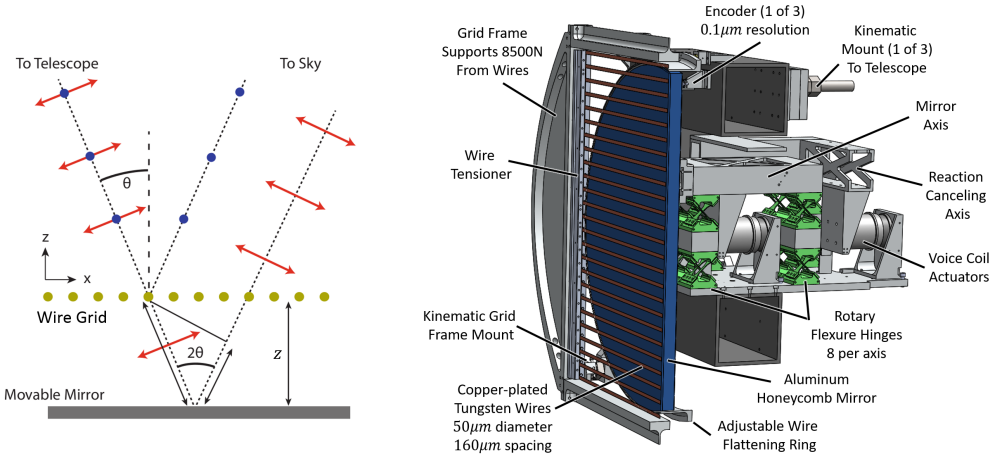

Figure 2.9: (Left) A schematic drawing of the a variable-delay polarization modulator as implemented by the CLASS telescopes. A stationary wire grid is held in front of a movable mirror to induce a phase delay between orthogonal linear polarizations. (Right) A section view of the complete CLASS VPM design.

Boresight rotations are performed in 15° increments along a range of $-45°$ to $45°$.

The azimuth axis has a maximum slew rate of $3°/s$ and a range from $-200°$ to $+560°$, while the elevation axis has a maximum slew rate of $1°/s$ and a range from 20° to 90° and the boresight axis has a maximum slew rate of $0.5°/s$. Each axis has an RMS pointing accuracy of 15 arcseconds. A co-moving ground screen and 1.5 meter (Q-band) or 3 meter (Q-band plus W-band) wide forebaffle is used to mitigate ground pickup.

Prior to being shipped to the CLASS site, the mounts were fully assembled in the highbay at Johns Hopkins University (JHU) Department of Physics and Astronomy. This assembly enabled a significant amount of integration tests to occur where it is easier to make changes to the setup.

2.3.3 Variable-delay polarization modulator

The most unique aspect of the CLASS instrument design is a variable-delay polarization modulator (VPM) in each telescope as the first optical element from the sky (Chuss et al., 2012; Miller et al., 2016; Harrington et al., 2018). Shown in figure 2.9, VPMs use a linearly polarizing wire grid in front of a movable mirror to induce a variable phase delay between polarization states parallel and perpendicular to the direction of the wires in the grid. This phase delay transforms the linear polarization at 45° with respect to the wires (Stokes Q or U) with circular polarization (Stokes V) as a function of the distance between the wire grid and the mirror. Setting the modulation at a rate faster than the rate of change of the sky or instrument creates a lock-in style measurement of the polarization at a particular point on the sky and greatly increases the stability of the demodulated data. The combination of the "lock-in" style stability afforded by the VPM together with CLASS's large FOV for simultaneously capturing the polarized sky over 200 deg^2 is a requirement to measure polarization on the largest angular scales.

A primary advantage of a VPM over other modulation technologies is that it straightforwardly scales to the large ($\sim$ 60 cm) size required for the first optical element. Since instrument polarization[4] ($T \rightarrow P$) after the VPM is unmodulated and does not affect the demodulated data, only modulated polarized ground pickup, polarization from the telescope baffling, or the VPM itself can influence the demodulated data. This significantly mitigates the level of $T \rightarrow P$ leakage observed in the CLASS telescopes. The combination of instrument stability and systematics rejection due to the front-end polarization modulation with a VPM enables the recovery of the

[4]Instrument polarization is the conversion of unpolarized light into polarized light by the telescope.

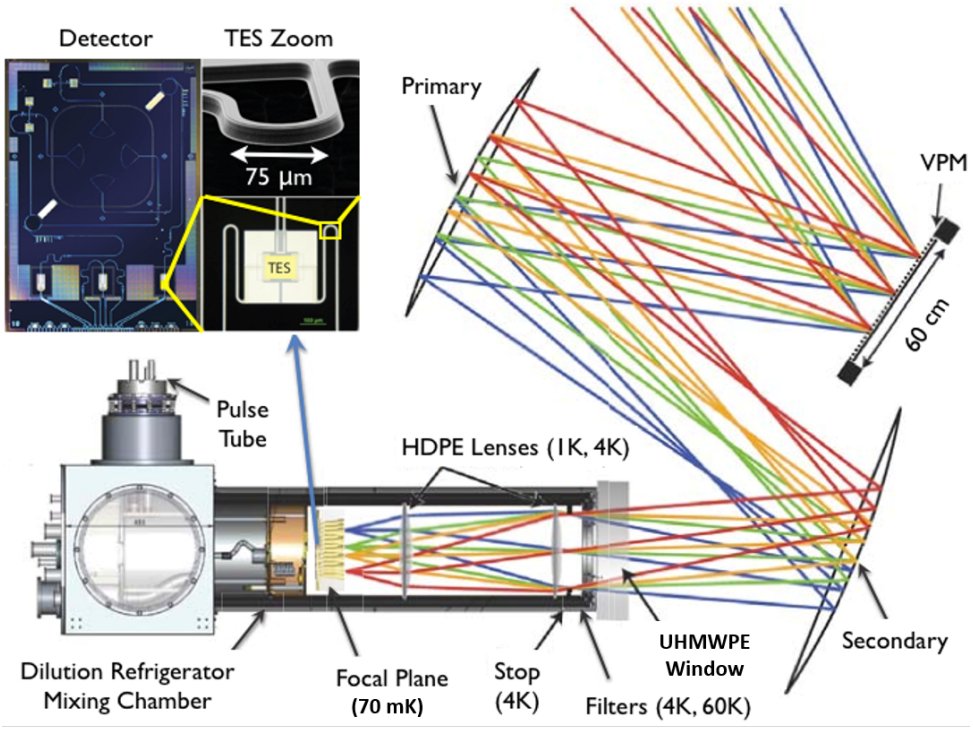

Figure 2.10: A CLASS Telescope. Each CLASS telescope is designed to minimize systematic effects while optimizing sensitivity. The figure shows a schematic with colored lines tracing the optical path for four beams. The VPM modulates the polarized sky signal (e.g., the CMB) and, *because it is the first optical element*, does not modulate instrumental polarization. Because atmospheric emission is not linearly polarized, it does not contaminate the signal. Mirrors and lenses focus the light onto the focal plane, which is continuously cooled to 40 mK in the dilution refrigerator-based cryogenic receiver. A highly-efficient polarization-sensitive detector defines the band-pass and measures the power of the linear polarization states with transition edge sensor (TES) bolometers.

largest angular scales of the CMB polarization from a ground based telescope(Miller et al., 2016). More information about the CLASS VPMs follows in Chapters 4, 5, 6.

2.3.4 Optics and Receivers

The CLASS telescopes share a common novel design, shown in Figure 2.10 (Eimer et al., 2012; Essinger-Hileman et al., 2014), with an approximately 200 deg^2 field of view and resolutions ranging from $18'$ (220 GHz) to $90'$ (40 GHz). The VPM is followed by elliptical $\sim$ 1 m diameter aluminum primary and secondary mirrors,

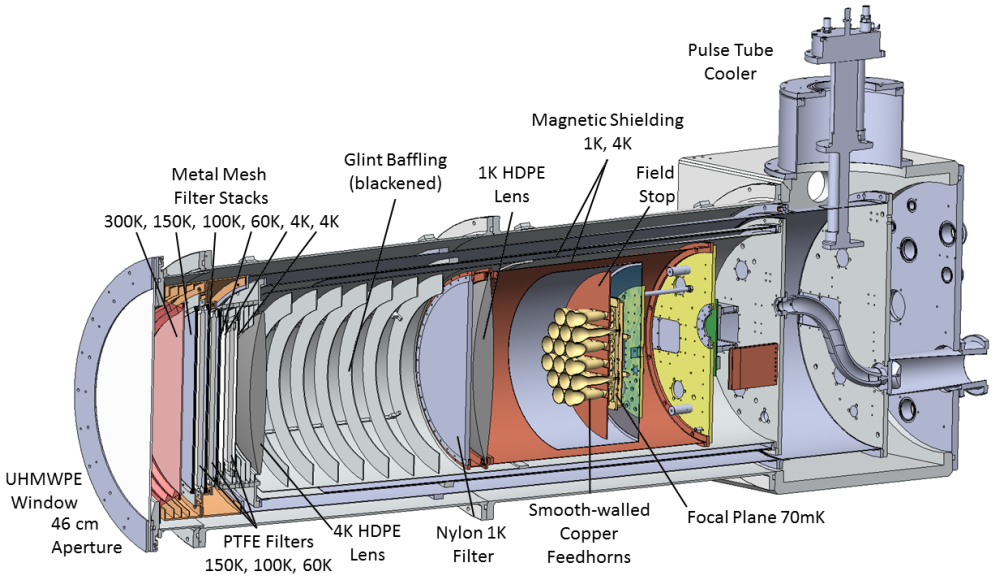

Figure 2.11: The 40 GHz receiver as it was fielded in early 2016. Vacuum is held over a 46 cm aperture by a 4.8 mm thick ultra-high molecular weight polyethylene window. Six multi-layer stacks of reflective metal-mesh filters interspersed between three polytetrafluoroethylene (PTFE) filters drastically reduce the loading from infrared radiation before the 4 K cold stop. Blackened glint baffling and a blackened field stop absorb stray light while two high-density polyethylene (HDPE) lenses image incident light onto the focal plane. The focal plane sits at 40 mK and is surrounded by two layers of magnetic shielding.

oversized to prevent warm spillover, that image the 4 K cold stop onto the VPM with low edge illumination (Eimer et al., 2012). Locating the VPM at a pupil ensures that each beam shares the same area of the modulator and thus common modulator response, while the reduced edge illumination eliminates systematics due to edge effects, including diffraction.

The CLASS telescopes use four custom cryostats built by BlueFors Cryogenics.[5] These cryostat receivers are necessary because the detectors, section 2.3.5, operate below 100 mK and the re-imaging optics must be held at cryogenic temperatures to minimize the emission from the dielectric materials. As shown in Figure 2.11, the cryostats contain a Cryomech PT415 pulse-tube cryocooler, which uses the expansion

[5]BlueFors Cryogenics, Arinatie 10, 00370 Helsinki, Finland, www.bluefors.com

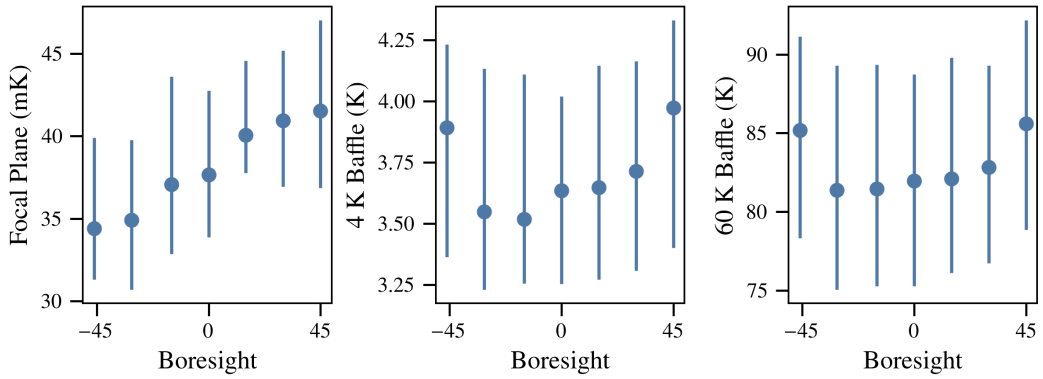

Figure 2.12: The median temperature of three of the cold stages (100 mK, 4 K, 60 K) during the first observing era, measured near the end of the stages where the optical elements are held. The error bars indicate the 1 σ widths of the temperature distributions at that boresight.

and compression of pressurized helium to cool stages at 60 K and 4 K. The pulse-tube has 40 W of cooling power at 40 K and 1.5 W of cooling power at 4 K. The cooling below 4 K is accomplished with a dilution refrigerator (DR), which exploits a phase transition in a ^{3}He/^{4}He mixture to achieve 100 mW of cooling power on a 1 K stage and 300 μW at 100 mK.

Each of the cold stages have different optical elements, such as lenses, filters or the focal plane, mounted on them. The CLASS cryostats are unique in that the cold stages are horizontally extended (figure 2.11) and that the pulse-tube and DR rotate with respect to gravity when the telescope moves with boresight. Figure 2.12 shows the median temperature of three of the cold stages ("100 mK", "4 K", "60 K") during the first observing era, where the error bars indicate the 1 σ widths of the temperature distributions at that boresight. For the 4 K and 60 K stages, the temperatures are recorded at the end of the stages near the relevant optical elements. The temperature of the focal plane varies with boresight, suggesting some change in the operation of the DR with gravity. The temperatures of the 4 K and 60 K stages are higher at

the boresight extrema, which indicates the performance of the pulse-tube, while still nominal, begins to degrade as it is displaced from vertical.

2.3.4.1 Window

The cryostat window must hold vacuum while having a minimal affect on the in-band radiation that transmits through the window and into the receiver. The 46 cm diameter window for the CLASS 40 GHz telescope is made of 4.8 mm thick ultra-high molecular weight polyethylene (UHMWP) that is anti-reflection coated with 1.6 mm thick sheets of porous polytetrafluoroethylene (PTFE). This window holds 8400 N of force from the atmosphere and, based on the level of bowing observed in the 40 GHz window at 5200 m, the 90 GHz telescopes have a thinner 3.2 mm UHMWP window that is also anti-reflection coated using porous PTFE. UHMWP is used as a window material because it is extremely transmissive in the microwave, however, it is also transmissive in the submillimeter and into the far-infrared. About 70 W of power enters into the cryostat though the window, the vast majority of which must be eliminated before the radiation reaches the coldest stages.

2.3.4.2 Filters

All CLASS telescopes use a combination of cryogenic reflecting and absorbing filters to reject the out-of-band power transmitted through the window and reduce optical loading on the detectors. For the 40 GHz telescope during era 1, six multi-layer stacks of reflective metal mesh filters, aluminum square grids on Mylar or polypropylene films, were used as low-pass filters to reflect over 75% of the incident infrared radiation back out the receiver window (Essinger-Hileman et al., 2014). A subset of these reflective filters were found to have higher than expected in-band reflection, so for

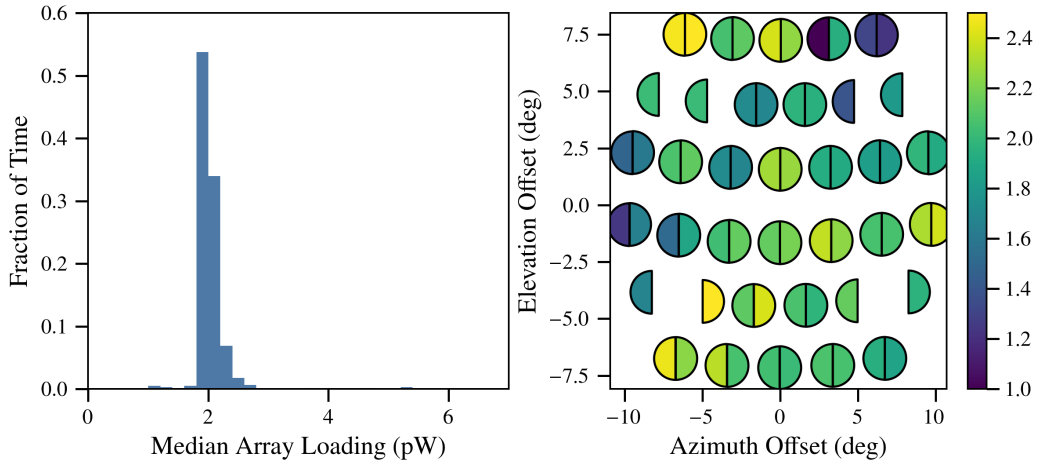

Figure 2.13: (Left) The median array loading for the Q-Band focal plane during the first era of observation. (Right) The median loading for each detector during the first era of observation, the right semi-circles are the detectors with $+45^\circ$ polarization angles while the left semi-circles are the detectors with -45° polarization angles. The units for the colorbar are pW.

the next observing era the number of reflective filters has been reduced to three and a stack of 10 extruded polystyrene foam (XPS) filters are used near the window. The 90 GHz telescope also uses three reflective filters and a stack of 10 XPS filters.

The 40 GHz and 90 GHz telescopes also use three PTFE filters, two on the 60 K stage and one on the 4 K stage, as well as one nylon filter on the 1 K stage to absorb above band frequencies. PTFE and Nylon absorb significant amounts of radiation in the terahertz and above, however, the loss in nylon is higher than that of PTFE closer to the CLASS bands. The 40 GHz PTFE and the 40 GHz and 90 GHz Nylon filters are anti-reflection coated using simulated dielectrics, a technique described in detail in Chapter 3. The 90 GHz PTFE filters are anti-reflection coated using heat pressed expanded sheets of porous PTFE.

Figure 2.13 shows the distribution of the median array loading on the left and the median loading for each detector on the right for the first era of observation for

the Q-band telescope. Here, loading is the amount of optical power incident on the detectors that is measured by a detector calibration routine at the beginning and end of each observation. The median of the median array loading during this era is 2.031 pW, which is close to what was originally predicted for the Q-band array and validates the filter scheme for the Q-band telescope. In addition, the tight spread in this value is indicative of the stability of the sky temperature around 40 GHz.

2.3.4.3 Lenses

The 40 GHz and 90 GHz CLASS telescopes each have two high-density polyethylene (HDPE) cryogenic lenses, one at 1 K and one at 4 K to re-image the incoming light onto the focal plane. The details of the manufacturing and anti-reflection coatings for these lenses are discussed in Chapter 3.

2.3.5 Detectors and Readout

The basis of the CLASS sensitivity is achieved through extremely sensitive transition edge sensor (TES) bolometers. TES bolometers use a thin film absorber (Mo-Au for the CLASS detectors) that is voltage biased to remain on a transition between superconducting and normal states. On this transition, the resistance of the material is a very strong function of temperature; power from the sky, deposited on the absorber, produces temperature changes which are read out as changes in the resistance of the material.

The CLASS detectors, fabricated at NASA Goddard Space Fight Center and shown in figure 2.14, are coupled to the incoming radiation using a smooth-walled feedhorn and a planar orthomode-transducer (OMT). The feedhorns for the Q-band and W-band telescopes are shown in figure 2.15 and 2.16, respectively. The feedhorn

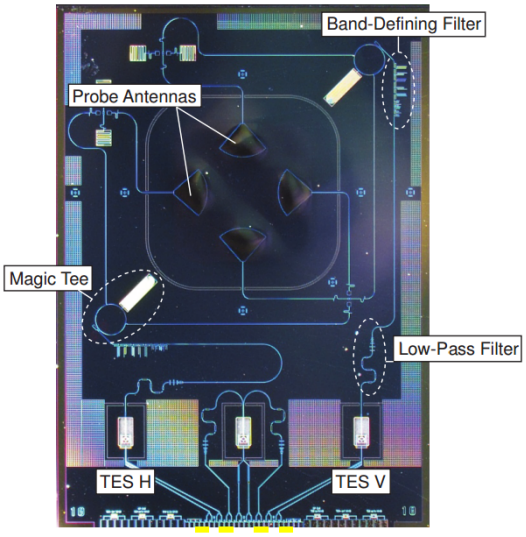

Figure 2.14: A single detector chip for the Q-band CLASS telescope. The orthomode-transducer (OMT), couples two orthogonal linear polarizations into the microstrip circuitry that is fabricated on low loss single crystal silicon. On chip filters define the frequency pass-bands for the detector. The remaining in-band power is deposited onto the transition edge sensor detectors where small changes in temperature result in resistance measurements that are read out using SQUID-based time domain multiplexing electronics.

and OMT couple two orthogonal polarizations onto planar microstrip transmission lines on single crystal silicon. An integrated quarter-wavelength backshort assembly completes the OMT and protects against stray light leakage. The monocrystalline silicon provides an extremely low loss dielectric for the microwave circuitry.

On-chip filters are used to define the detector bandpass, after which the powers from two linear polarizations are terminated onto two Mo-Au TESs with a transition temperature of $\sim$ 150 mK. More details about the CLASS detectors can be found in Appel et al. (2014), Rostem et al. (2016),and Dahal et al. (2018).

The CLASS 40 GHz focal plane includes 36 dual-polarization pixels mounted into a gold-plated copper baseplate. The left image in Figure 2.15 shows the completed 40 GHz focal plane mounted inside the 40 GHz receiver. Laboratory measurements

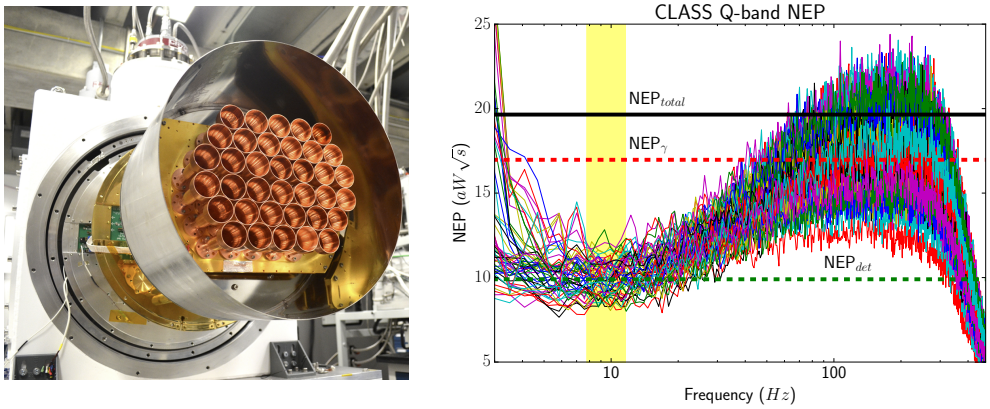

Figure 2.15: Left Figure: The fully integrated CLASS 40 GHz focal plane mounted in the cryostat receiver. **Right Figure:** The dark noise of the CLASS 40 GHz detectors. The average detector noise around the 10 Hz modulation frequency (green dashed line) is significantly lower than the expected noise due to optical loading on the detectors (red dashed line).

of dark detector noise are plotted in the right frame of Figure 2.15. The average dark detector noise around the 10 Hz modulation frequency (green dashed line) is significantly lower than the expected photon noise contribution (red dashed line) meaning each detector is background limited with an array sensitivity of 16 aW$\sqrt{\text{s}}$ (Appel et al., 2014).

The 90 GHz focal planes consist of seven hexagonal monolithic wafer modules with 37 dual-polarization detectors in each module. Figure 2.16 shows the completed focal plane for the first W-Band telescope and laboratory measurements of the dark detetector noise spectra. The array NEP for the first W-band telescope is 2.1 aW$\sqrt{\text{s}}$ (Dahal et al., 2018).

The changes in resistance at the TESs are read out using a type of low noise current amplifier called a superconducting quantum interference device (SQUID) that uses an inductor to measure the change in magnetic field associated with a change in current (Irwin et al., 2002). The low impedance of SQUIDs are what has made TESs such a

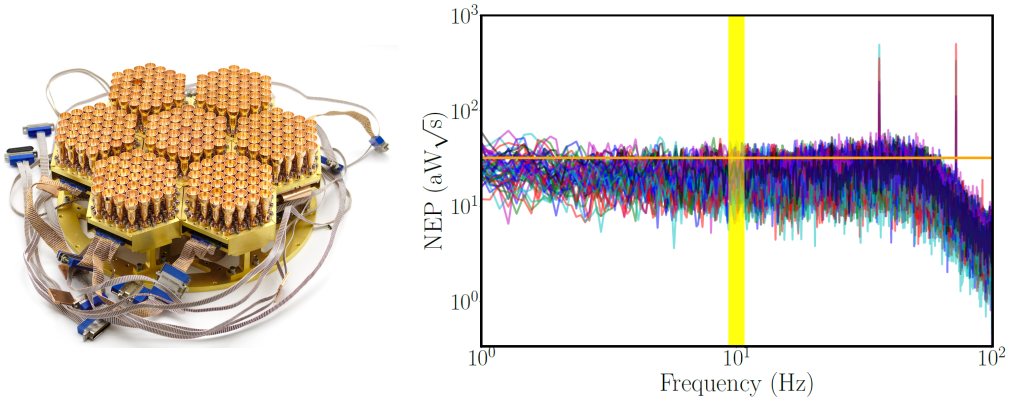

Figure 2.16: Left Figure: The fully integrated CLASS 90 GHz focal plane. **Right Figure:** The dark noise of one module of CLASS 90 GHz detectors. The orange horizontal line of 32 aW$\sqrt{s}$ indicates the estimated photon NEP for a single detector in the field. Noise spectra from Dahal et al. (2018).

viable high sensitivity detector option, there are two stages of SQUIDs in the CLASS setup, one set to readout the detectors and another at 4 K to further amplify the signal. The CLASS readout is time-domain multiplexed, where one SQUID is used to readout 11 channels, this reduces the number of wires and connections required to access all of the detectors.

Chapter 3

CLASS Cryogenic Optics

As discussed in chapter 2, the receiver for each CLASS telescope requires a set of cryogenic lenses and filters to re-image light onto the focal plane while blocking as much out-of-band light as possible. In addition to the reflective metal mesh filters, the Q-band and W-band CLASS telescopes use a variety of plastic cryogenic optical elements as absorptive filters and lenses. For these lower frequency telescopes, many plastics have reasonable indexes of refraction ($n \sim 1-2$) and are low-loss in-band while being lossy at submillimeter wavelengths (Halpern et al., 1986; Lamb, 1996). Therefore, the plastic optical filters will absorb out of band power and, as long as they are sufficiently cryogenically cooled, will not re-emit significantly in band. Also, the required diameters of these optical elements ($\gtrsim 400$ mm) make many alternative material choices (i.e. Silicon and Alumina) expensive and difficult to acquire and machine. Each Q- and W-band CLASS telescope uses three flat polytetrafluoroethylene (PTFE) filters and one nylon filter to reduce the out of band power on our detectors as well as two high density polyethylene (HDPE) lenses to re-image the light from the sky onto the focal plane.

All of these optics needed to be machined to the required optical specifications

and anti-reflection coated to increase the throughput of the telescope system. This chapter covers various infrared loss measurements used to inform filter design, the development and results of the machining procedure used to manufacture the lenses and various filters, and the design and machining of simulated dielectric anti-reflection coatings used for many of these optical elements.

3.1 Far IR FTS Measurements

One of the questions we had in the design of the cryogenic optics for CLASS is the in-band and out-of-band loss present in the materials, particularly at cryogenic temperatures where few measurements are made or published. Lamb (1996) has a compilation of index of refraction and loss measurements at microwave frequencies for a large variety of materials at a range of temperatures. One of the less constrained values in this set is the loss of Nylon at low temperatures. To investigate the loss through the far IR, the transmission of HDPE and Nylon were measured using a Fourier transform spectrometer (FTS) at NASA Goddard Space Flight Center. These measurements were performed at room temperature and then a subset were remeasured at 8 Kelvin, close to the operating temperatures of the materials in the CLASS telescopes (1 K and 4 K).

The FTS measurements result in a transmission spectra as a function of frequency (ν) or spectroscopic wavenumber ($k = 1/\nu$) for a given material, which can then be fit for the assorted material parameters. Following the notation in (Pozar, 2012), for a plane wave electric field incident on a flat slab of dielectric with index of refraction n,

the propagation coefficient and impedance are defined as

$$\begin{aligned} \gamma &= 2i\pi nk + ak^b \\ \eta &= \frac{2i\pi k}{\gamma}\eta_0, \end{aligned} \tag{3.1}$$

where k is the spectroscopic wavevector, a and b parameterize the loss in the material, and η_0 is the characteristic impedance of free space. With these definition the transmission coefficient and transmission of the plane wave through a dielectric of thickness τ is

$$\begin{aligned} t &= \frac{2}{2\cosh\gamma\tau + \left(\frac{\eta_0}{\eta} - \frac{\eta}{\eta_0}\right)\sinh\gamma\tau} \\ T &= t^\star t. \end{aligned} \tag{3.2}$$

Figure 3.1 shows the transmission spectra of four samples, two HDPE and two nylon, measured at 300 K. None of these samples were anti-reflection coated. The measured FIR transmission was fit to the transmission expected for a single dielectric slab, such as that described in equation 3.2, which was convolved with the resolution of the FTS. Because the observed transmission for nylon was so low for the thicker sample, a third thinner sample was also measured to more accurately constrain the material parameters. Using the three sample thicknesses for nylon at 300 K, the index of refraction and the loss were simultaneously fit to $n = 1.761^{+0.015}_{-0.018}$, $a = 1.25 \pm 0.09 \times 10^{-2}$ cm^{-1}, and $b = 1.92 \pm 0.02$.

Figure 3.2 shows the transmission measured by the FIR FTS as a function of wavenumber for three different nylon samples at 8 Kelvin. The transmission needed to be measured at cryogenic temperatures because nylon absorption decreases significantly with temperature and CLASS uses Nylon at 1 K. The shading around the

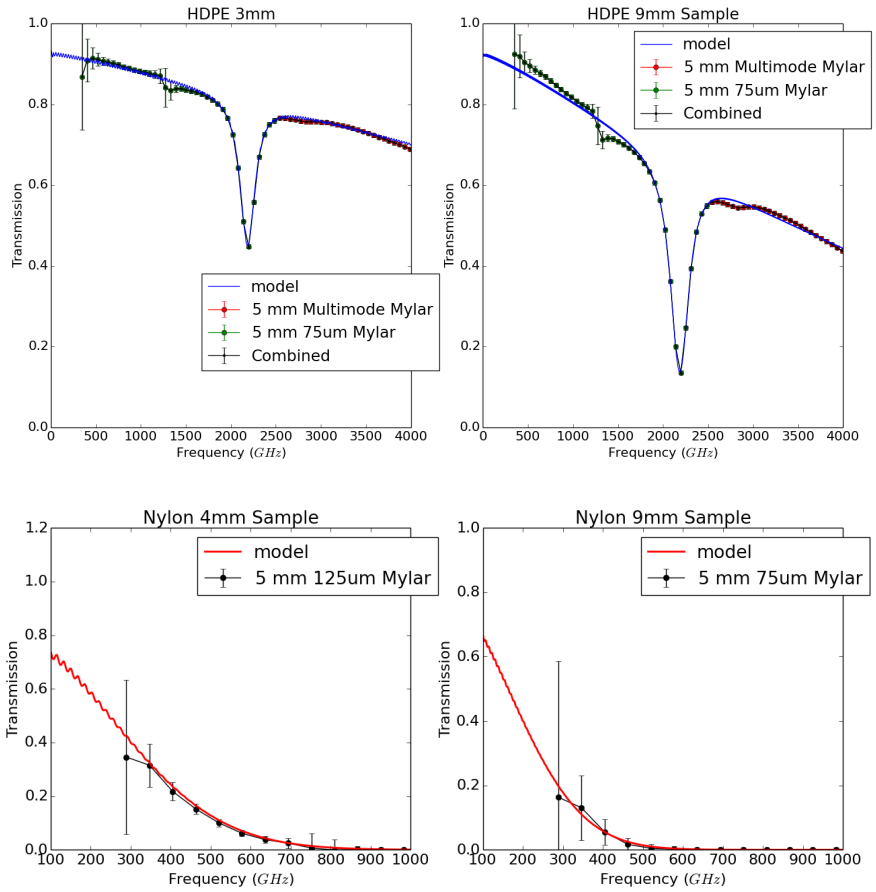

Figure 3.1: Warm FTS measurements for HDPE and Nylon at Terahertz frequencies. HDPE, the material used for the Q-band and W-band lenses, has a resonance feature near 2 THz but is very low loss, especially closer to the CLASS bands. Nylon is extremely lossy at room temperature and it was found that we needed thinner samples to effectively measure the material properties. The labels on the points denote the beam splitters used in the FTS, the type of beam splitter determines the level of sensitivity at different frequency ranges.

Parameter	3 Parameter Fit	2 Parameter Fit	2 Parameter - high k
n	1.608 ± 0.019	1.72 - Fixed	1.72 - Fixed
a (cm^{-1})	$6.74 \pm 0.34 \times 10^{-4}$	$6.69 \pm 0.37 \times 10^{-4}$	$11.13 \pm 0.74 \times 10^{-4}$
b	2.63 ± 0.02	2.625 ± 0.017	2.477 ± 0.019
χ^2_ν	1.75	1.49	0.585

Table 3.1: The material parameters extracted from the various methods of fitting to the nylon transmission curves.

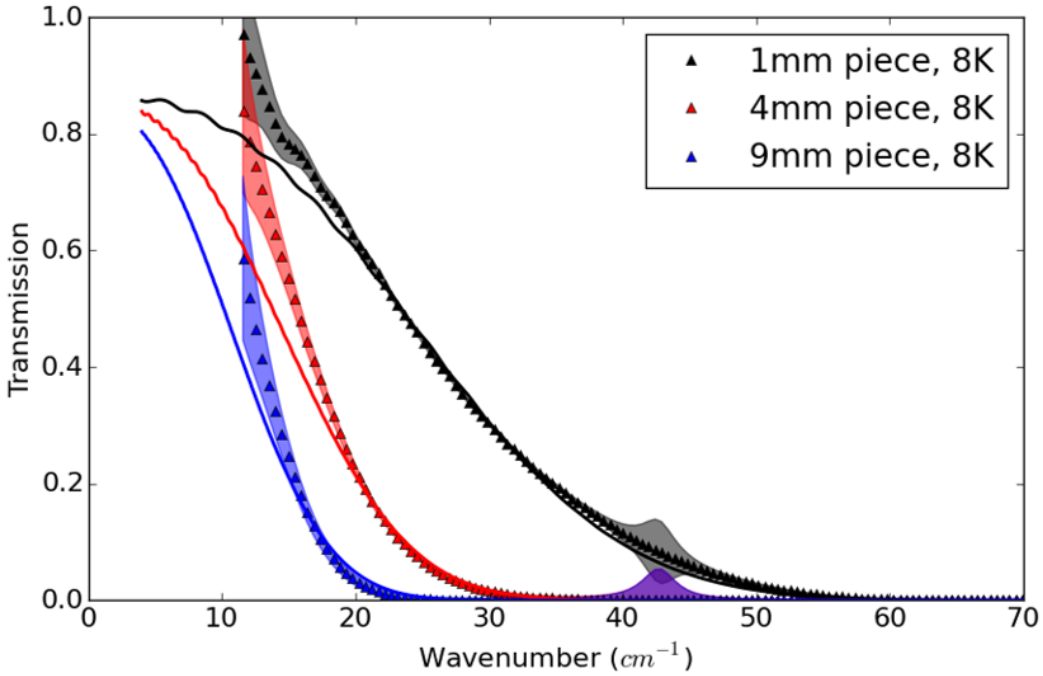

Figure 3.2: Transmission spectra of nylon taken with the far-IR FTS setup at NASA

points indicate the instrumental uncertainty associated with decreased sensitivity at low wavenumber. However, there is also something odd at lower wavenumbers because the transmission is near one for the thinner samples but does not appear to have turned over as one would expect. The transmission was fit using an MCMC to extract the index of refraction and loss for nylon at 8 K while marginalizing over uncertainties in the sample thicknesses. Table 3.1 lists the results for three different fitting schemes, one where all three parameters were simultaneously fit, one where the index of refraction was fixed to the value listed in (Lamb, 1996), and one where the index of refraction was fixed and the lower wavenumbers ($k < 20$) were excluded.

Fixing the index of refraction was motivated by the significant difference between the values fit at 8 K and at 300 K, a change that is no easily physically motivated. The only physically motivated change in index would come from the change in density

associated with length contraction at cryogenic temperatures, an effect that would increase the index instead of decreasing it. In addition, the part of the transmission curve that is most sensitive to index of refraction is where the FTS has reduced sensitivity and it is likely the errorbars on the points and extracted indexes are mis-estimated. Fixing the index to the value in Lamb, 1996 does not significantly change the resulting loss measurement, which is $\sim$ 20 times lower than the value at 300 K. The difference in loss between fits with all or a subset of the data does significantly change the resulting loss measurement, this could be because ak^b does not fully describe the loss in Nylon or the presence of other frequency dependent effects such as the efficiency difference due to sample surface roughness.

3.2 Anti-Reflection Coating Design

All of the refractive optics and filters used in a CMB telescope must be anti-reflection coated to reduce the loss due to reflections throughout the frequency range of the detectors. This is because the overall optical efficiency of the telescopes is directly related to the possible depth of the resulting maps. CLASS uses a simulated dielectric anti-reflection coating for many of the cryogenic optical elements, a technique using subwavelength holes cut into the surface of the optical element to create a layer of lower mean density. This process reduces the effective index of refraction of the material in the surface layer defined by the holes. This type of AR coating, which is a type of meta-material AR coating, was first used with plastics on the CAPMAP experiment (Barkats et al., 2005) and is also implemented with silicon optics in several experiments such as ACTPol (Coughlin et al., 2018) to create AR coatings for silicon lenses. Simulated dielectrics are an optimal choice of AR coating style for cryogenic

	Q-Band	W-Band
Center Frequency	38 GHz	92.5 GHz
Center Wavelength	7.388 mm	3.241 mm
Band Edges	33-43 GHz	77-108 GHz
Drill Diameter	1.511 mm	0.5334 mm

Material	Temperature of Interest	Index of Refraction at Temperture	Length Contraction at Temperature
HDPE	1 K and 4 K	1.564	2.0%
Nylon	1 K	1.760	1.4%
PTFE	4 K	1.440	2.15%
PMP	100 K	1.475	1.2%

Table 3.2: The top table lists the various parameters relevant to the design of simulated dielectric anti-reflection coatings for the Q- and W-Band CLASS telescopes. To simplify the machining and design procedure, the diameter of the drill bit used to create the holes was fixed once it was verified through simulation that it was sufficiently subwavelength. The bottom table lists the types of plastics where simulated dielectric coatings were designed, the expected temperature of the optical elements during operation in the CLASS telescopes, and the index of refraction and length contraction expected at the relevant temperature. AR coatings for polymethylpentene (PMP) were designed but not manufactured because the filtering plans changed over time.

optics because the AR layer is cut directly into the bulk material of the optical element and there is no risk of delamination or separation during cryogenic cycling. In addition, these AR coatings are significantly more tunable than options such as heat pressing sheets of lower density materials, enabling the creation of AR coatings which are perfectly matched to each material.

As a starting point for AR coating designed with cylindrical holes cut from a bulk material, the index of refraction of a layer is estimated by

$$n_{AR} = \frac{1}{a^2}\left[n_{\text{bulk}}a^2 + \pi r^2(1 - n_{\text{bulk}})\right], \tag{3.3}$$

where a is the pitch of the holes, r is the hole radius, and n_{bulk} is the index of refraction of the solid plastic. This requires the $2r < a$ and that $a \lesssim \lambda/5$. We only require a single layer AR coating for the Q-band and W-band telescopes, because the indexes of refraction of the materials (listed in table 3.2) are fairly low and the required bandwidth is modest ($\sim 25\%$). The optimal parameters for single layer AR coatings, which can be analytically calculated from reflection of a dielectric slab, are $n_{\text{AR}} = \sqrt{n_{\text{bulk}}}$ and a thickness of $\tau = \lambda_0/4n_{\text{AR}}$.

Simulations were done in an electromagnetic modeling program called HFSS[1] to model these type of anti-reflection coatings and optimize the parameters involved beyond the simple model described above. Figure 3.3 shows the half-space setup, where only one interface between the material and air is simulated. A half-space setup was used for these optimizations to ignore the Fabry-Pérot cavity effects that are present when there are multiple interfaces. A single cell the width of the simulated dielectric pitch a was created with alternating "perfect-E" and "perfect-H" boundary conditions to create input and output plane waves where the reflection and

[1] https://www.ansys.com/products/electronics/ansys-hfss

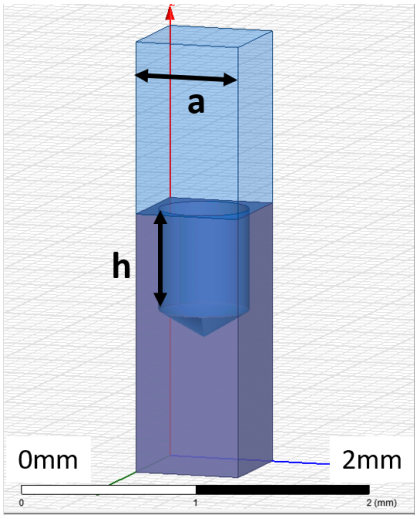

Figure 3.3: An example half-space setup used to optimize the simulated dielectric anti-reflection coating parameters. A cell the width of the grid pitch is created with alternating "Perfect-E" and "Perfect-H" boundary conditions to simulate plane wave transmission through the sample. Ports are set at the top and bottom of the cell as locations to measure the reflection and transmission off the sample. A cylinder with radius equal to that of the drill bit is cut out of the sample, along with a cone to account for the sharpened point of the drill bit.

transmission coefficients could be measured. A cylinder of radius r and height h are cut from the material along with a cone that was added to match the shape of the drill bit used for the machining of these layers. The dimensions of the drill bit were altered to account for the expected length contraction at cryogenic temperatures.

While HFSS has optimization routines capable of varying the values of a and h to maximize the transmission across the band, it was found that default gradient decent methods in the software did not converge well in the regime of high transmission encountered during the simulations. Likely because of the low indexes of these materials causing small changes in these parameters to not significantly change the results. Instead, simulations were run for a grid of a and h values to find the optimal parameters. To a large extent, the radius-to-pitch ratio of the simulated dielectric r/a controlled the index of refraction of the meta-material, and thus the maximum

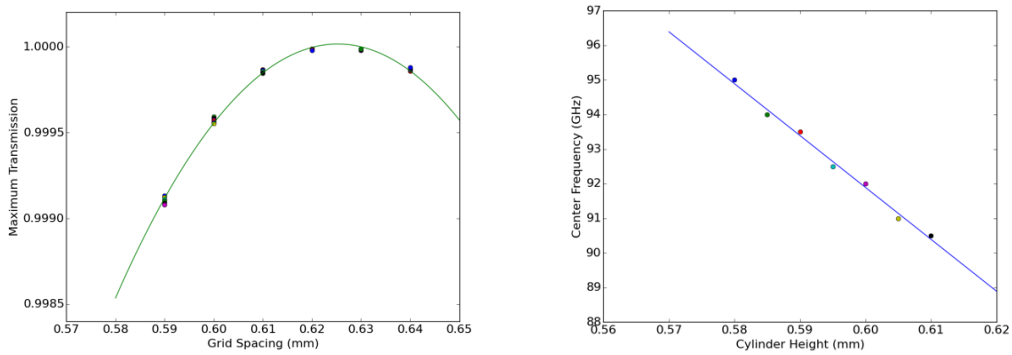

Figure 3.4: Left: The simulated maximum transmission as a function of the grid spacing parameter, this was fit to a quadratic function to find the optimal grid pitch. Right: The center frequency of the anti-reflection coating band as a function of cylinder height. The height was set so that the center frequency matched that of the telescope band.

possible transmission. An example of this effect is shown in figure 3.5. Once the effective index was set, the cylinder height h controlled the effective thickness of the layer, and thus the center frequency of the AR coating. The plots in figure 3.4 illustrate this effect for the HDPE simulations.

Table 3.3 lists the optimized height and pitch for each material simulated for each band and, where completed, also lists the effective dielectric layers necessary to input these AR coatings into an optics simulation software. It was found that these AR coatings were best modeled in an optics simulator as two-layer AR coatings, likely because of the cone at the bottom of each hole. To create these models, dielectric sheets of various thickness were simulated in HFSS with the meta-material AR coating on both sides of the sheet. Theoretical transmission spectra were calculated using 5

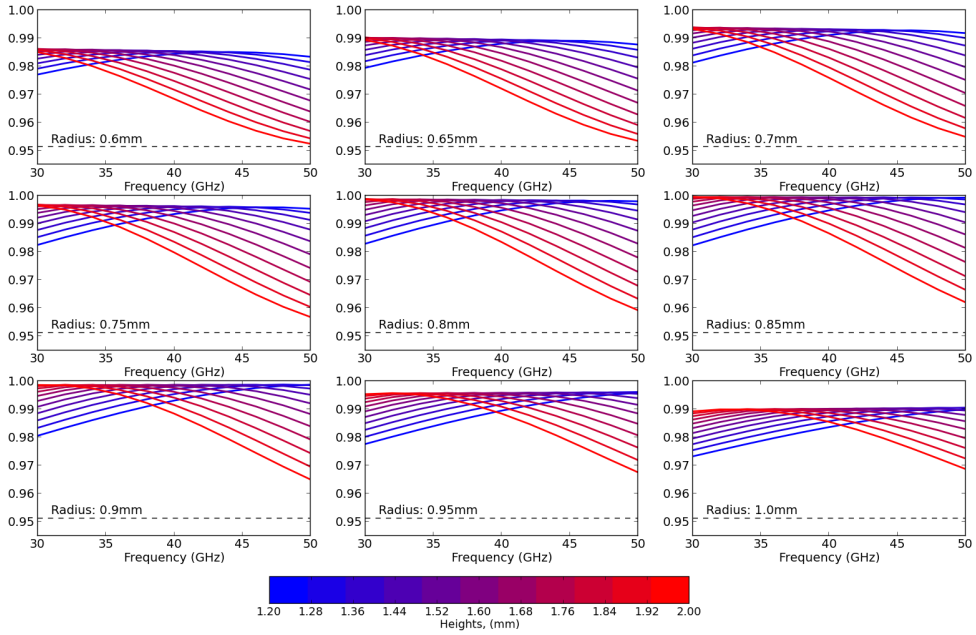

Figure 3.5: An example illustrating the optimization strategy for the simulated dielectric AR coatings. For this setup, the pitch, a was fixed and the transmission for a grid of r and h values were calculated with HFSS. Each plot shows the transmission curves for all the values of h for each radius. The ratio of radius-to-pitch controls the effective index of the meta-material and this determines the maximum possible transmission. Once the effective index of the material is set, the optimum height can be found to center the transmission on the band.

ABCD matrices[2] to model the different layers:

$$\begin{aligned}\left[ABCD_{\text{tot}}\right] = &\left[ABCD_{\text{AR,1}}(n_{\text{out}}, \tau_{\text{out}})\right] \cdot \left[ABCD_{\text{AR,2}}(n_{\text{in}}, \tau_{\text{in}})\right] \cdot \\ &\left[ABCD_{\text{bulk}}(n_{\text{bulk}}, \tau_{\text{slab}})\right] \cdot \left[ABCD_{\text{AR,2}}(n_{\text{in}}, \tau_{\text{in}})\right] \cdot \\ &\left[ABCD_{\text{AR,1}}(n_{\text{out}}, \tau_{\text{out}})\right].\end{aligned} \tag{3.4}$$

The transmission can then be directly calculated from the $ABCD_{\text{tot}}$. The simulated spectra were used to fit for all the variables except n_{bulk}. The resulting parameters were added to the optical model of the CLASS telescopes for a complete simulation of the expected throughput.

The AR coatings for the Q-Band simulated dielectrics were machined using a standard high speed steel drill bit, with a miniature center drill used to start the holes on curved surfaces. For W-band, the reduced diameter of the drill bit caused the high speed drill bit to wonder or deflect across flat surfaces and produced extremely uneven coatings. Experimentation with different machining strategies showed a carbide drill bit was stiff enough to produce accurate grids without center-drilling, even along the curved lens surfaces. For the Q-Band optical elements, with diameters $\sim$ 400 mm, these simulated dielectrics took approximately one day per side to machine using a customized Tormach PCNC 1100[3] mill at JHU. The W-band optical elements had over 300,000 holes to machine and took over four days per side. Figure 3.6 shows the simulated dielectric AR coating for the Q-band 1 K lens.

Q-band AR Coating Parameters						
	Optimization Results at Cryogenic Temperatures		Effective Dielectric Layers			
			Outer Layer		Inner Layer	
Material	Height (mm)	Pitch (mm)	Thickness (mm)	Index	Thickness (mm)	Index
HDPE	1.3926	1.836	1.3926	1.2468	0.2319	1.3626
Nylon	1.3865	1.724				
PTFE	1.5053	1.769				
W-band AR Coating Parameters						
	Optimization Results at Cryogenic Temperatures		Effective Dielectric Layers			
			Outer Layer		Inner Layer	
Material	Height (mm)	Pitch (mm)	Thickness (mm)	Index	Thickness (mm)	Index
HDPE	0.5897	0.6250	0.5897	1.2489	0.0638	1.3209
Nylon	0.5568	0.6210	0.55679	1.3254	0.0668	1.4430
PTFE	0.6164	0.6300	0.6164	1.1990	0.0658	1.2581
PMP	0.6345	0.6075	0.6075	1.2135	0.0667	1.2771

Table 3.3: The optimized simulated dielectric coating parameters for the Q-band and W-band plastic cryogenic optics. The grid parameters are listed at cryogenic temperatures listed in table 3.2 for each material. and needed to be adjusted for length contraction before machining at room temperature. Also listed are the values for dielectric layers which could be used to input these AR coatings into optics simulations of the complete telescope.

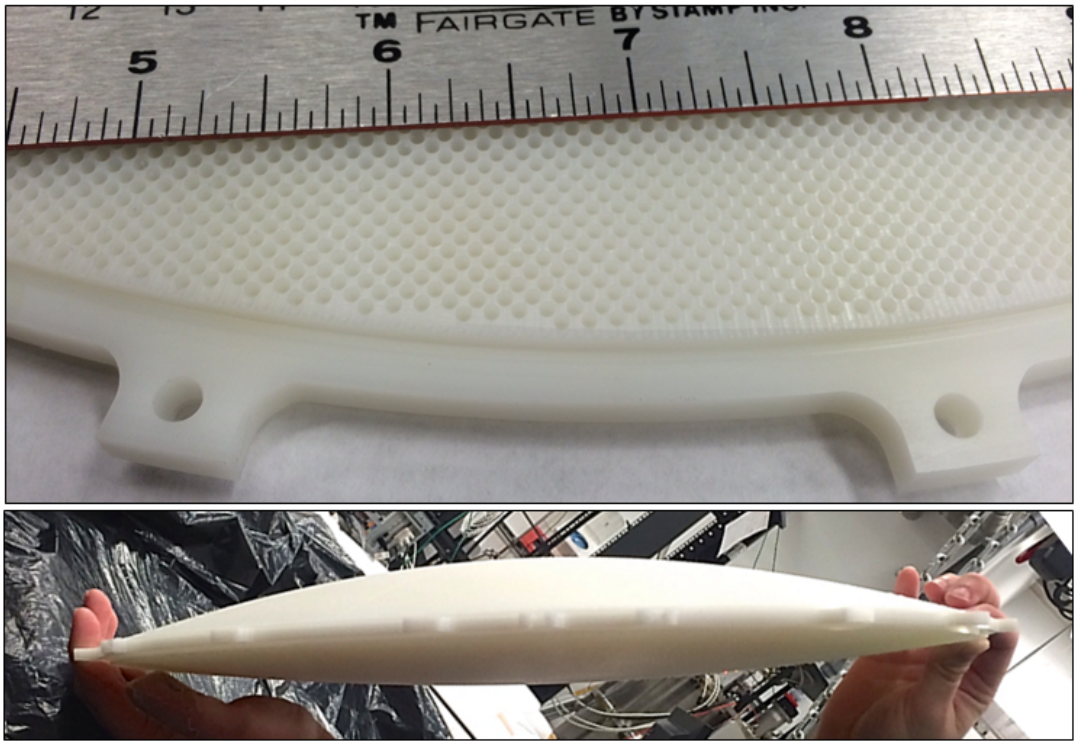

Figure 3.6: Top: A close-up image of the simulated dielectric coating for the Q-band lenses. Bottom: The profile of the completed 1 K lens for the Q-band telescope, which was $\sim$ 400 mm in diameter and $\sim$ 50 mm thick.

Surface Measurements for the Q-Band Lenses				
Type of Machining Error		Required Tolerance	1 K Lens Measured Value	4 K Lens Measured Value
Thickness		0.0078 in	0.0015 in	0.0002 in
Surface Error	Side 1	$\pm$0.005 in	$^{+0.003}_{-0.004}$ in	$^{+0.005}_{-0.003}$ in
	Side 2	$\pm$0.005 in	$^{+0.005}_{-0.002}$ in	$^{+0.004}_{-0.004}$ in
Face Tilt	Side 1	0.4°	0.004°	0.013°
	Side 2	0.4°	0.006°	0.011°
Face Decenter		0.012 in	0.0006 in	0.0011 in

Table 3.4: The machining error achieved for the Q-band lenses, as measured with a portable coordinate measuring machine. All measured errors are well within the tolerances allowed by the optical designs.

3.3 HDPE Lens Machining

Machining the HDPE lenses for the first three CLASS telescopes required some development to achieve the accuracy and precision necessary. The lenses are roughly 400 mm in diameter and 50 mm thick. It was discovered that sourcing high quality HDPE was import to creating these lenses as lower quality plastic was likely to contain or develop cracks. The diameter was larger than the y-axis travel on the CNC Mill we had so we developed a plan to use a rotational axis to machine the entire shape. There are two main challenges for machining plastics. First, large cuts ($\gtrsim$ 0.25 mm) are required because the material will deflect around the cutting tool if the cut is only removing a small amount from the surface; this can be accounted for with forward planning. Second, the material will significantly relax after cutting as stresses inside the polymers relax.

In order to reduce the amount of relaxation experienced after machining, the lenses were annealed twice during the process; once before any cutting has been completed and once after a "rough-cut" of the lens shape has been made. Annealing is the process of heating a material up close to its melting temperature (130 $^{\circ}C$ for HDPE), maintaining that temperature for a time, and then very slowly ramping the temperature back down. Holding the material at high temperature allows the material to release stresses and the slow cool down prevents new stresses from forming at room temperature. The annealing recipe for the 62 mm thick blocks of HDPE was: 4 hours to ramp the temperature to 120 $^{\circ}C$, hold at 120 $^{\circ}C$ for 48 hours, then ramp the temperature back down to 25 $^{\circ}C$ over 48 hours. Each anneal step took one week to complete. The final shape of the lenses were cut after the second annealing step

[2] See appendix C for details on ABCD matrices

[3] https://www.tormach.com/pcnc-1100/

and were measured with a FARO portable coordinate measuring arm. The time to machine and inspect the shape of the lenses was an additional 1-1.5 weeks. The entire procedure of anneal, rough cut, anneal, final cut, inspect, simulated dielectric machining, took approximately one month per lens for the Q-band lenses and six weeks for the W-band lenses. Table 3.4 contains the results for the two Q-Band lenses, which were well within the required tolerances for the CLASS optics.

Chapter 4

CLASS VPM Architecture

This chapter is almost entirely taken from Harrington et al. (2018).

This chapter covers the requirements, design, implementation, and performance of the VPMs for the first two CLASS telescopes (Q-band and the first W-band telescope). The Q-band VPM was installed at the CLASS site in the Spring of 2016 and was on sky until the Spring of 2018, when it was removed and re-installed. The first W-band VPM was installed in Spring 2018.

4.1 VPM design requirements

The scientific goals of the CLASS survey drive the design requirements for the CLASS VPMs. The B-mode signal from primordial gravitational waves is predicted to be higher than the gravitationally lenses E-modes on angular scales larger than about a degree on the sky; this sets the upper limit for the CLASS beamwidths. Since the VPM is the first optical element, the diameter of the VPM limits the beamwidth of the CLASS telescopes. The diffraction limit, $\theta \sim \lambda/d$, and the Q-Band center wavelength of 7.89 mm set the required diameter of the clear aperture for CLASS VPMs to $\sim$ 45 cm. The CLASS VPMs have been constructed with a 60 cm clear aperture to limit spill

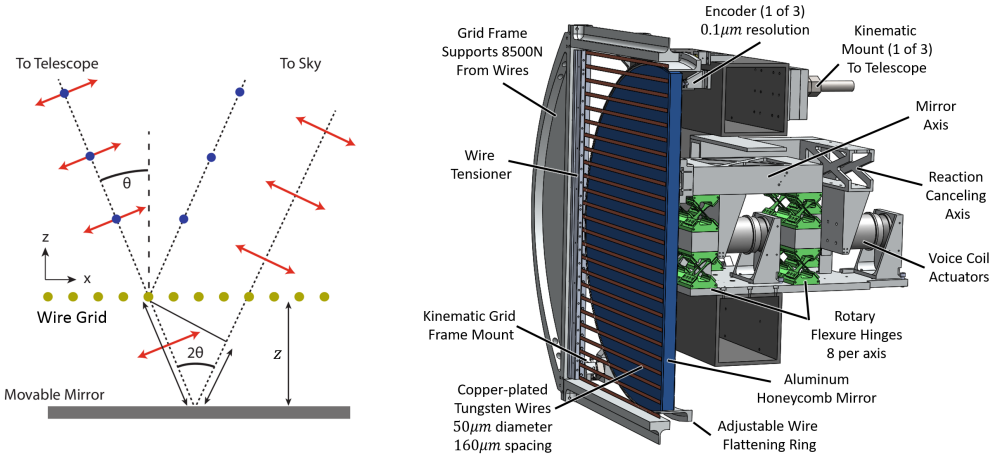

Figure 4.1: (Left) A schematic drawing of the a variable-delay polarization modulator as implemented by the CLASS telescopes. A stationary wire grid is held in front of a movable mirror to induce a phase delay between orthogonal linear polarizations. (Right) A section view of the complete CLASS VPM design.

and reduce systematic effects resulting from edge illumination of the VPM (Eimer et al., 2012).

A non-normal incidence is required since the VPM is a reflective device and normal incidence would require an obstruction, causing an unacceptable level of diffraction and instrument polarization in the system. However, non-normal incidence on a flat mirror produces a polarized signal that increases with angle of incidence, so it is desirable to keep the angle of incidence on the VPM as small as possible. CLASS has chosen to set the angle of incidence at 20° as a compromise between these two design constraints.

CLASS implements a polarization modulator to move the scan frequency to a region above the $1/f$ knee of the detectors and environment. The $1/f$ knee frequency depends on the thermal stability of the atmosphere, warm optics, and cryogenic receiver as well as the white noise level from the detectors. In addition, the modulation must be slower than the response rate of the detectors. Given these constraints and

the noise levels observed in Appel et al. (2014), the CLASS modulation frequency is set at 10 Hz.

4.1.1 Throw Requirements

Given the angle of incidence on the VPM and the band-pass of each detector, we can calculate the required throw, the grid-mirror distance range through which the VPM mirror moves, for each telescope. For an ideal VPM with a perfect mirror and grid, the single frequency, ν, phase delay between the two orthogonal linear polarization states is

$$\phi = \frac{4\pi\nu}{c} z \cos\theta, \tag{4.1}$$

where z is the distance between the grid and the mirror and θ is the angle of incidence. This causes mixing between one of the linear polarization states and circular polarization. If $+Q$ is defined as being along the wires of the VPM, then the polarization before and after the VPM is modulated as

$$\begin{aligned} U_{\text{out}}(\nu) &= U_{\text{in}}(\nu)\cos\phi - V_{\text{in}}(\nu)\sin\phi \\ V_{\text{out}}(\nu) &= U_{\text{in}}(\nu)\sin\phi + V_{\text{in}}(\nu)\cos\phi. \end{aligned} \tag{4.2}$$

The single frequency modulation is integrated over the band-pass of the detectors to calculate the total modulation function of the instrument. For the following calculations we assume this ideal model for the VPM with a top-hat band-pass for each detector. The band edges for the detectors are 33-43 GHz and 77-108 GHz for the Q-band and W-band telescopes, respectively. The frequency integration also assumes a source spectrum of a 2.725 Kelvin blackbody. The total modulation functions[1] for the CLASS Q-Band and W-band VPMs are shown in figure 4.2, where S_x describes the

[1]The modulation functions are the top row of the Mueller matrix for the combined VPM plus detector system, this takes polarization from the sky and returns the power observed by the detector.

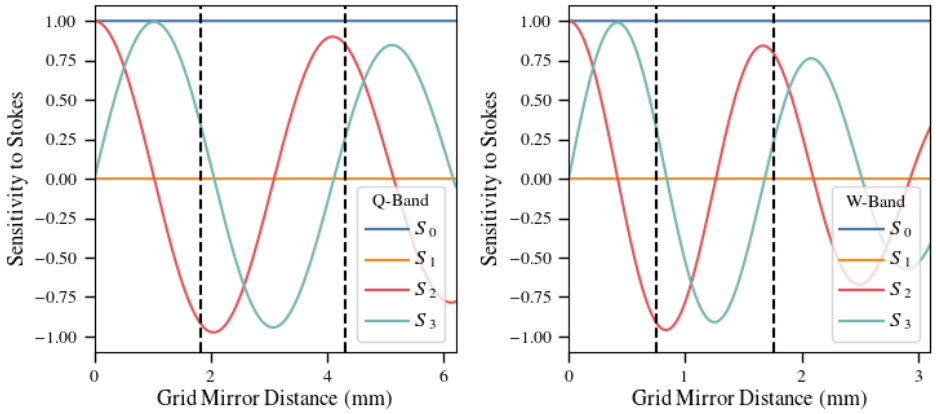

Figure 4.2: Modulation functions for ideal CLASS VPMs with a single linearly polarized Q-Band (left) and W-Band (right) detector aligned at 45° with respect to the wire grid at an angle of incidence of 20°. S_x refers to the detector's sensitivity to Stokes I, Q, U, and V respectively. The black dashed lines delineate the optimized mirror throw for each band.

sensitivity to Stokes I, Q, U, and V as a function of grid-mirror distance for a linearly polarized detector aligned at 45° with respect to the wire grid. The sensitivities are normalized to the intensity observed by a single linearly polarized detector.[2] The decrease in the amplitude of the peaks with increasing grid-mirror distance is a decoherence effect due to the finite band-pass of the CLASS detectors.

The VPM modulation produces a detector timestream, $P_{\rm det}(t)$, that depends on the modulation functions (S_x) and the polarization state of the incoming radiation

$$P_{\rm det}(t) = S_0\left[z(t)\right] I + S_1\left[z(t)\right] Q + S_2\left[z(t)\right] U + S_3\left[z(t)\right] V, \tag{4.3}$$

where $z(t)$ is the timestream of the grid-mirror distances for a chosen sinusoidal VPM throw.

For an ideal VPM with a detector aligned at 45° with respect to the VPM wires,

[2]The modulation functions in equation 4.3 are normalized by a factor of $\frac{1}{2}\frac{dP}{dT}$ which is accounted for in the absolute calibration of the detectors. This definition separates the effects of the VPM modulation from the absolute calibration of the instrument.

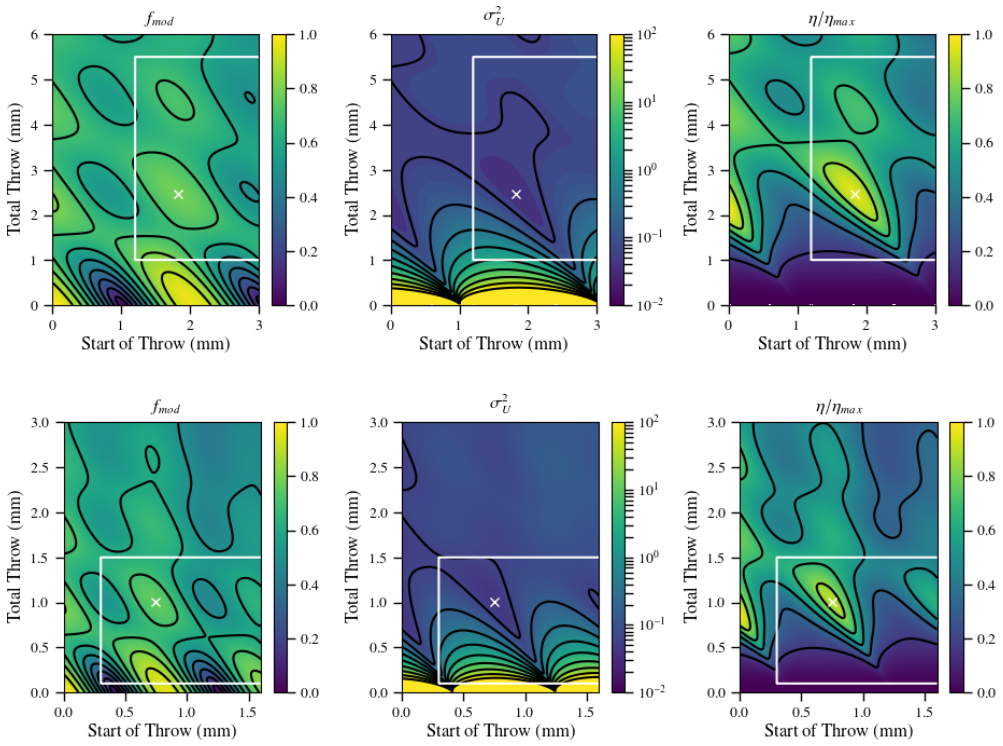

Figure 4.3: The modulation efficiency (left), uncertainty on U (center), and relative efficiency (right) for ideal CLASS-style VPMs with Q-band (top) and W-band (bottom) detectors over a range of mirror throw parameters. The start of the throw is the minimum distance between the grid and the mirror and the total throw is the peak-to-peak amplitude of the mirror motion. The white boxes indicate the regions accessible to the mechanical/electrical design of the CLASS VPMs, and the white X's mark the optimal throw parameters.

S_0 and S_1 are one and zero, respectively. Stokes V (circular polarization) is predicted to be zero for the CMB, so the optimum throw for the CLASS VPMs will maximize the time spent observing U while minimizing the uncertainty σ_U. The modulation efficiency is the mean sensitivity to Stokes U over the modulation cycle

$$f_{\mathrm{mod}} = \lim_{T\to\infty} \left(\frac{1}{T} \int_0^T S_2 \left(z(t)\right)^2 dt \right)^{1/2}. \tag{4.4}$$

The uncertainty on U depends on the number of points observed through the throw. For this we assume 40 points through the throw and set up a linear least squares fit

	Throw Start (mm)	Total Throw (mm)	Modulation Efficiency (f_{mod})	Relative Efficiency (η/η_{max})
Q	1.828	2.4775	0.7855	0.9561
W	0.7476	1.0107	0.7564	0.898

Table 4.1: The optimized VPM throw parameters for the Q-Band and W-Band CLASS VPMs. The differences in throw start and total throw are due to the wavelength shift between the two detector bands while the difference modulation efficiency and relative efficiency is entirely due to the difference in relative bandwidth.

where

$$\vec{d} = M\vec{S}, \quad M = \begin{bmatrix} S_0\left[z(t)\right] & S_2\left[z(t)\right] & S_3\left[z(t)\right] \end{bmatrix}, \quad \text{and} \quad \vec{S} = (M^T M)^{-1} M^T \vec{d}. \tag{4.5}$$

Here, $\vec{S}$ is the vector of Stokes parameters which are modulated by the VPM and observed by the detector in equation 4.3. The uncertainty on U is calculated using the (2,2) element of the inverse Fisher matrix

$$\sigma_U^2 = (M^T M)^{-1}_{22}. \tag{4.6}$$

These two metrics are combined into an observation efficiency $\eta = f_{\mathrm{mod}}/\sigma_U$. The optimal throw for a VPM is where η is maximized for the bandpass of the detectors. Figure 4.3 shows the modulation efficiency (f_{mod}), the uncertainty on U (σ_U), and the relative efficiency for a variety of throw parameters for the Q-Band and W-Band telescopes. The white box indicates the region of the plot accessible by the mechanical and electrical design of the VPMs. The highest peaks in the efficiency plot occur at zero path length difference and are not considered viable due to the fact that they would require contact between the mirror and the grid. Table 4.1 lists the optimized throw parameters, that are marked by a white X in figure 4.3. The differences in modulation efficiency and relative efficiency between the two bands are a consequence of the different detector bandwidths.

4.1.2 Alignment Requirements

The VPM mirror must be held extremely parallel to the wire grid throughout the entire throw of the mirror. To zeroth order, the tilt or parallelism error between the mirror and grid must be much less than the full width half max of the CLASS beams; however, it is useful to quantify this requirement to place design constraints on the VPM. A misalignment between the mirror and grid creates a pointing difference between the two surfaces; where a difference in temperature between the two directions leads to an additional term in the intensity modulation function

$$S_{0,\text{tilt}} = S_0 + \left.\frac{dT}{d\delta}\right|_{\delta_0} (\delta(z) - \delta_0) \tag{4.7}$$

where δ_0 is the pointing of the VPM grid and $\delta(z)$ is the pointing of the mirror across the mirror throw. From equation 4.7 it is clear that a constant tilt across the mirror throw will not be modulated by the VPM, meaning only changing tilts will cause a modulated temperature to polarization leakage ($T \rightarrow P$).

For a systematic modulated signal to influence the demodulated data, it must create a bias in the Stokes parameters fit using equation 4.5. The largest source of temperature fluctuations will be the atmosphere where, due to effective thickness variations as a function of elevation, a 10 K sky changes by ~ 69 μK/arcsecond at CLASS pointing of 45°. Simulating a timestream with equation 4.7 and fitting the output Stokes parameters with equation 4.5 gives $\Delta U = -30.5$ μK and $\Delta Q = -0.4$ μK per arcsecond of mirror tilt. This is a $T \rightarrow P$ leakage of 3×10^{-6} per arcsecond. To maintain a $T \rightarrow P$ leakage of less that 10^{-4}, the change in tilt across the mirror throw must be less than 30 arcseconds, and the lower the tilt is across the throw the lower the $T \rightarrow P$. The requirement of a changing mirror tilt of less than 30 arcseconds must

hold for all boresight rotations the CLASS telescope completes.

The realized $T \rightarrow P$ leakage will be less than described above because the effect can be reduced through various data analysis techniques. For example, the S_0 term used in the demodulation can be replaced with equation 4.7, or two detectors can be pair subtracted before demodulation to reduce the effect to the level of difference in the two beams.

4.2 Mirror Transport Mechanism

From the previous section, CLASS requires a VPM with a 60 cm mirror able to move through a range of up to 2.5 mm along the vector normal to its surface, at 10 Hz, with less than 30 arcseconds of variable tilt across the mirror throw. This mirror must be mounted $\sim$ 1 mm behind a fixed linearly polarizing wire grid which also requires a clear aperture of at least 60 cm. Both surfaces must be held at an angle of incidence of 20° (25° from vertical when observing at 45° elevation). These parameters must be maintained throughout $\pm$45° boresight rotations that change the direction of gravity by $\sim$ 20% at the VPM. This section describes the design and control of the Mirror Transport Mechanism (MTM) used to move the mirror, and section 4.3 describes the design and manufacturing of the wire polarizer.

4.2.1 Mechanical Design

Flexures are compliant mechanisms that use flexing or deflection to accomplish a desired outcome (Howell et al., 2013). There are countless types of flexures with one or more translational or rotational degrees of freedom where the dimensions,

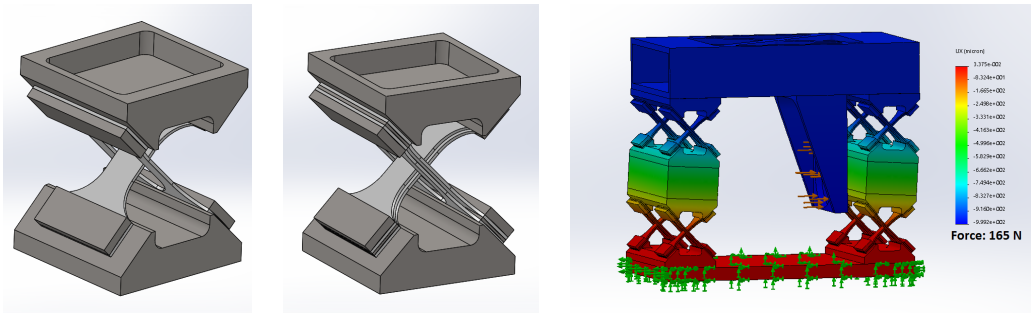

Q - Band W-band Four bar linkage Simulation

Figure 4.4: The crossed leaf rotary flexures used for the Q-band (left) and W-band (center) MTMs. The analytic description of these devices is in section 4.2.1 while the explanation of the differences is in section 4.2.3. The right image shows the 3D four-bar-linkage configuration used to connect the CLRFs under an example deflection simulation that was used to estimate the final mechanical properties of the MTM.

configuration, and materials can be engineered to achieve the exact level of compliance or constraint desired in every direction of motion. One key aspect of a flexural system is the motion and motion constraints are achieved with no contact or friction between parts. Assuming the forces on the flexure do not exceed the yield strength of the material, this enables extremely high wear resistance and repeatability over long-lifetimes.

The design requirements for VPM Mirror Transport Mechanisms (MTMs) are very well matched to a flexural mechanism with one translational degree of freedom. Previous VPMs designed for Hertz (Krejny et al., 2008) and PIPER (Chuss et al., 2014) both used double-bladed flexures to guide mirror motion. However, the larger total required throw and desired lifetime of > 5 years for the CLASS VPMs produced addition challenges and required a more complex flexure system.

CLASS VPMs use "cross-leaf rotary flexures"(CLRF) (Bal-tech, 2018) as a basic building block for the MTMs. These CLRFs are shown in the left and center images in figure 4.4 and use the deflection of two crossed leaf springs to create a rotation around

a pivot axis located where the springs cross. Basic leaf springs have a rectangular cross-section ($w \times t$ - width $\times$ thickness) with second moments of area of $wt^3/12$ and $w^3t/12$ when the force is along the thinner and wider directions, respectively. Since the second moment of area scales with the cubed thickness of the axis of deflection, setting $w >> t$ creates a spring with one rotational axis much stiffer than the other. For a cantilevered beam, the rotational spring constant is

$$k_{\phi,leaf} = \frac{Ewt^3}{6L^2} \text{ N/rad}, \tag{4.8}$$

where E is the elastic modulus of the spring material and L is the length of the deflected spring.The cross-leaf flexure configuration has two of these leaf springs in parallel, which doubles the spring constant, effective force is reduced by a factor of $\sqrt{2}$ since the expected force is only at 45° to the flexures. This gives a total CLRF spring constant of

$$k_{\phi,CLRF} = \frac{\sqrt{2}Ewt^3}{6L^2} \text{ N/rad}. \tag{4.9}$$

As shown in figures 4.1 and 4.4, the CLRFs are built into a parallelogram four-bar-linkage configuration where they are separated by a vertical distance, h, to translate rotations around the CLRF axes into horizontal displacement. The spring constant of the complete MTM is

$$k_{\text{x,MTM}} = \frac{\sqrt{2}Ewt^3}{3hL^2} \text{ N/m}. \tag{4.10}$$

where E is the elastic modulus of the spring material and L is the length of the crossed leaf springs. A variety of design constraints and considerations were used to determine the dimensions and materials of the MTM flexure:

Consideration 1 The material selection of the leaf springs sets the value for the elastic modulus in equation 4.10. The CLASS MTMs need to survive for 5 or more

years of operation while cycling at 10 Hz, requiring over 1.6 billion MTM cycles. To ensure survivability, we use wear-resistant blue tempered spring steel which is specifically tempered for applications such as the MTMs. Spring steel is only commercially available in specific thicknesses and dimensions, so we constrain our designs to use only these available options.

Consideration 2 The maximum required throw of the MTM, $\sim$ 2.5 mm, must be well within the linear regime of deflection for the spring steel straps to prevent plastic deformation. In addition, higher repetitive stresses applied to the steel straps result in lower lifetimes. Since CLASS requires a significant number of cycles we need to keep the stresses at a manageable level. For a given set of leaf spring dimensions, the spacing between the axes, h, can be increased to reduce the stresses imparted on the leaf springs while maintaining the off-axis rotational constraints.

Consideration 3 The selection of the axis drive system significantly influences the design of the flexure. The flexure could be driven by any type of linear actuator or a cam-type system coupled to any rotational motor. We chose a linear actuator because cams would require the entirety of the mirror throw to be physically designed into the system, which would prevent adjustments to the throw once the VPM was installed. In addition, the cams would be the only point of contact in the system and were likely to wear down with use while producing unnecessary vibrations in the system. Voice coil linear actuators, solenoids mounted in a magnetic field, are used to drive the MTMs because they provide a non-contact force which is linear to drive current and enable adjustments to the mirror positioning through calibration and commissioning of the instrument. The commercially available voice coils limited the maximum force which could be imparted on the MTM flexure and created an upper

bound for the possible flexure stiffness.

Consideration 4 The mirror, described in more detail is section 4.2.2, is the main source of mass and drag in the system. For a given maximum force output of the voice coils, the flexure needed to be compliant enough to move the mirror through the entire required mirror throw. This requirement needed to be achieved for all gravitational vectors encountered by the MTM over all elevation and boresight rotations.

Consideration 5 The combination of the mirror mass and MTM spring constant results in a resonance frequency for the system as a whole. Ideally, the resonance frequency is significantly higher than the drive frequency of the system. In practice, other constraints on the system such as the required mirror throw and drive selection push the resonance frequency lower than ideal. This has consequences for the mirror control and vibration suppression which are described in section 4.2.4.

The candidate system was simulated using the finite element analysis (FEA) software in Solidworks®. The right image of figure 4.4 shows the simulated deflection of the MTM mirror axis under a force applied at the voice coil mount that is through the center of mass of the mirror. This simulation was used to obtain a more precise prediction of the spring constant of the system and to verify that the linkages between the CLRFs were stiff enough to prevent any undesired deflections.

In addition, the simulation was used to extract the torsion coefficients for the mirror axis because the required alignment between the mirror and wire-grid creates a rotational constraint to torques for the MTM. For the two rotations of interest, the torsion coefficients were both $\sim 20 \times 10^6$ Nm/rad, which indicates a required torque of $\sim$ 100 Nm to produce one arcsecond of deflection. Since static deflections are unmodulated, the MTM would require *changing* torques of this order of magnitude

to produce these deflections which is well outside any expected forces during VPM operation. In addition, non-uniformities in the CLRFs cause non-uniform deflections which have to propagate through the steel and aluminum connections to influence the mirror tilt. For standard machining and assembly procedures with errors on the order of $\sim 50\mu$m, these deflections are small but non-negligible, and great care was taken to minimize assembly non-uniformities wherever possible.

The leaf springs were manufactured using a wire-cut electronic discharge machine (EDM). EDMing was used because it can produce higher precision parts than laser cutting or water jetting ($\sim$ 100 μin compared to $\sim$ 1000 μin) and causes less heat damage or metal warping during the machining. The leaf spring holders and clamps are CNC milled steel to match the leaf springs while the spacers between the CLRFs are aluminum tube stock, selected to maintain flexure stiffness while reducing the weight of the system. Each MTM flexure was assembled using alignment jigs and pins for the CLRFs to maintain uniformity between them at a level of 25 μm or better. The voice coil drives also required alignment jigs to achieve uniformity in the motor constants since misalignments create nonlinearities in the current to force ratio.

The mirror positions are read out using 0.1 μm resolution linear optical quadrature digital encoders[3]. Optical encoders were chosen because they are non-contact and have sufficient resolution for the mirror displacements required for the MTMs. In addition, quadrature digital encoders have a standard interface which allows for significant flexibility in controller hardware. Three encoders (see figure 4.1) are mounted on the back of the mirror to enable tip/tilt measurements of the mirror in addition to the mirror position. The encoders and tapes must be mounted parallel to the direction of motion of the mirror to prevent bias in the position readout.

[3]Renishaw ATOM^{TM} incremental encoder system with RTLF linear scale.

The deflection of MTMs were measured using the voice coils to apply forces and the encoders to read out position; an example of these measurements is shown in figure 4.6. The prediction of the MTM spring constant (equation 4.10) matches the final measured values to within 6%, validating that our simple MTM spring model is well motivated for understanding the trade-offs and design constraints in the system. The simulation calculated spring constant was within 4% of the measured value. Some of the difference between the calculated, simulated, and measured values is likely due to the calibration of the motor constant of the voice coil, which is not well constrained.

4.2.2 Mirror Selection and Mounting

The mirror is the largest source of mass and drag for the MTM system and therefore has important mechanical and dynamic effects in addition to its function as an optical element in the VPM. Optically, we require the mirror to be a flat mirror with low surface roughness, high reflectivity, and low emissivity. The CLASS VPM mirrors are constructed using aluminum sheet metal as the mirror face. Aluminum is chosen because of its manufacturability, durability, and high conductivity. We opted not to coat the mirror with copper or gold because the increased conductivity would have resulted in an improvement in emissivity of less than 3 mdB (see left plot in figure 4.5). The surface roughness of the rolled aluminum (8-16 μin) is sufficient to maintain the phase across the illuminated surface and, as shown in the right plot of figure 4.5 produces an acceptable emissivity of less than 0.2 mdB. Hence, no further processing of the surface is required.

Aluminum sheet metal alone is not stiff enough to maintain its shape under the

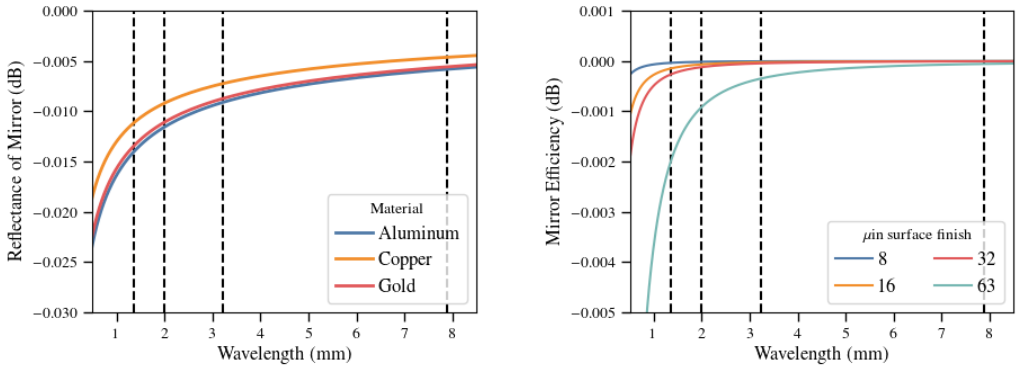

Figure 4.5: Left: The reflectance at normal incidence as a function of wavelength for three candidate mirror materials. The differences between aluminum and copper or gold was not sufficient to warrant the cost. Right: The mirror efficiency as a function of wavelegnth for various surface finishes. Surface finishes of 8-16 μin, standard finishes for rolled sheet metal, result in negligible effects in the efficiency from surface roughness.

oscillatory forces applied to the VPM mirror, so a honeycomb panel is used to significantly increase the mirror stiffness while minimizing the addition of weight. Various honeycomb panel manufacturing methods were used to determine the method which produced the best mirror. The mirror installed in the Q-band VPM was custom made using a 6.35 mm thick precision aluminum plate as a face sheet. The face sheet, honeycomb, and thinner back sheet were individually cut to a 61 cm diameter and then pressed into a panel. This fabrication method created a defocus in the VPM mirror which is visible in figure 4.15 and is large enough it would be unacceptable for the higher frequency mirrors. The thick plate as a face sheet was also heavy, causing issues for the control system. For the W-Band mirror, a 4 ft by 8 ft panel with a 1.27 mm thick face sheet was assembled using standard commercial practices and then 61 cm diameter mirrors were cut out of the panel. This method led to mirror faces that have flattness errors well below 25 μm and a significantly reduced mirror weight.

Each VPM mirror must be mounted perpendicular to the direction of motion, because misalignments will produce errors in the mirror positions read out by the encoders. Usually, mirrors have kinematic and adjustable mounts; however, the VPM mirrors were permanently epoxied onto the MTM to prevent the large, repetitive vibration forces from causing separation during operation.[4] To align the mirror to the MTM axis, adjustable alignment jigs, set in place using measurements from a portable coordinate measuring machine (CMM), were used to hold the mirror and mount while the epoxy was applied and allowed to cure. The misalignments between both the Q- and W-band mirrors and the MTM axes were at or below the level of systematic error expected from the CMM ($\sim$ 10 arcseconds).

4.2.3 Differences between Q-Band and W-Band VPMs

The difference in the VPM mirrors, described in section 4.2.2, is one of the changes made based on lessons learned from the development of the Q-Band VPM. The weight of the mirror and the compliance of the flexures combined to produce a resonance frequency that was too low (consideration 5, more details in section 4.2.4). While it was possible to create a working control system for Q-band under these conditions, it left the MTM sufficiently susceptible to external disturbances that it would have been problematic for the higher frequency telescopes where the minimum distance between the mirror and the grid (table 4.1) is significantly decreased.

In order to minimize the differences between the VPMs, methods of altering the CLRFs were investigated. The most straightforward way to increase the spring constant of the CLRFs was to increase the thickness of the leaf springs, but the required

[4]Optical alignment of the VPM to the rest of the telescope optics is performed using kinematic adjustments on the back of the VPM MTM mount, shown in figure 4.1, where the vibrations of the mirror motion have been canceled by the reaction axis and kinematic mounting is safer.

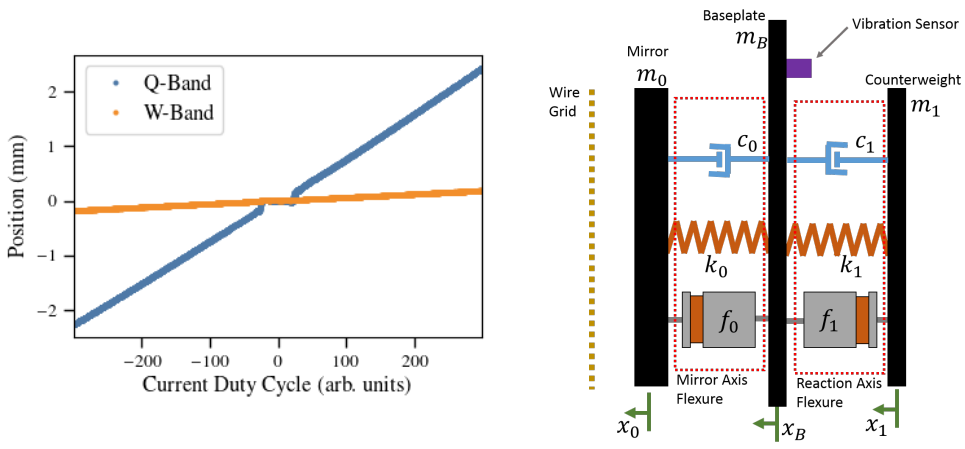

Figure 4.6: (Left) The MTM deflection as a function of current duty cycle (approximately equal to force) for the Q-band and W-band VPMs illustrates the factor of 12.5 increase in stiffness between the two designs. The Q-band curve also shows the dead-zone in the motor driver due to the large inductance of the voice coils interacting with the pulse width modulation in the driver. (Right) The mechanical equivalent diagram for the MTM flexure, which functions as a coupled damped mass spring system where the spring constants, k, are from the MTM flexures and the damping, c, and mass, m are primarily from the mirror and mirror counterweight.

increase was large enough that blue-tempered spring steel is not available in those thicknesses. Instead, as shown in figure 4.4, a second leaf spring was added to each original spring with a small spacer in between. It was found that the thickness of the spacer could be chosen to finely adjust the resulting spring constant and resonance frequency. The W-band MTM was made 12.5 times stiffer than the Q-band MTM. This was as stiff as possible given the available voice coil drives (consideration 3) and the weight of the W-band mirror (consideration 4). Figure 4.6 shows the deflection versus current duty cycle (∼force) for Q and W-band VPMs and illustrates the large increase in stiffness.

4.2.4 MTM Control

The control system for the MTM has two design objectives: move the mirror through the required throw at 10 Hz and cancel the impulses created by this motion. The

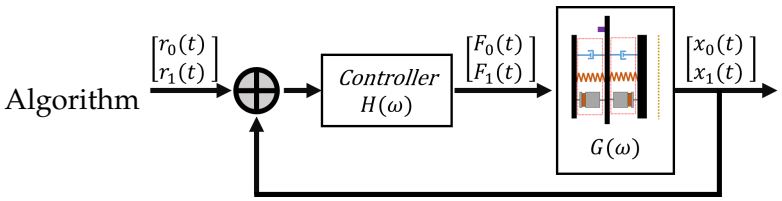

Figure 4.7: The outline of a generic control system where reference points r_x are fed into the system, a controller determines the forces output to the axes, and the resulting displacements are fed back to the controller and used the adjust the calculated forces.

impulse canceling is done with a reaction canceling axis (see figure 4.1) that surrounds the mirror axis and is as identical to it as possible. The reaction axis has a separate voice coil driver and encoder readout. Since both the mirror and reaction axes are constrained to move in only one direction, the small parasitic vertical vibrations created through the MTM rocking are deliberately ignored. Measurements of vibration levels for the fielded VPMs validated this decision as any parasitic vertical vibrations are much smaller then the external vibrational disturbances.

Figure 4.7 shows the layout for a standard time domain control system. The reference positions are input into a controller which has some transfer function $H(\omega)$ that depends on frequency. The controller calculates the required forces (currents) and sends them to the voice coils where the MTM has its own response, $G(\omega)$. The response of the MTM is then fed back into the controller to adjust the control to any external disturbances or drifts in the response of the system. $G(\omega)$, called the open-loop response function, can be calculated or measured from the dynamics of the MTM system. Once $G(\omega)$ is known, a controller $H(\omega)$ can be designed to control the motion of the axes.

Since the MTM is a flexure system that is completely non-contact and only experiences small deflections around the zero position, the dynamics are within the linear regime and can be described by linear control theory. The right diagram in figure 4.6

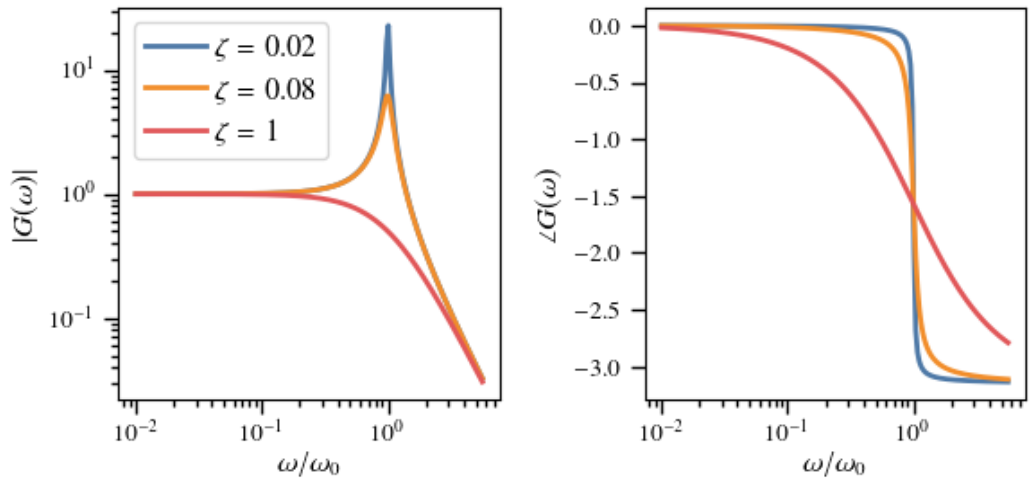

Figure 4.8: The amplitude (left) and phase (right) response of an example mass-spring system as described in equations 4.13 and 4.14.

shows the equivalent mechanical system for the MTMs, which functions as a coupled and damped mass spring system with two force inputs from the voice coils and two outputs from the encoders on the mirror[5] and reaction axes. The spring constants, k, come from the MTM flexure. The mirror has a mass, m_0, and is also responsible for much of the damping, c_0, experienced by the mirror axis ($c_0 \sim \pi r^2$). The reaction axis has a counterweight attached to the back of the flexure; this counterweight alters the damping c_1 of the reaction axis as well. External disturbances, such as vibrations from the telescope structure, enter the system through the baseplate of the MTM flexure. A vibration sensor is mounted to the baseplate to track vibrations induced by the MTM as well as any incoming external disturbances.

[5]There are three encoders mounted on the back of the mirror to enable measurements of tilts across the mirror. Since there is only one possible input to the mirror side, only one encoder is read out into the control system.

$$
\begin{aligned}
m_0\ddot{x}_0 &= f_0 - k_0(x_0 - x_B) - c_0(\dot{x}_0 - \dot{x}_B) \\
m_1\ddot{x}_1 &= f_1 - k_1(x_1 - x_B) - c_1(\dot{x}_1 - \dot{x}_B) \\
m_B\ddot{x}_B &= f_D - f_0 - f_1 - k_0(x_B - x_0) - k_1(x_B - x_1) \\
&\quad - c_0(\dot{x}_B - \dot{x}_0) - c_1(\dot{x}_B - \dot{x}_1)
\end{aligned} \tag{4.11}
$$

Equation 4.11 is the system of differential equations that describe the dynamics of the MTM. In the limit where $m_B \to \infty$ and $x_B \to 0$, the two axes are separate mass spring systems with well known dynamics. Since the equations are linear, it is straightforward to solve the simplified system for axis n with Laplace transforms and obtain the frequency response function (FRF) that depend on the system parameters k, c, and m and describe the response of the system to some sinusoidal input,

$$
G(i\omega) = \frac{X_n(i\omega)}{F_n(i\omega)/m_n} = \frac{1}{(\omega_0^2 - \omega^2) + 2i\zeta\omega\omega_0}. \tag{4.12}
$$

For a given sinusoidal input at frequency ω, $F_n(\omega)$, the sinusoidal output at that frequency is $X_n(i\omega)$ and can be directly calculated with the FRF. Both the amplitude and phase of this response are important to consider for the control of a system.

$$
\frac{X_{\text{amp}}}{F_{\text{amp}}/m}(\omega) = \frac{1}{\sqrt{(w_0^2 - w^2)^2 + 4\zeta\omega_0\omega}} \tag{4.13}
$$

and

$$
\phi_X - \phi_F = \tan^{-1}\left(\frac{-2\zeta\omega_0\omega}{w_0^2 - w^2}\right) \tag{4.14}
$$

respectively, where

$$
\omega_0 = \sqrt{\frac{k}{m}} \quad \text{and} \quad \zeta = \frac{c}{2\sqrt{mk}}. \tag{4.15}
$$

Figure 4.8 shows the amplitude and phase response of a system for different values

of ζ. The amplitude of the response determines the input force required to drive the axis at a specific frequency and if $\zeta << 1$ the amplitude response is maximized when ω equals the resonance frequency ω_0. The phase of the response determines how quickly the axis responds to changes in the input drive. Near the resonance frequency, the phase response of the axis shifts from in phase with the drive to out of phase with the drive and the value of ζ controls the rate of this change.

Figure 4.9 shows the Q-band (top) and W-band (bottom) frequency response functions that were measured at the CLASS site, where the drag on the mirror is reduced due to the lower air pressure. The response of the mirror axis to the mirror drive and the reaction axis to the reaction drive shows that the MTM designs are under-damped ($\zeta << 1$) with resonance frequencies twice (W-band) or below (Q-Band) the drive frequency of 10 Hz.

$$\begin{aligned} \omega_{0,Q} &< \omega_{\text{drive}} \qquad & \Delta\phi_Q(\omega_{\text{drive}}) &\sim -180^\circ \\ \omega_{0,W} &\sim 2\omega_{\text{drive}} \qquad & \Delta\phi_W(\omega_{\text{drive}}) &\sim -5^\circ \end{aligned} \tag{4.16}$$

The resonance frequency of the Q-Band MTM was the main reason for the design changes made to the W-Band MTM (described in section 4.2.3). With a phase response of $\sim -180^\circ$, no time-domain controller could produce a stable response at the drive frequency because feedback into the system would be out of phase with the drive. For W-band, a 5° phase response means a time-domain feedback control system could be created, however strong filtering must be implemented to prevent the nearby resonance from causing instabilities. In lab tests, the level of filtering required to negate the mechanical resonance of W-band reduced the bandwidth of the control system to below drive frequency. With the significantly reduced bandwidth, the controller was unable to cancel external disturbances and often increased the level of

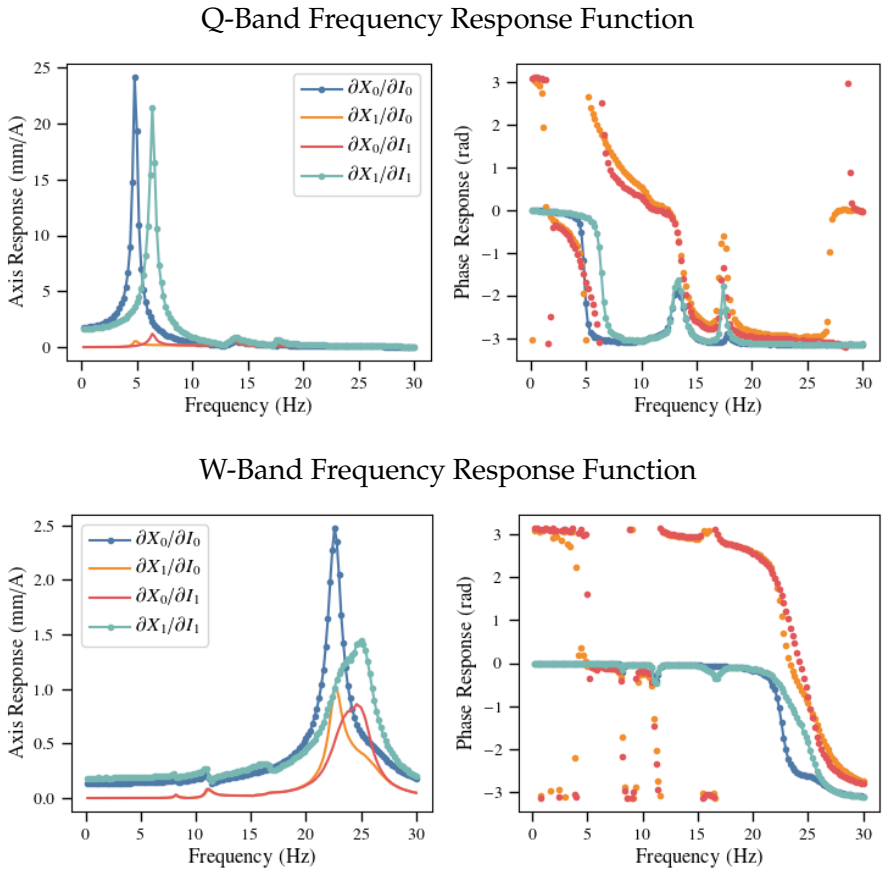

Figure 4.9: The measured frequency response functions of the Q-band (top) and W-band (bottom) MTMs, taken at the CLASS site before the installation of the wire grid. $\partial X_i/\partial I_j$ labels the response of the i^{th} axis to the drive of the j^{th} axis where 0 is the mirror axis and 1 is the reaction axis. The increase in MTM stiffness and decrease in mirror weight for the W-band VPM increased the resonance frequency by a factor of ~ 4.5 and reduced the resonance height by a factor of ~ 10. The response of one axis to the drive of the other indicates the axes are not completely independent and that the mounting structures had a finite stiffness. The smaller features in the response are due to the VPM coupling to the mounting utilized for these measurements.

the disturbance through a delayed response. For both MTM designs, a controller that tried to follow a set-point sinusoidal path in time was not possible or not useful.

Another factor to consider for the control system is that, in practice, m_B is large but finite. The motion of one axis influences the other and external vibrations from forces such as the wind on the telescope transmit through the baseplate. This is visible in figure 4.9 where both the mirror and reaction axes have responses to the other axis's drive. There are small features in all the responses which are evidence of resonance frequencies in the support system the VPM was attached to during the measurements.

Since a time-domain control system was not feasible for either MTM, a frequency-domain control system was developed to drive the axes at a single frequency while ignoring all others. This was possible because observability for the CLASS VPMs is more important than controllability.[6] Demodulation requires knowledge of the positions of the mirror as a function of time; it does not require that those positions be precisely a pre-determined function of time. The use of frequency-domain control does prevent the MTM control from actively reducing external disturbances input on the MTM, meaning all vibration canceling of external impulses is passive and determined by the frequency response function of the MTM.

The MTM controller uses an input amplitude and DC offset for each axis along with a relative phase between the axes to create sinusoidal drive currents for the voice

[6]Observability is the ability to know or measure the state of the system while controllability is the ability to move the axes to a particular location in a particular amount of time with some limit on the allowed error. Having sufficient observability of the axis vibrations does require that the output positions are sufficiently sampled to detect them. The VPM positions are read out synchronously with the detectors at 200 Hz which enables the detection of vibrations below the 100 Hz Nyquist frequency. Since the MTM is a mass spring system it functions as a low-pass filter, and significant vibrations above the resonance frequency do not occur.

coils,

$$I_0(t) = I_{amp,0}\sin(\omega t) + I_{dc,0}$$
$$I_1(t) = I_{amp,1}\sin(\omega t + \phi_I) + I_{dc,1}. \tag{4.17}$$

Unless otherwise specified, axis 0 is the mirror axis and axis 1 is the reaction axis. The controller then observes the resulting axis motion and fits the responses to sine waves of the same frequency,

$$x_0(t) = x_{amp,0}\sin(\omega t) + x_{dc,0}$$
$$x_1(t) = x_{amp,1}\sin(\omega t + \phi_x) + x_{dc,1}, \tag{4.18}$$

to measure the output amplitudes, phases, and offsets from the MTM. This produces a control system that has five inputs, $\vec{X}$, and five outputs, $\vec{I}$,

$$\vec{I} = [I_{\mathrm{dc},0},\ I_{\mathrm{dc},1},\ I_{\mathrm{amp},0},\ I_{\mathrm{amp},1},\ \phi_I]^T$$
$$\vec{X} = [X_{\mathrm{dc},0},\ X_{\mathrm{dc},1},\ X_{\mathrm{amp},0},\ X_{\mathrm{amp},1},\ \phi_X]^T. \tag{4.19}$$

Assuming this is a linear system, these quantities are related by a system matrix,[7] $\vec{X} = A\vec{I}$. At each step, the change in input current values is calculated as $\Delta\vec{I} = -K(\vec{R} - \vec{X})$, where K is the feedback matrix and $\vec{R}$ is the reference positions defining the VPM throw parameters. In this setup, K is also the inverse of the system matrix, and can be directly measured with the MTM. Figure 4.10 shows an example of the tests used to measure the system matrix for the Q-band MTM, where one input variable was swept across a range of interest and the response of all the output variables was recorded. This type of measurement indicated the system was not completely linear, so subsequent tests were conducted around the set operating points of the MTMs to linearize the system. The feedback matrices of the MTMs can be directly calculated

[7] The system matrix described here is not the standard definition of a system matrix used in control theory, where it is usually defined as $\dot{\vec{x}} = A\vec{x} + B\vec{u}$ with $\vec{x}$ being the the state vector and $\vec{u}$ being the inputs to the system.

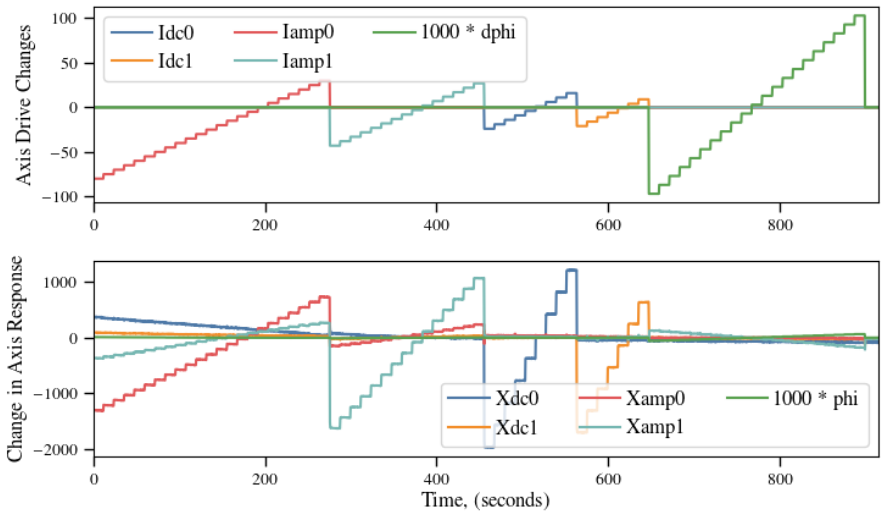

Figure 4.10: An example of the convenient tuning test used to measure the feedback matrix in equation 4.20, each of the controller inputs were varied across a range centered on the expected operating point while the response of all the outputs was recorded. This process was performed iteratively to obtain a final value for the feedback matrix used during scientific observations. This example is from the Q-band MTM where the covariance in the response is quite significant.

from these tests using

$$K = X_t^T I_t (I_t^T I_t)^{-1}. \tag{4.20}$$

where I_t and X_t are matrices with each row containing the input and output variables of the control system for each time step.

The off-diagonal terms of K are significantly higher for the Q-Band MTM compared to the W-Band MTM, this is likely due to the mechanical dynamics of the MTM and the relation between the drive frequency and the resonance frequency. The off-diagonal terms for Q-Band are large enough that using a diagonal matrix for K is unstable. It is possible to use a diagonal matrix for the W-band MTM; however, the full feedback matrix produces faster settling times and better noise rejection.

4.2.4.1 Controller Selection

As the development of the MTM control system progressed, it was determined that most commercial controllers were not designed for the type of control system required by the MTM. The controllers that were used initially assumed that current was proportional to velocity by default and did not have the available computational capabilities to quickly calculate the output variables for the control system. In particular, the computation rates for fitting the response of the axes limited the bandwidth of the control system to ~ 0.5 Hz. These limitations led to the development of custom controllers for the CLASS MTMs built around the OSD3358 system-in-package,[8] which includes a 1 GHz ARM Cortex-A8 processor and 512 MiB of RAM, providing ample computational resources to run the control code using a real-time operating system. The chip also includes dedicated hardware peripherals for reading in the MTM's quadrature encoders and an Ethernet interface for command input and telemetry. To actuate the voice coils, the controller includes a pair of H-bridge coil drivers with current sensing capabilities. A high sensitivity 3-axis accelerometer is used for tuning the reaction canceling axis, a process that is described in section 4.2.5. The new controllers increased the control bandwidth to ~ 2.5 Hz and this bandwidth is no longer limited by the controller capabilities.

4.2.5 Vibration Suppression

The impulses created by the mirror motion are significant and must be canceled to avoid unnecessary stress on the telescope structure. This is accomplished with the reaction canceling axis of the MTM. The control settings for the reaction axis

[8] Octavo Systems, https://octavosystems.com/

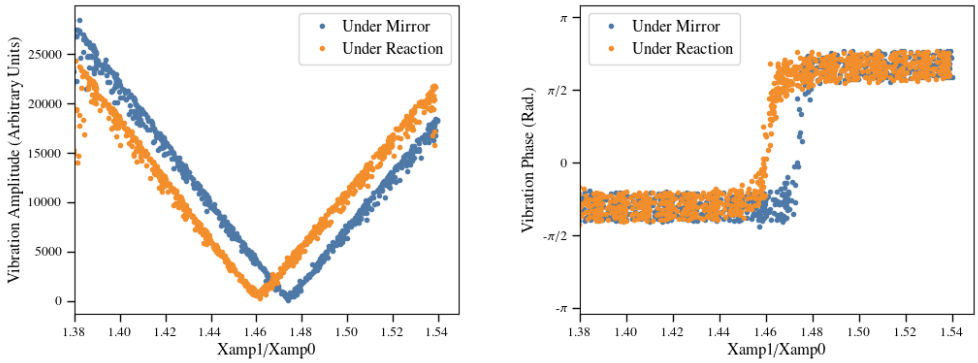

Figure 4.11: The amplitude and phase (relative to the mirror axis position) of the vibrations measured for the Q-band VPM with the accelerometer positioned at different places on the MTM flexure baseplate. These measurements indicate that the vibrations can be significantly canceled using the correct setting for the reaction axis relative to the mirror axis and that the placement of the accelerometer during this tuning is important for canceling vibrations at the correct locations within the telescope structure.

determine the level of vibration canceling and must be correctly tuned.

Looking back at figure 4.6 and assuming this simple model of the mechanical setup, the vibrations from the MTM will be zero when $\ddot{x}_B = 0$. If the mirror and reaction axes are identical ($k_0 = k_1$ and $c_0 = c_1$) and moving at 10 Hz with amplitudes of $X_{\text{amp},0}$ and $X_{\text{amp},1}$ respectively, then $\ddot{x}_B = 0$ when

$$\frac{X_{\text{amp},1}}{X_{\text{amp},0}} = \frac{m_0}{m_1}. \tag{4.21}$$

In practice, the values for m_i are related but not equal to the physical mass of the axes and $c_0 \neq c_1$ because of the mirror's larger surface area and the effect of the reaction axis counterweight. In addition, the MTM has a finite size and vibrations have finite wavelengths, meaning the level of vibration canceling will vary across the MTM. Despite these complications, it is still possible to find a ratio $X_{\text{amp},1}/X_{\text{amp},0}$ which minimizes the vibrations at locations of interest. For example, figure 4.11 shows the level of vibrations measured along the axis of motion with accelerometers under

Grid property	Value
Wire material	Tungsten
Wire plating	Copper (5 μm)
Wire diameter	50 μm
Wire spacing	160 μm
Grid diameter	62 cm

Table 4.2: Properties of the CLASS wire grids

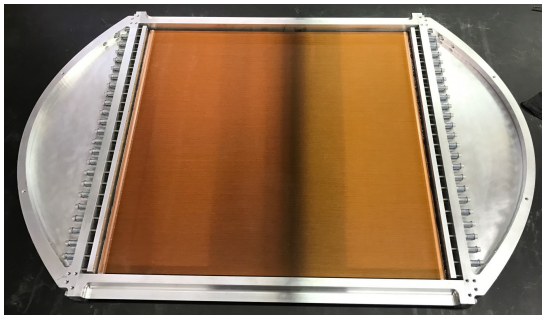

Figure 4.12: The VPM grid for the first W-Band CLASS telescope

either the mirror or reaction axis voice coils for a range of $X_{\mathrm{amp},1} / X_{\mathrm{amp},0}$ values. These measurements were performed on the Q-Band MTM before the wire grid was installed. The clear minimum and simultaneous phase shift distinctly show the optimal ratio to cancel vibrations at each location. These measurements were completed before and after the installation of the wire grid as well as once the VPM was installed in the telescope structure. Reoptimization is critical after installation because the cage mounts are much sturdier than those used during MTM development and testing.

After the Q-band VPM was installed on the telescope mount, accelerometers and the mount encoders were used to improve the reaction canceling within the complete telescope system. The residual vibrations from the VPM in the telescope structure are well below other vibrational lines in the system.

4.3 Wire Grids

A stationary linearly polarizing wire grid is held ~ 1 mm in front of the moving mirror and is used to separate the two orthogonal linear polarization states of the incoming radiation. Real wire grids have several non-ideal effects which can be mitigated though optimization of the materials and specifications of their design. Chuss et

al. (2012) developed a transmission-line optical model of VPMs at submillimeter wavelengths and showed that a ratio of π between the wire pitch (g) and wire diameter ($2a$) is a reasonable choice for producing grids with high isolation between orthogonal linear polarizations but that small variations around this ratio did not have a significant impact on the isolation. In addition, the ratios of g/λ and a/λ should be made as small as possible, and the outer material of the wires should be as conductive as possible in order to minimize loss and thermal emission from the wires.

CLASS chose to use copper plated wires because measurements in Chuss et al. (2012) indicated a gold wire plating might not function optically as gold. Copper plating will develop a copper oxide layer, but it will be extremely subwavelength. Also the copper plating can be made several times thicker than the skin depth at 40 GHz. Tungsten is used as the bulk material for the wires because it has the highest yield strength to density ratio of standard materials that can be drawn of formed into small caliber wire. The diameter of the CLASS wires was chosen based on how the wires would be secured to the grid frame. Stycast® 2850 with 23LV catalyst was used to epoxy the wires onto the grid mandrel bars. Pull tests with a variety of diameters indicated that the 50 μm wire would be secured by the epoxy up to its breaking strength of $\sim$ 7 N while 38 μm wire would pull out of the epoxy before it broke. Wires smaller than 50 μm could be used with other techniques to secure them, such as those used for the PIPER grids (Chuss et al., 2014); however, 50 μm is sufficiently subwavelength for the CLASS VPMs to allow this simpler method of wire attachment.

The wire grids for the VPMs for the four CLASS telescopes were manufactured

using a wire wrapping technique first pioneered in the far-infrared (Novak et al., 1989) and later scaled to larger format (Voellmer et al., 2008). The details of the CLASS grid wrapping technique are similar to those used for the PIPER grids (Chuss et al., 2014). In this process, the wires are wrapped onto a 8-inch diameter mandrel. Two aluminum bars are counter-sunk into the mandrel and grooved at the desired wire spacing using a square straight flute carbide end mill held at 45° relative to the mandrel. Wires are wrapped using a CNC mill with a 4th (rotation) axis mounted to the machine bed. After wrapping is complete, the wire is epoxied to the mandrel bars. The wire between the mandrel bars is cut, and the wires are carefully unwrapped and mounted to a frame using 100 screws and springs. The screws are tightened a set amount such as to apply 50% of the breaking strength to each wire. This requires over 3000 lbs of force across the bars holding the wires. The applied tension raises the resonance frequency of the wires to over an order of magnitude above the modulation frequency. After over a year of operation at the CLASS site, all of the wires comprising the Q-band wire grid were still intact. Figure 4.12 shows the complete grid for the first W-band VPM.

Figure 4.13 shows a microscope image taken using a microscope mounted on a custom XY-gantry system described in section 4.4. Fifty of these images were taken across the vertical height of the grid ($\sim$ 1 per 0.5 in) with the microscope centered horizontally. These images were used to measure the ratio of the wire diameter to wire spacing. For the W1 grid the pitch to diameter ratio is 3.01 ± 0.06, which is within 5% of the target spacing of π and a histogram of the measured values is shown in the right plot of figure 4.13. A similar procedure was done for the Q-band wire grid which has a pitch to diameter ratio of 2.61 ± 0.12, which is 17% away from the

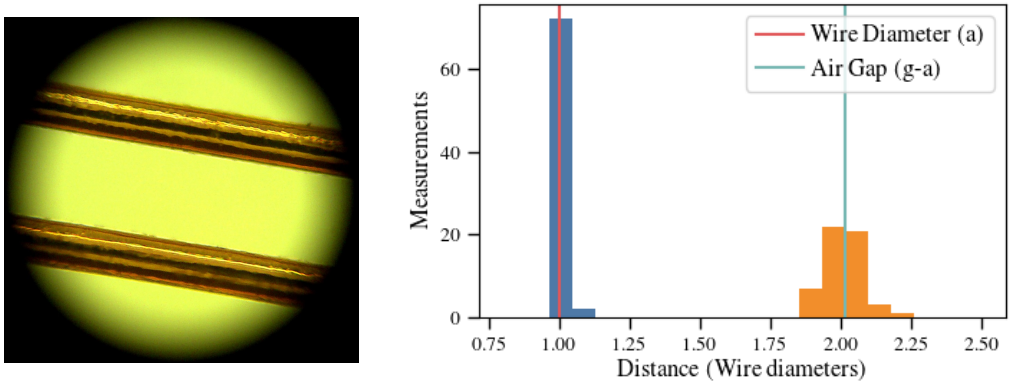

Figure 4.13: (Left) A microscope image of the wires taken using the XY-gantry calibration microscope, used to measure the wire spacing across the grid and to align the grid plane to the mirror. (Right) The wire spacing measurements for the W-band wire grid. Fifty images of the wires were taken across the face of the grid. The diameters of the wires in those images were used to calibrate the spacing between the wires and determine the pitch of the grid.

target spacing but still within the acceptable range for the CLASS grids.

4.4 Grid-Mirror Alignment

The wire grids need to be held flat and parallel to the VPM mirror in order to reduce temperature to polarization leakage and maintain the polarization transfer function as close to ideal as possible. In addition, the absolute position of the wire grid with respect to the mirror-off position[9] has to be within 2 mm (Q-band) or 0.2 mm (W-band) of the desired throw center. This requirement is determined by the stiffness of the MTM flexure, the weight of the mirror, and the force available from the voice coils.

To complete this alignment, a custom XY-gantry calibration microscope was designed and built because no commercial XY-gantry could meet the requirements of travel and clearance across the grid face. The left image in figure 4.14 shows the

[9]The mirror-off position or the zero current position is defined as the position the MTM sags to when the telescope is pointed at 45° elevation and the voice coils are unpowered.

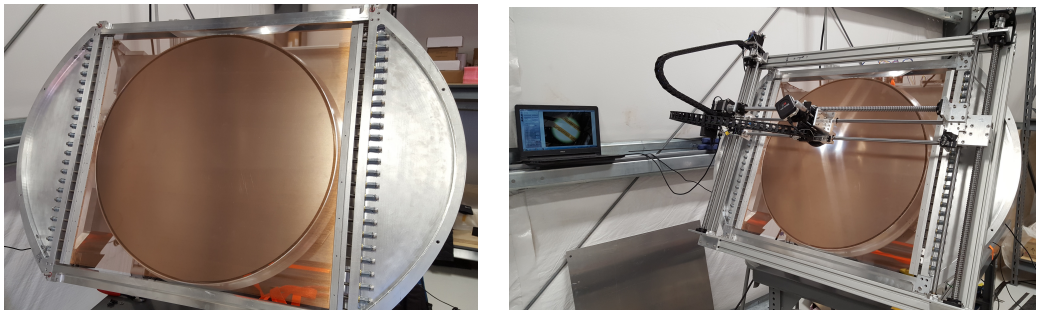

Figure 4.14: Left: The completed W-band VPM in the highbay at the CLASS site. Right: The XY-gantry calibration microscope in used on the W-band VPM.

XY-gantry in use with the W1 VPM. Three 750 mm long 16 mm diameter ball screws, two on the vertical axis and one on the horizontal axis, are coupled to NEMA 23 stepper motors. The ball screws and four 12 mm diameter linear shafts support the microscope stage which has 546 mm by 570 mm of travel. The microscope stage contains a microscope connected to a vertically mounted linear micrometer stage with 25 mm of travel. The microscope has a 10x objective and 20x wide-field eyepiece for 200x total magnification and is coupled to a 2 megapixel USB camera through a macro lens. The image of the wires in figure 4.13 is an example of the view of the wires through the microscope, which has a $\sim$ 250 μm diameter field of view. The microscope is focused on the wires or the mirror using the micrometer stage on the gantry. The depth of focus is $\sim$ 10 μm, which is small enough to allow the user to distinguish between the top and edge of each wire. The positioning of the microscope stage is controlled with an Arduino Uno[10] connected to a SMAKN® stepper motor driver. In use, the microscope stage can be repeatably stepped the $\sim$ 160 μm between wires, and reliably returns within $\sim$ 50 μm to previous positions after removing the gantry from the VPM and reinstalling.

[10] https://www.arduino.cc/

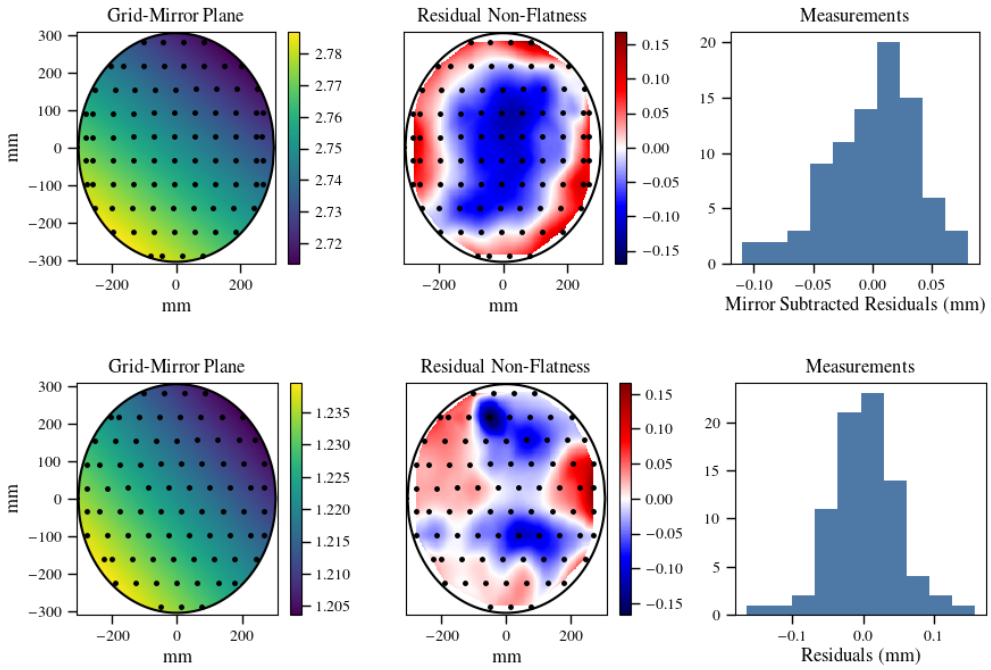

Figure 4.15: The final alignment of the grid to the mirror for the Q-band (top) and W-band (bottom) VPMs. The left figures show the plane of the grid relative to the mirror at the mirror-off position and the black dots indicate the measurement points. The center plots show the residuals from the plane fit and, for the Q-band, primarily shows the shape of the mirror described in section 4.2.2. The colorbar scales of the left and center plots are all in millimeters. The right plots show the histograms of the residuals to the plane fit, the Q-band residuals have also had the CMM measured mirror shape was subtracted.

To align the wire grid to the mirror, the distance between the wires and the mirror is measured at $\sim$ 60 points across the mirror face by measuring the distance the vertical linear stage must be adjusted to change the focus between the wires and the mirror. This distance is recorded with the XY-gantry position and the three mirror encoder positions to determine the plane of the wire grid with respect to the mirror plane at the mirror-off position. The parallelism and positioning of the wire grid is coarsely adjusted with spacers under the kinematic grid mounts and then finely adjusted with micrometers attached to a flattening ring that is gently pressed into the wires to define a wire plane. An initial alignment was performed at JHU and the final alignments were performed at the CLASS high-altitude site before the VPMs were installed in the telescope optics cage.

The top row in figure 4.15 shows the final alignment for the Q-band VPM. The top left plot shows a plane fit to the grid-mirror distance measurements across the face of the mirror. The center plot shows the residuals to that fit. The shape in the residual non-flatness is due to the shape of the Q VPM mirror described in section 4.2.2. The tilt across the mirror is 24.9 arcseconds, which is 1.5 wire diameters and well within the tolerances required for the 90 arcminute Q-band beam. The residuals from the measurement, after the CMM measured mirror shape is subtracted, indicates the wire grid has an RMS flatness error of 36 μm with the flattening ring engaged, which is less than the diameter of a wire.

The bottom row in figure 4.15 shows the final alignment for the first W-band VPM. The top left plot shows a plane fit to the grid-mirror distance measurements across the face of the mirror. The center plot shows the residuals to that fit. The tilt across the mirror is 12.2 arcseconds, which is half the diameter of a wire and well within

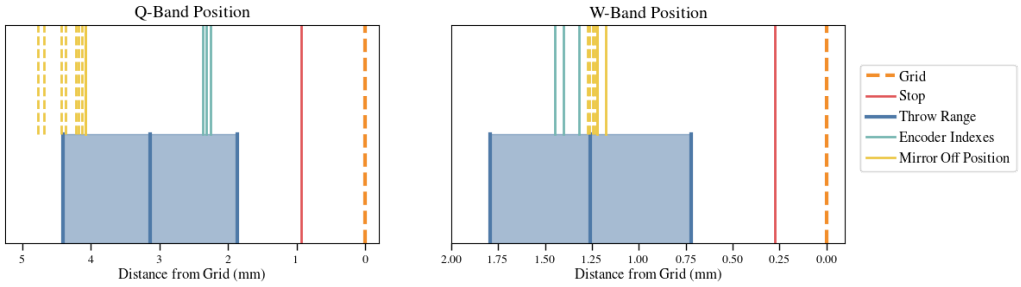

Figure 4.16: The absolute position of the Q- and W-band VPM mirrors with respect to the wire grid after alignment. The mirror-off positions (plotted for each boresight value) are within the required range for each VPM and the encoder index locations are within the mirror throw. The red line marks the location of a hard mirror stop that is a protection of last resort for the VPM grid.

the tolerances required for the 40 arcminute W-band beam. The residuals from the measurement indicate the wire grid has an RMS flatness error of 49 μm when the flattening ring is engaged, which is about the diameter of one wire.

In addition to the parallelism requirements, the absolute position of the wire grid with respect to the mirror-off position and the encoder indexes needed to be set. This requirement was much more stringent for the W-Band VPM as the stiffer flexure made the total possible displacement of the mirror much smaller. Figure 4.16 shows the achieved Q-band and W-band positions. The red lines indicate the position of the hard stop for the VPMs, where a metal block is positioned to prevent farther travel. The distances between the mirror-off positions and the required mirror throw are within the range accessible to each VPM, and the encoder indexes are within the mirror throw, enabling position recalibration during observation.

4.5 VPM Performance

The tilt of the VPM mirrors is measured using three optical linear encoders mounted on the back of the mirror. The change in tilt across the throw of the VPM creates a

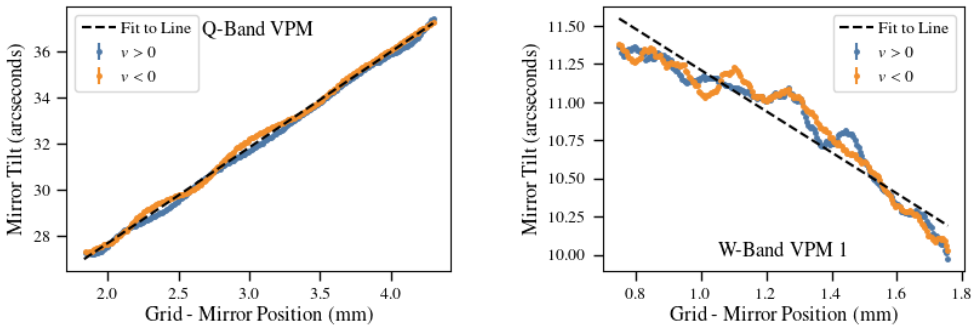

Figure 4.17: The tilt or parallelism error between the mirror and grid plane as the VPM is running at 10 Hz at an elevation = 45° and boresight = 0° for the Q-band (left) and W-band (right) VPMs. The absolute value of these tilts are determined with the grid-mirror alignment and then relative tilts are calculated from each set of encoder positions during the test.

temperature to polarization leakage in single detector data. While various analysis methods, such as template subtraction, can be used to measure and remove these signals, the design goal of the MTM was to reduce their amplitude as much as possible.

Figure 4.17 shows the amplitude of the mirror tilt as a function of grid mirror distance while the VPMs were running at 10 Hz for the Q-Band (left) and W-Band (right) VPMs. Both measurements were taken with the VPM held in the configuration consistent with the CLASS telescope observing at 45° elevation and at zero boresight. The absolute value of the tilt was calibrated using the grid-mirror alignment, described in section 4.4, which results in a parallelism measurement relative to a plane defined by a set of three encoder values. The tilts are then calculated for each set of encoder values as the VPM runs. Fitting the tilts to lines gives a changing tilt of 4.16 arcsec/mm and -1.35 arcsec/mm for the Q-band and W-band respectively; however, it is clear that a linear fit is not a complete explanation. The overall reduction in the tilt slope between the Q-band and W-band is likely due to the increased stiffness

in the MTM flexure.

Both the Q-band and W-Band tilts exhibit a hysteresis effect from the direction of motion of the mirror. The effect is ± 0.3 arcseconds for Q-band and ± 0.15 arcseconds for W-band. This is most likely due to the air resistance on the mirror motion because it depends on velocity and the maximum velocity for Q-band is twice that of W-band. The air resistance could produce a changing force vector on the mirror supports that could cause a slight tilt. It is possible the other non-linear aspects of the tilts come from process variation in the assembly of the CLRFs or small machining errors in the linkages of the full flexure.

The range of the Q-band tilt is 10.25 arcseconds which indicates a level of $T \rightarrow P \sim 3 \times 10^{-5}$ for single detector data. The tilt of the W-band mirror over the mirror throw, 1.4 arcseconds, implies $T \rightarrow P \sim 3 \times 10^{-6}$. With forward modeling or pair subtraction, the $T \rightarrow P$ due to tilts can be further reduced. In addition, the front-end modulation of the CLASS data with the VPM means $T \rightarrow P$ effects at or before the VPM, such as with these tilts, are some of the few sources of instrument polarization that can affect CLASS data.

The Q-Band VPM was installed at the CLASS site in the Spring of 2016. As described in section 4.2.3, the lower than ideal resonance frequency of the Q-band MTM allows the wind and motion of the telescope to excite vibrations in the mirror. These vibrations do not decrease the quality of data obtained by the experiment because the exact mirror positions are read out fast enough to observe the vibrations and these positions are used in the demodulation of the CLASS data. The vibrations do inhibit the function of the VPM in high winds ($\geq$ 12 m/s) because the mirror will hit the software limit and the MTM control will turn off to protect the wire grid. To

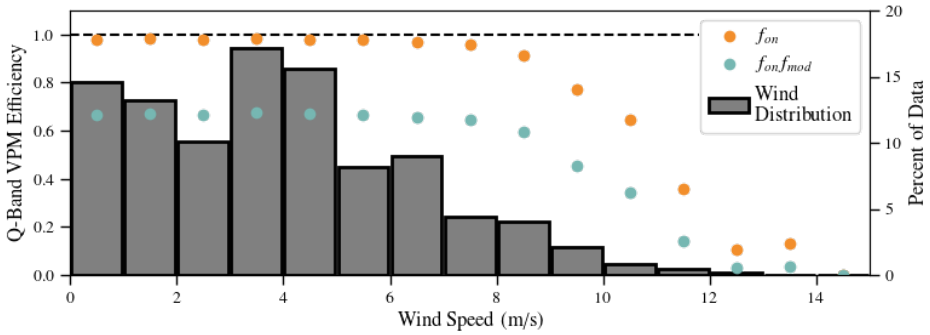

Figure 4.18: The VPM on efficiency and the VPM modulation efficiency as a function of wind speed for the Q-band VPM between September 1st 2016 and February 1st 2018. The bars denote the distribution of the winds experienced at the CLASS site during this time. The low resonance frequency of the Q-band MTM limits the VPM functionality in high winds, but the overall on efficiency is still over 96%.

mitigate this effect, the total throw of the VPM was reduced slightly to allow for more vibrations. This reduced the overall modulation efficiency but significantly increased the uptime of the VPM.

Figure 4.18 shows the effect of the wind on the uptime of the Q-band VPM at the CLASS site between September 1st 2016 and February 1st 2018. During this time period the VPM was on for over 288 days and completed over 250 million cycles. This accounts for over 96% of the time the Q-band telescope spent observing the CMB. The VPM modulation efficiency, defined in equation 4.4, during this period was 0.675 which is lower than the ideal value but was required to maximize the efficiency of the survey.

4.6 Conclusions

The VPMs for the CLASS telescopes were designed to meet a variety of constraints that were required to achieve the science goals of the CLASS survey. The CLASS VPMs required a 60 cm clear aperture with a mirror throw of up to 2.5 mm at 10 Hz

while maintaining excellent parallelism with between the mirror and the wire grid. The flexure-based mirror transport mechanism for the Q-band and first W-band VPMs achieve these requirements; however, design optimization was required between the Q- and W-band MTMs. The VPMs for the second W-band and the high frequency CLASS telescopes have the same design as the first W-band VPM.

The four wire-grids for the CLASS VPMs have been fabricated, and the specifications for the first two to be used are reported here. These large aperture wire grids have unprecedented uniformity and flatness across the entire VPM aperture and the manufacturing technique employed here is scalable to even larger apertures.

Chapter 5

Modeling a VPM

Chapter 4 described the most ideal case for modulation with a VPM, where reflections off the wire grid and mirror are idea (ie. $r = -1$) and the detectors are exactly aligned at $\pm 45^\circ$ with respect to the wire grid. In this chapter, I will be expanding the modeling to include a more complete description of the VPM. This will include the necessary transforms for calculating the modulation functions across the focal plane, the effects of realistic materials for the wires and mirror, and the effect of the detector readout system on VPM signatures.

5.1 Ideal VPM Model

Understanding how the polarization modulation varies across the focal plane for the CLASS telescopes is necessary to obtain the correct polarization state on the sky. In this section, I derive the modulation functions for the CLASS detectors as a function of their pointing on the sky and introduce mathematical descriptions of a VPM which can be easily extended to more complex representations.

Figure 5.1 shows the setup used for the VPM coordinate system, the wires, $\hat{w}$, a vector perpendicular to the wires, $\hat{a}$, and the normal to the wire grid, $\hat{n}$, are aligned

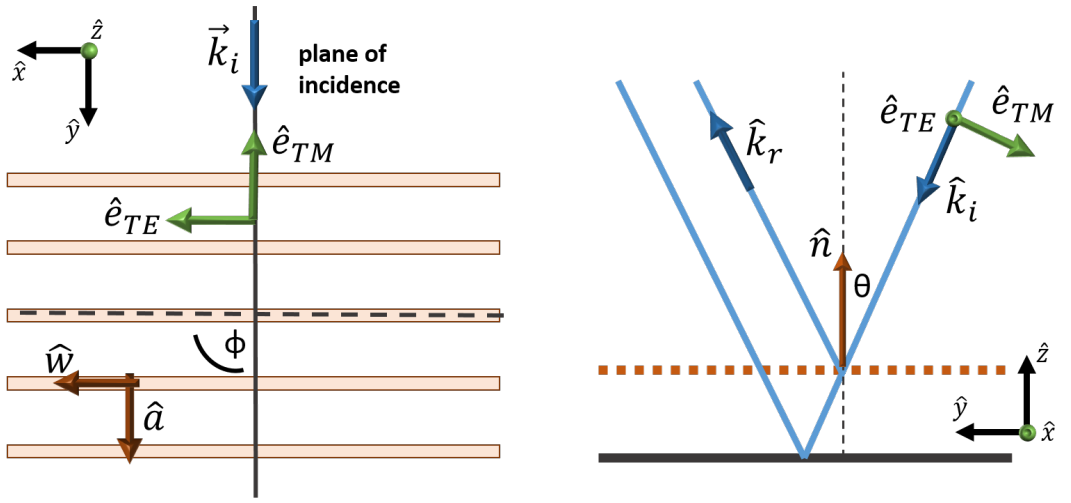

Figure 5.1: The layout of the coordinate system for a VPM such as those used in the CLASS telescopes. A right-handed coordinate system is defined by the normal to the grid surface, $\hat{n}$, a vector along the wires, $\hat{w}$, and a third vector $\hat{a}$ that is perpendicular the wires. A second set of orthogonal vectors are defined by the incident wavevector, $\hat{k}_i$, and unit vectors for electric fields in TE (transverse electric) and TM (transverse magnetic) modes with respect to the surface of the VPM.

along $\hat{x}$, $\hat{y}$, and $\hat{z}$, respectively. The incident wavevector, $\hat{k}_i$, the reflected wavevector $\hat{k}_r$, and the surface normal, $\hat{n}$, all define a *plane of incidence* where ϕ is the angle between $\hat{w}$ and the plane of incidence and θ is the angle of incidence for $\hat{k}_i$. This coordinate system, and the others that will be introduced later, are listed in table 5.1.

The most straightforward way to trace polarization through a system such as the VPM is with a Jones matrix (more details in Appendix A) because the Jones matrix encodes relative phase differences between two orthogonal polarization states and is the standard way to describe interactions with surfaces or materials. A major drawback to the Jones matrix formalism is that these 2×2 matrices do not have a mechanism of describing coordinate system shifts, such as those that occur on reflections, in a way that can be differentiated from phase shifts or retardance of the

Coordinate System Definitions	
VPM	A coordinate system used to define the VPM setup. The surface normal is $\hat{n} = [0, 0, 1]$ and the wires are along $\hat{w} = [1, 0, 0]$
Instrument	A coordinate system for when imaginary detector at the center of the CLASS telescope pointing is aligned along the horizon at boresight zero. The azimuth and elevation offsets (az, el) for each detector in the CLASS telescope are defined relative to this coordinate system.
Sky	(Detector at Horizon) A coordinate system for an individual detector where it is pointed along the horizon. The on-sky "detector angle" is defined in this coordinate system because of standard conventions. The VPM transfer functions are calculated in terms of these coordinates because standard mapping code works with the detector sensitivity to Stokes parameters defined in this coordinate system.
Mod	A remapping of the sky coordinate system to after reflection through the VPM, deals with those respective sign changes. Because of our modulation, our detectors actually observe in this coordinate system.
Global	A transition coordinate system, O matrices go from one of the local coordinate systems to this one and O^T matrices go from here to the other local coordinate systems.

Table 5.1: A description of the different coordinate systems used to describe or define different variables within the CLASS optical setup

light. For example, the "standard" Jones Matrix for a mirror,

$$J_{mirror} = \begin{bmatrix} -1 & 0 \\ 0 & 1 \end{bmatrix}, \tag{5.1}$$

includes the two $e^{i\pi}$ phase shifts that occur on a reflection off a perfect surface and an extra -1 for the TM mode to represent a change in direction of the wavevector. However, that Jones matrix could also represent a transmissive optical element where one axis is retarded relative to the other. Working with Jones matrices in three-dimensional systems inherently requires addition tracking of wavevectors and the local coordinate systems at each interactive surface.

In order to make this process slightly more straightforeward, I am using a formalism similar to that developed in Yun et al. (2011a) and Yun et al. (2011b), where three dimensional wavevectors and electric field vectors ($\hat{k}$, $\hat{E}$) are traced through an optical system using orthogonal O matrices to transform these vectors into the local coordinate system at each surface. Orthogonal matrices require three orthogonal unit vectors as the columns, and for a plane wave interacting with a surface there is a natural set of basis vectors: the normalized wavevector, and unit vectors describing the direction of the transverse electric (TE, also s-wave polarization) and transverse magnetic (TM, also p-wave polarization) modes of the electric field as it is incident on that surface.

$$O = \begin{bmatrix} \hat{e}_{TE}^T & \hat{e}_{TM}^T & \hat{k}^T \end{bmatrix} \tag{5.2}$$

These basis vectors can always be explicitly defined with respect to the wavevector and surface normal. Since the O matrices will encode all the coordinate system shifts on reflection, the Jones matrices will always be written assuming a TE, TM basis for the orthogonal polarization states. In this setup, the Jones matrices will be extended

to 3D as

$$J_{3D} = \begin{bmatrix} & & 0 \\ & J_{2D} & 0 \\ 0 & 0 & 1 \end{bmatrix}. \tag{5.3}$$

This is possible because any valid electric field cannot be projected into the third column and the reflection of wavevectors is handled with the O matrices. In this setup, the Jones matrix for a mirror is now

$$J_{mirror} = \begin{bmatrix} -1 & 0 & 0 \\ 0 & -1 & 0 \\ 0 & 0 & 1 \end{bmatrix}, \tag{5.4}$$

and the O matrices will account for the change in direction of the TM mode. These O matrices are also the mechanism for defining and rotating the polarization basis of one coordinate system into another.

As an example, for a wavevector reflecting out of the VPM and headed toward the sky at some angle of incidence θ, and where the plane of incidence is perpendicular to the wires, $\hat{k}_r = [0, \sin\theta, \cos\theta]$[1]. The basis vectors for the electric field are then

$$\begin{aligned} \hat{e}_{TE} = \hat{s} &= \frac{\hat{k}_r \times \hat{n}}{|\hat{k}_r \times \hat{n}|} = [1, 0, 0] \\ \hat{e}_{TM} = \hat{p} &= \frac{\hat{k}_r \times \hat{e}_{TE}}{|\hat{k}_r \times \hat{e}_{TE}|} = [0, \cos\theta, -\sin\theta]. \end{aligned} \tag{5.5}$$

Note that these unit vectors are defined in such a way that they can be quickly and easily calculated for any wavevector and surface normal, an especially useful feature when the wavevectors become more complicated. The corresponding O matrix for

[1] I am starting with the outgoing wavevector because electromagnetic waves are invariant under time reversal and most detector parameters, such as pointing offsets and polarization angles, are defined or calibrated based on the sky.

this reflecting wavevector is

$$O_r = \begin{bmatrix} 1 & 0 & 0 \\ 0 & \cos\theta & \sin\theta \\ 0 & -\sin\theta & \cos\theta \end{bmatrix}. \tag{5.6}$$

Given an outgoing wavevector and a surface normal, the incident wavevector is

$$\hat{k}_i = \hat{k}_r - 2(\hat{k}_r \cdot \hat{n})\hat{n} \tag{5.7}$$

and the electric field basis vectors are calculated as with equation 5.5 to create another O matrix,

$$O_i = \begin{bmatrix} 1 & 0 & 0 \\ 0 & -\cos\theta & \sin\theta \\ 0 & -\sin\theta & -\cos\theta \end{bmatrix}. \tag{5.8}$$

These O matrices function such that, for any valid electric field unit vector $\hat{E}_r$, where $\hat{k}_r \cdot \hat{E}_r = 0$, $O_r^T \hat{E}_r$ transforms the electric field into the TE, TM basis of the surface. Reflection or transmission coefficients for surfaces are defined in this basis, often just using the Fresnel equations (see appendix B for more details). For a perfectly ideal case, when the plane of incidence is perpendicular to the wires, the three dimensional Jones matrix for the VPM is

$$J_{VPM} = \begin{bmatrix} -1 & 0 & 0 \\ 0 & -e^{i\delta} & 0 \\ 0 & 0 & 1 \end{bmatrix} \quad \text{with} \quad \delta = \frac{4\pi\nu}{c} z\cos\theta. \tag{5.9}$$

δ is the induced phase delay caused by the polarization perpendicular to the wires transmitting through the grid and reflecting off the mirror that is z behind the grid.[2]

Using this setup, the incident electric field is calculated with respect to the reflected

[2]The more complete VPM Jones matrix, defined in 5.14, includes a dependency on the angle of the plane of incidence with respect to the wires. In this example $\phi = 90^\circ$ and so 5.14 is evaluated at this angle.

field by

$$\hat{E}_i = \left(O_i \cdot J_{VPM} \cdot O_r^T \right) \hat{E}_r \tag{5.10}$$

and we can also note that $O_i O_r^T$ encodes all the coordinate shifts related to reflection off the surface separately from the reflection coefficients or relative phase shifts. In this example

$$O_i O_r^T = \begin{bmatrix} 1 & 0 & 0 \\ 0 & -\cos 2\theta & \sin 2\theta \\ 0 & -\sin 2\theta & -\cos 2\theta \end{bmatrix}, \tag{5.11}$$

which clearly illustrates the reflection and rotation by 2θ that occur on reflection at non-normal incidence. When $\phi \neq 90^\circ$, the unit vectors for reflection off the VPM are rotated as

$$k_r = \begin{bmatrix} \sin\theta\cos\phi \\ \sin\theta\sin\phi \\ \cos\theta \end{bmatrix} \quad \hat{e}_{TE} = \begin{bmatrix} \sin\phi \\ -\cos\phi \\ 0 \end{bmatrix} \quad \hat{e}_{TM} = \begin{bmatrix} \cos\theta\cos\phi \\ \cos\theta\sin\phi \\ -\sin\theta \end{bmatrix} \tag{5.12}$$

and the corresponding incident unit vectors are

$$k_i = \begin{bmatrix} \sin\theta\cos\phi \\ \sin\theta\sin\phi \\ -\cos\theta \end{bmatrix} \quad \hat{e}_{TE} = \begin{bmatrix} \sin\phi \\ -\cos\phi \\ 0 \end{bmatrix} \quad \hat{e}_{TM} = \begin{bmatrix} -\cos\theta\cos\phi \\ -\cos\theta\sin\phi \\ -\sin\theta \end{bmatrix}. \tag{5.13}$$

To get the Jones matrix in this case is slightly more complicated, because there is a total of four reflection coefficients based on the combination of TE and TM modes, both along and across the wires. To calculate this, we take the electric fields in the TE and TM basis and project them onto the grid plane ($\hat{e}' = \hat{e} - (\hat{e} \cdot \hat{n})\hat{n}$). These prime vectors are projected into the ($\hat{w}$, $\hat{a}$) coordinates where the associated reflection coefficients are applied. Rotating back into the (TE, TM) basis completes the Jones

matrix. Mathematically, this looks like

$$J_{VPM} = \begin{bmatrix} \sin\phi & -\cos\phi & 0 \\ \cos\phi & \sin\phi & 0 \\ 0 & 0 & 1 \end{bmatrix} \begin{bmatrix} \Gamma_{TE,w}\sin\phi & \Gamma_{TM,w}\cos\phi & 0 \\ -\Gamma_{TE,a}\cos\phi & \Gamma_{TM,a}\sin\phi & 0 \\ 0 & 0 & 1 \end{bmatrix}$$
$$J_{VPM} = \begin{bmatrix} \Gamma_{TE,w}\sin^2\phi + \Gamma_{TE,a}\cos^2\phi & (\Gamma_{TM,w} - \Gamma_{TM,a})\cos\phi\sin\phi & 0 \\ (\Gamma_{TE,w} - \Gamma_{TE,a})\cos\phi\sin\phi & \Gamma_{TM,w}\cos^2\phi + \Gamma_{TM,a}\sin^2\phi & 0 \\ 0 & 0 & 1 \end{bmatrix}. \tag{5.14}$$

When reflections off the grid and the mirror are ideal, $\Gamma_{TE,w} = \Gamma_{TM,w} = -1$ and $\Gamma_{TE,a} = \Gamma_{TM,a} = -e^{i\delta}$.

$$J_{VPM} = \begin{bmatrix} -\sin^2\phi - e^{i\delta}\cos^2\phi & (e^{i\delta} - 1)\cos\phi\sin\phi & 0 \\ (e^{i\delta} - 1)\cos\phi\sin\phi & -\cos^2\phi - e^{i\delta}\sin^2\phi & 0 \\ 0 & 0 & 1 \end{bmatrix}. \tag{5.15}$$

Equation 5.14 and the O matrices built with equations 5.12 and 5.13 create a standard mechanism for calculating how the VPM affects any electric field traveling along wavevectors defined in spherical coordinates with respect to the VPM. The next step is to determine the wavevectors and electric fields[3] of the CLASS detectors.

The optical designs of the CLASS telescopes have an imaginary pixel at the center of the focal plane with incidence on the VPM at $\theta = 20^\circ$ and $\phi = 90^\circ$. The VPM is located at a pupil for the optical system, meaning the illumination of the VPM by each detector is approximately the same (all detectors "see" the same VPM). The left plot in figure 5.2 shows the distribution of pixels across the CLASS Q-band focal plane. Each detector has an azimuth and elevation pointing offset that is measured by observations of the moon[4] and has coordinates (az, el). Since relative detector

[3] An "electric field" for a detector is a unit vector projected on the sky that encodes the polarization sensitivity of that detector.

[4] The moon is a point source for the Q-band telescope, the higher frequency telescopes with smaller beamwidths will use other point sources to calibrate detector pointing.

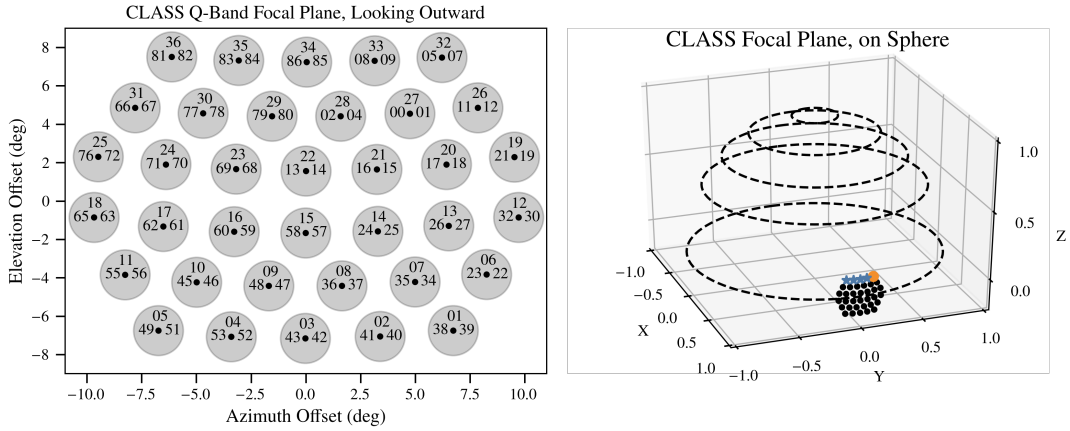

Figure 5.2: (Left) The pixel distribution on the CLASS Q-band focal plane. Each gray circle indicates a dual polarization pixel (but does not indicate the beamwidth of the pixel). In each pixel, the top number is the designed feedhorn number, the left is the detector id number for the detector with angle $\alpha = -45^\circ$, and the right number is the detector id for the $\alpha = 45^\circ$ polarization. This plot is oriented as though the receiver is looking out at the sky. (Right) The Q-band focal plane positions placed on a sphere where the receiver is pointed along $[1, 0, 0]$. The blue stars indicate the top row of detectors in the focal plane while the orange dot is the feedhorn number 36, which is in the top left corner when the receiver is looking outward.

pointings are calibrated off other measurements and well understood, we can define all the detector incidences on the VPM in terms of the a "main beam" pointing $(\Theta, \Phi) \sim (20^\circ, 90^\circ)$ and the relative (az, el) coordinates. The optical alignment of the telescope system is not 100% accurate and we expect there to be some offset to the ideal positioning, so Θ and Φ will need to be calibrated.

The "instrument" coordinate system for the CLASS telescopes is defined as the coordinate system where the main beam is pointed along the horizon with boresight equal to zero. This is different than the detector coordinate system, which is when *that individual* detector is pointed along the horizon. Conventional mapping routines use the detector coordinate system to define the "detector angle," the angle the detector polarization makes with respect to meridians on the sky. However, the exact definition depends on the convention used. Figure 5.3 shows three relevant

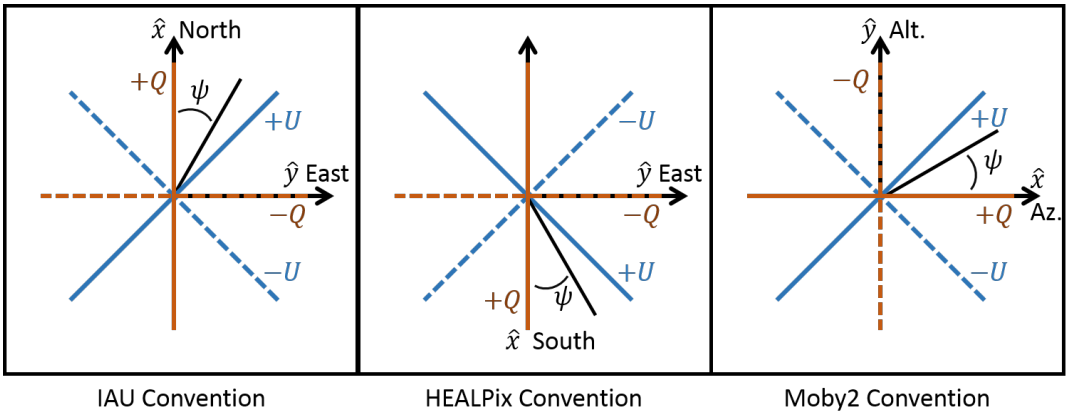

Figure 5.3: Some of the different conventions used to define the direction of polarization on the sky. The IAU convention is the most standard one used by astronomers. The HEALPix convention is often called the CMB convention because HEALPix is the standard software system used to pixelize the full sky and all CMB maps use this pixelization. Moby2 is the software system used by the CLASS team for analysis, where parallactic angles are calculated with the time and mount position assuming this polarization convention.

conventions for defining polarization angle when the detector is pointed along the horizon; the HEALPix convention is often called the CMB convention because the HEALPix software is what defines the standard pixelization for CMB maps and the Moby2 convention is what is used in the analysis software currently used by the CLASS team. Because I am calculating transfer functions that will go into the CLASS analysis pipeline, I will use the Moby2 convention, where the basis vectors for the electric fields on the sky are $\hat{x}_{\rm det} = [0, -1, 0]$ and $\hat{y}_{\rm det} = [0, 0, 1]$[5]. The detector angle, α is defined such that the electric field of the detector is

$$\hat{E}_{\rm det} = \hat{x}_{\rm det} \cos\alpha + \hat{y}_{\rm det} \sin\alpha \tag{5.16}$$

To rotate a detector wavevector and electric field from along the horizon into its

[5]Changing the convention used just requires updating the definitions of these basis vectors and will simply result in sign changes for the output modulation functions.

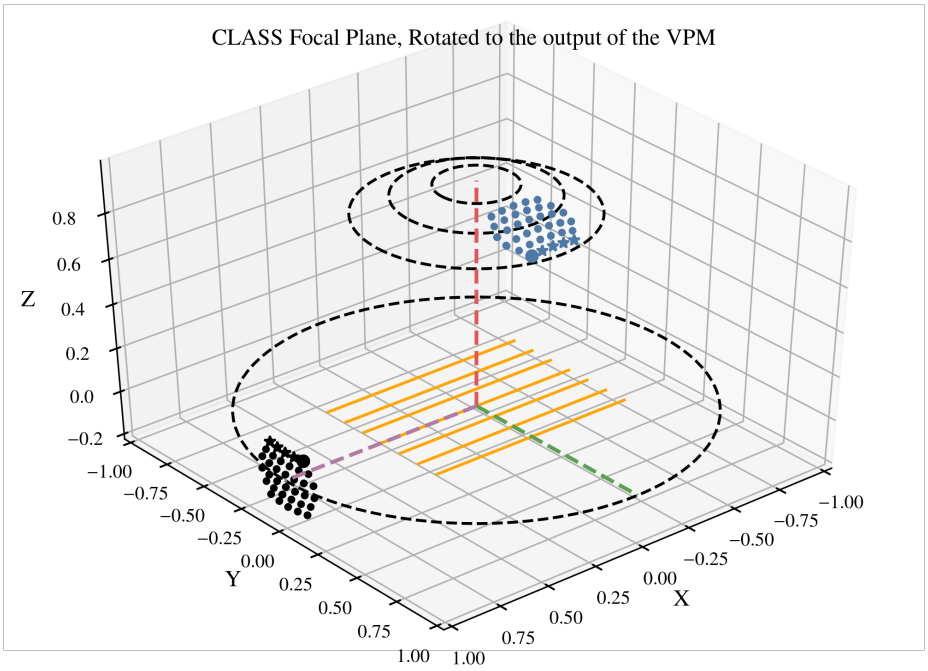

Figure 5.4: A visual representation of the rotations required to determine the detector incidence on the VPM. The black focal plane is the focal plane in the instrument coordinate system when the main beam is pointed along $[1, 0, 0]$, the stars are the detectors with the most positive elevation offsets and the larger dot in the corner is feedhorn 36 which is the top left corner when looking outward from the receiver. The orange lines represent the wires in the VPM coordinate system and the blue focal plane is the detector wavevectors with respect to the VPM. The marker shapes for the blue focal plane is the same as the black and indicate the detectors with the highest elevation offsets also have the largest angle of incidence on the VPM.

position on the focal plane we use

$$R_{\text{det}\to\text{inst}} = \begin{bmatrix} \cos(el)\cos(az) & \cos(el)\sin(az) & -\sin(el) \\ -\sin(az) & \cos(az) & 0 \\ \sin(el)\cos(az) & \sin(el)\sin(az) & \cos(el) \end{bmatrix}. \tag{5.17}$$

From the instrument coordinate system, we can rotate into the orientation of the VPM for the CLASS telescopes. This rotation is

$$R_{\text{inst}\to\text{VPM}} = \begin{bmatrix} \cos\Phi\sin\Theta & \sin\Phi & \cos\Phi\cos\Theta \\ \sin\Phi\sin\Theta & -\cos\Phi & \sin\Phi\cos\Theta \\ \cos\Theta & 0 & -\sin\Theta \end{bmatrix}. \tag{5.18}$$

These rotations depend on how the (az, el) variables are defined during pointing calibration measurements and orientation of the of the VPM within the CLASS optical setup.

Figure 5.4 shows a visual representation of these rotations. The black focal plane is the focal plane in the instrument coordinate system when the main beam is pointed along $[1, 0, 0]$; the stars are the detectors with the most positive elevation offsets and the larger dot in the corner is feedhorn 36, in the top left corner when looking outward from the receiver. The orange lines represent the location and direction of the wires in the VPM coordinate system and the blue focal plane is the detector wavevectors with respect to the VPM. The marker shapes for the blue focal plane is the same as the black and indicate the detectors with the highest elevation offsets also have the largest angle of incidence on the VPM. The azimuth and elevation pointing offsets for each detector create a spread in the angle of incidence and angle with respect to the grid wires. The spread in θ and ϕ are shown in figure 5.5 along with the absolute value of the angle of the detector electric field with respect to the wires in the grid.

Mathematically, the definitions of the sky basis vectors ($\hat{x}_{det}$, $\hat{y}_{det}$, and $\hat{k}_{det}$) and the

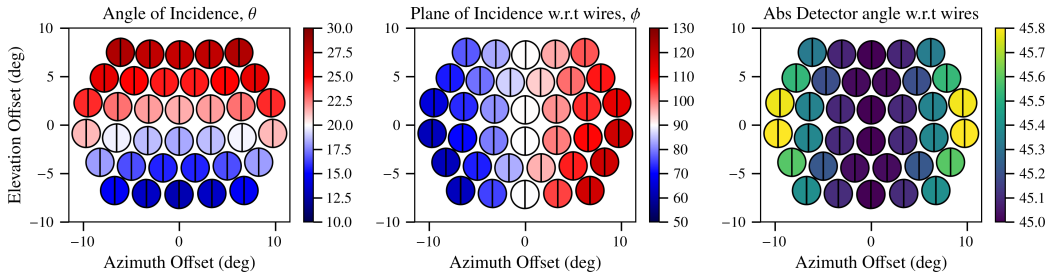

Figure 5.5: The projections of individual detectors in the Q-band focal plane onto the surface of the VPM. The left plot is the angle of incidence, calculated as $\cos^{-1} \hat{k}_r \cdot \hat{n}$. The main beam has an angle of incidence of 20°, but the large field of view of the instrument requires a significant of incidence angles on the VPM. The center plot is the angle of the plane of incidence with respect to the wires of the VPM grid, calculated as $\phi = \tan^{-1} \frac{\hat{k}_r \cdot \hat{a}}{\hat{k}_r \cdot \hat{w}}$. The main beam is designed to have $\phi = 90°$, but as with the angle of incidence, the large field of view requires a large range in this parameter. The right plot shows the absolute value of angle of the detector polarization with respect to wire grid. These are designed to be as close to 45° as possible, however edge effects do cause those detectors to have modulated polarization which is not quite orthogonal to each other.

rotations necessary to transform these basis vectors into position with respect to the VPM can be combined into one orthogonal matrix which is defined as

$$O_{sky} = R_{\text{inst}\to\text{VPM}} \cdot R_{\text{det}\to\text{inst}} \cdot \begin{bmatrix} 0 & 0 & 1 \\ -1 & 0 & 0 \\ 0 & 1 & 0 \end{bmatrix}. \tag{5.19}$$

Since we are interested in calculating the polarization modulation as a function of the Stokes vectors as they are defined on the sky, we need to trace the sky basis vectors through the reflections and coordinate transforms caused by the VPM. These transforms are a series of O matrices defined as

$$O_{mod} = O_i \cdot O_r^T \cdot O_{sky}. \tag{5.20}$$

Defining $\hat{E}_{det}$ as the electric field of the detector on the sky and $\hat{E}_{mod}$ as the detector electric field once it has been modulated by the VPM *but in the sky coordinate system* we can connect these two electric fields with a series of orthogonal transforms and

the Jones matrix for the VPM as

$$\begin{aligned}
\hat{E}_{mod} &= O_{mod}^T \left(O_i \cdot J_{vpm}(\theta, \phi, z, \nu) \cdot O_r^T \right) O_{sky} \hat{E}_{det} \\
&= O_{sky}^T \cdot O_r \cdot O_i^T \left(O_i \cdot J_{vpm}(\theta, \phi, z, \nu) \cdot O_r^T \right) O_{sky} \hat{E}_{det} \\
&= \left(O_{sky}^T \cdot O_r \right) J_{vpm}(\theta, \phi, z, \nu) \left(O_r^T \cdot O_{sky} \right) \hat{E}_{det} \\
&= \left(O_r^T \cdot O_{sky} \right)^T J_{vpm}(\theta, \phi, z, \nu) \left(O_r^T \cdot O_{sky} \right) \hat{E}_{det}.
\end{aligned} \tag{5.21}$$

While the matrices for O_r and O_{sky} are fairly complex, their combination is

$$O_r^T O_{sky} = \begin{bmatrix} \frac{-\sin(\Theta+el)}{L_{TE}} & \frac{\sin(az)\cos(\Theta+el)}{L_{TE}} & 0 \\ \frac{\sin(az)\cos(\Theta+el)}{L_{TE}} & \frac{\sin(\Theta+el)}{L_{TE}} & 0 \\ 0 & 0 & 1 \end{bmatrix}. \tag{5.22}$$

Where L_{TE} is the normalization required for the $\hat{e}_{TE}$ mode and is

$$L_{TE} = \sqrt{\cos^2(az)\sin^2(el + \theta_V) + \sin^2(az)}. \tag{5.23}$$

Intuitively, this combined matrix is the required transform from the basis where the detector angles are defined to the basis where interaction with the VPM is understood. When the azimuth offset for a detector is zero, it is the identity matrix with a single sign flip to record the effect of reflection off a surface. However, when the azimuth offset is non-zero, the ($\hat{e}_{TE}$, $\hat{e}_{TM}$) basis is no longer orthogonal to the basis vectors from the sky and rotations are required. This entire effect is less necessary for the case of an ideal VPM, where the reflection coefficients for the TE and TM modes are identical, but becomes important when the reflection coefficients for real materials are added into the model because the TE and TM mode reflections will differ by factors of $\cos\theta$.

In addition to the $O_r^T O_{sky}$ transform, we also need to calculate the values of θ and

ϕ that are required for the VPM Jones matrix (equation 5.14). The wavevector in VPM coordinates is the third column of O_{sky}

$$\hat{k} = (O_{sky})_{3i} = \begin{bmatrix} \cos(\Phi)\cos(az)\sin(\Theta + el) - \sin(\Phi)\sin(az) \\ \sin(\Phi)\cos(az)\sin(\Theta + el) + \cos(\Phi)\sin(az) \\ \cos(az)\cos(\Theta + el) \end{bmatrix}, \tag{5.24}$$

and we can calculate θ and ϕ directly from this wavevector:

$$\begin{aligned} \cos\theta &= \hat{k} \cdot \hat{n} = \cos(az)\cos(\Theta + el) \\ \tan\phi &= \frac{\hat{k} \cdot \hat{a}}{\hat{k} \cdot \hat{w}} = \frac{\sin(\Phi)\cos(az)\sin(\Theta + el) + \cos(\Phi)\sin(az)}{\cos(\Phi)\cos(az)\sin(\Theta + el) - \sin(\Phi)\sin(az)}. \end{aligned} \tag{5.25}$$

With equations 5.14, 5.22 and 5.25 we can now completely define the effect of the VPM in terms of the pointing parameters for each detector (Θ, Φ, az, and el) and the reflection coefficients off the VPM ($\Gamma_{w,TE}$, $\Gamma_{w,TM}$, $\Gamma_{a,TE}$, $\Gamma_{a,TE}$). This is all that is required to describe how the VPM modulates polarization from the sky. The last piece to add is a Jones matrix describing the detector response, since the CLASS detectors observe a single linear polarization, the detector can be modeled as a Jones matrix for a linear polarizer rotated at some angle α.

$$J_{det} = \begin{bmatrix} \cos^2\alpha & \cos\alpha\sin\alpha & 0 \\ \cos\alpha\sin\alpha & \sin^2\alpha & 0 \\ 0 & 0 & 1 \end{bmatrix}. \tag{5.26}$$

There are two Jones matrices of interest, which can be defined explicitly as

$$\begin{aligned} J_{tot,sky}(\Theta, \Phi, az, el) &= \left(O_r^T \cdot O_{sky}\right)^T J_{vpm}(\theta, \phi) \left(O_r^T \cdot O_{sky}\right) \\ J_{tot,det}(\Theta, \Phi, az, el, \alpha) &= J_{det} \left(O_r^T \cdot O_{sky}\right)^T J_{vpm}(\theta, \phi) \left(O_r^T \cdot O_{sky}\right). \end{aligned} \tag{5.27}$$

These total Jones matrices can be evaluated at $\Theta \neq 0$, $\Phi = \frac{\pi}{2}$, and $az = el = 0$ as a

simple example of VPM modulation. Plugging these values into O_{sky} produces

$$\hat{k} = \begin{bmatrix} 0 \\ \sin\Theta \\ \cos\Theta \end{bmatrix}, \quad \theta = \Theta, \quad \text{and} \quad \phi = \Phi = \frac{\pi}{2}. \tag{5.28}$$

From there we calculate J_{vpm} and $O_r^T O_{sky}$ as

$$J_{VPM} = \begin{bmatrix} -1 & 0 & 0 \\ 0 & -e^{i\delta} & 0 \\ 0 & 0 & 1 \end{bmatrix} \quad \text{and} \quad O_r^T O_{sky} = \begin{bmatrix} -1 & 0 & 0 \\ 0 & 1 & 0 \\ 0 & 0 & 1 \end{bmatrix} \tag{5.29}$$

and then the total Jones matrix from the sky is

$$J_{tot,sky}\left(\Theta, \frac{\pi}{2}, 0, 0\right) = \begin{bmatrix} -1 & 0 & 0 \\ 0 & -e^{i\delta} & 0 \\ 0 & 0 & 1 \end{bmatrix}. \tag{5.30}$$

We can translate the 2D Jones matrix into a Mueller Matrix using the standard transform defined in equation A.3

$$M_{tot,sky}\left(\Theta, \frac{\pi}{2}, 0, 0\right) = \begin{bmatrix} 1 & 0 & 0 & 0 \\ 0 & 1 & 0 & 0 \\ 0 & 0 & \cos\delta & -\sin\delta \\ 0 & 0 & \sin\delta & \cos\delta \end{bmatrix}. \tag{5.31}$$

This Mueller matrix confirms the modulation of Stokes U into Stoke V described in chapter 4 equation 4.2 for the main beam of the instrument. Adding a detector angle into the description we get

$$J_{tot,det}\left(\Theta, \frac{\pi}{2}, 0, 0, \alpha\right) = \begin{bmatrix} -\cos^2\alpha & -e^{i\delta}\cos\alpha\sin\alpha & 0 \\ -\cos\alpha\sin\alpha & -e^{i\delta}\sin^2\alpha & 0 \\ 0 & 0 & 1 \end{bmatrix}, \tag{5.32}$$

This matrix can also be turned into a Mueller matrix, however, the CLASS detectors are total power detectors, meaning sensitivity to the sky Stokes parameters only

depends on the top row of that Muller matrix. So the power measured by the detectors is

$$\begin{aligned} P_{\rm det}\left(\Theta, \frac{\pi}{2}, 0, 0, \alpha, z, \nu\right) =& \frac{1}{2} I_{\rm sky}(\nu) + \frac{1}{2}\cos(2\alpha) Q_{\rm sky}(\nu) \\ &+ \frac{1}{2}\sin(2\alpha)\cos\left(\frac{4\pi\nu}{c} z\cos\theta\right) U_{\rm sky}(\nu) \\ &+ \frac{1}{2}\sin(2\alpha)\sin\left(\frac{4\pi\nu}{c} z\cos\theta\right) V_{\rm sky}(\nu) \end{aligned} \tag{5.33}$$

where the dependence on the grid-mirror distance z and the frequency ν have been reinstated. The optical design of the CLASS telescopes has $\alpha = \pm 45^\circ$ degrees to maximize the level of polarization modulation and minimize sensitivity to the other linear polarization. The modulation functions first defined in chapter 4 equation 4.3 are calculated from the frequency integration of the above equation, to be

$$\begin{aligned} S_0(z) &= \frac{1}{2}\frac{dP}{dT}\int_0^\infty d\nu B(\nu)\frac{I(\nu)}{\bar{I}} \\ S_1(z) &= \frac{1}{2}\frac{dP}{dT}\int_0^\infty d\nu B(\nu)\frac{Q(\nu)}{\bar{Q}}\frac{dP}{dT}\cos(2\alpha) \\ S_2(z) &= \frac{1}{2}\frac{dP}{dT}\int_0^\infty d\nu B(\nu)\frac{U(\nu)}{\bar{U}}\frac{dP}{dT}\sin(2\alpha)\cos\left(\frac{4\pi\nu}{c} z\cos\theta)\right) \\ S_3(z) &= \frac{1}{2}\frac{dP}{dT}\int_0^\infty d\nu B(\nu)\frac{V(\nu)}{\bar{V}}\frac{dP}{dT}\sin(2\alpha)\sin\left(\frac{4\pi\nu}{c} z\cos\theta)\right). \end{aligned} \tag{5.34}$$

In these equations, $B(\nu)$ is the CLASS detector bandpass, the barred values are the average Stokes parameters across the detector bandpass in temperature units, and $\frac{dP}{dT}$ converts the temperature on the sky to power on the detector. For the rest of this thesis, the factor of $\frac{1}{2}\frac{dP}{dT}$ is divided out of the modulation functions because it is the overall calibration of the instrument and detectors. Normalizing the modulation functions by this factor separates the absolute calibration of the instrument from the

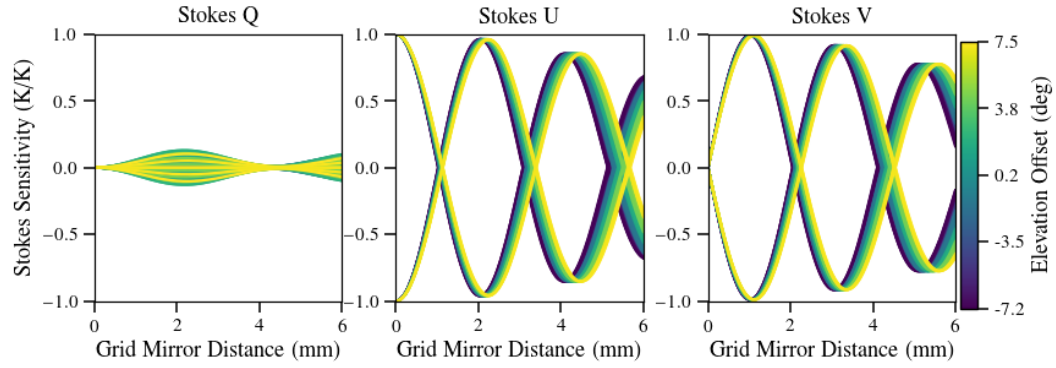

Figure 5.6: The modulation functions S_1 (left), S_2 (center), and S_3 (right), such as those defined in equation 5.34, but evaluated at the detector pointing for each detector in the Q-band focal plane. The colors of the lines are set by the elevation offsets for each detector, which illustrates the dependence of the modulation on the angle of incidence of the detector on the VPM.

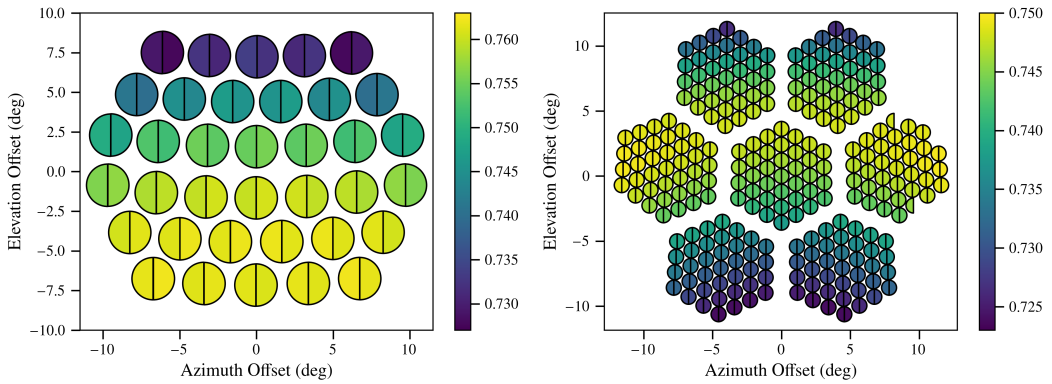

Figure 5.7: The modulation efficiency for each detector in the Q-band (left) and W-band (right) focal planes assuming the optical throw parameters defined in table 4.1. The Q-band modulation functions include the "real" simulated bandpass for the Q-band detectors while the W-band modulation functions only include a top-hat bandpass. The difference in bandpasses accounts for the difference in positioning of the pixels with the highest modulation efficiency.

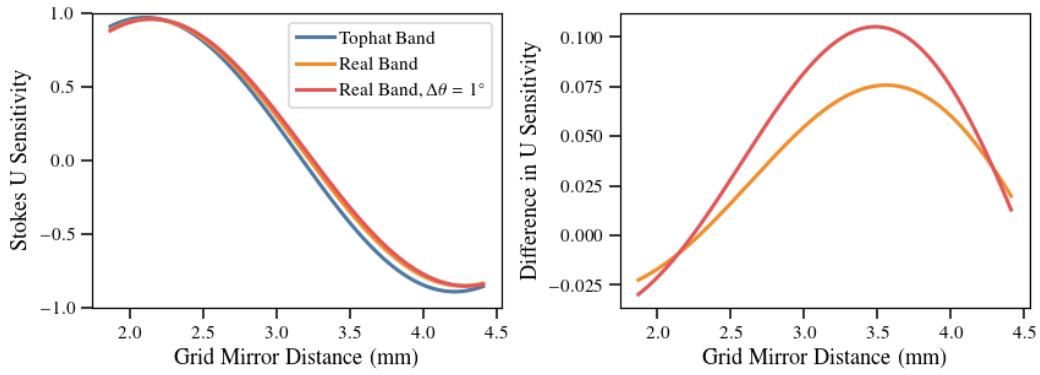

Figure 5.8: Left: The sensitivity to the Stokes U parameter, $S_2(z)$, for a Q-band detector with a top hat bandpass (33-43 GHz) compared to the "real" simulated bandpass of the on-chip filters for the Q-band detectors. Also plotted is the model with the real bandpass with a slightly miscalibrated angle of incidence. Right: the difference between the models with real bandpasses and the model with a tophat bandpass. The change in bandpass causes the modulation functions to vary by up to 7% across the VPM throw, which is a larger effect than the change due to a miscalibrated angle of incidence.

modulation effects of the VPM.

Figure 5.6 shows these modulation functions, but evaluated for each detector pointing in the Q-band CLASS focal plane. The lines are colored by the elevation offset of each detector to show how the modulation depends on angle of incidence. Figure 5.7 shows the modulation efficiency, as defined in chapter 4 equation 4.4, for every pixel in the focal plane for the Q-band and W-band telescopes using the VPM throws defined in table 4.1.

As an example of the effect of detector bandpass on the VPM modulation functions, the left plot in figure 5.8 shows the sensitivity to the Stokes U parameter, $S_2(z)$, for a Q-band detector with a top hat bandpass (33-43 GHz) compared to the "real" simulated bandpass of the on-chip filters for the Q-band detectors. The last line shows the real bandpass with a slightly miscalibrated angle of incidence. The right plot in figure 5.8 shows the difference between the real bandpasses and the tophat bandpass. The

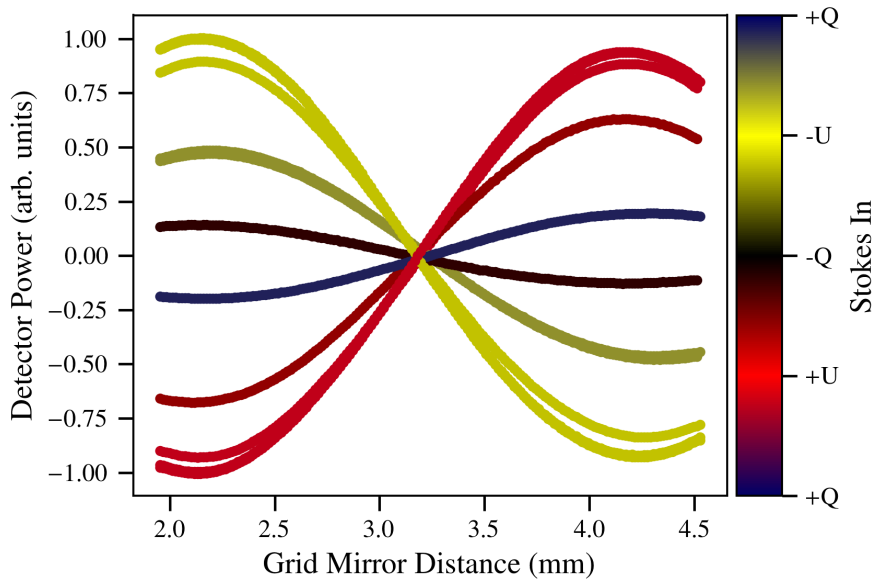

Figure 5.9: An example polarization calibration measurement for a Q-band detector. A linear polarization is input in front of the telescope aperture using a sparse wire grid that is rotated to change the direction of the polarization. Fitting these measurements to the modulation functions defined above is one way to extract the various parameters describing the optical system.

change in bandpass causes the modulation functions to vary by up to 7% across the VPM throw, which is a larger effect than the change due to a miscalibrated angle of incidence. The size of this effect means understanding the bandpass of the CLASS telescopes and correctly including the effects in the VPM transfer functions is vital to extracting the true Stokes parameters from the sky.

One of the ways to calibrate the VPM transfer functions is using a sparse wire grid polarizer in front of the telescope aperture to input a linear polarization. Figure 5.9 shows an example of this sort of test for a detector near the center of the Q-band focal plane. The response of the detector is highest when the sparse wire grid is aligned with $\pm U$ and is significantly lower when the wire grid is aligned closer to $\pm Q$. Fitting this measurements to the modulation functions in equation 5.34 is one way to extract

parameters describing the system.

5.2 Realistic Grids and Mirrors

Section 5.1 built up the transfer functions of the VPM in terms of the pointing for all the detectors and this section will focus on how to calculate the reflection coefficients for the VPM for the different modes and accounting for real materials. The basis for these ideas come from Pozar (2012), Goldsmith (1998), Marcuvitz (1951), and Chuss et al. (2012). Chuss et al. (2012) built a transmission line model for the VPM using transmission line models for wire grids, delays, and mirrors. In this section the same calculations are set up but in a slightly different way that is more useful for understanding the emission properties of the VPM described in section 5.3.

5.2.1 Wire Grid Model

The level of reflection, transmission and loss on incidence with a wire grid depends on the various modes of the electric fields interacting with the grid. First, reflection and transmission depends on if the electric field is parallel or perpendicular to the wires. Second, it depends on if the electric field is part of a TE or TM mode.

Electric fields parallel to the wires are often described as the "inductive" modes while electric fields perpendicular to the wires are "capacitive" modes. The reasoning for this naming structure can be seen in figure 5.10, where inductive and capacitive grids are drawn with their equivalent transmission line circuitry. The transmission line equivalents are from Marcuvitz (1951). The associated ABCD matrix

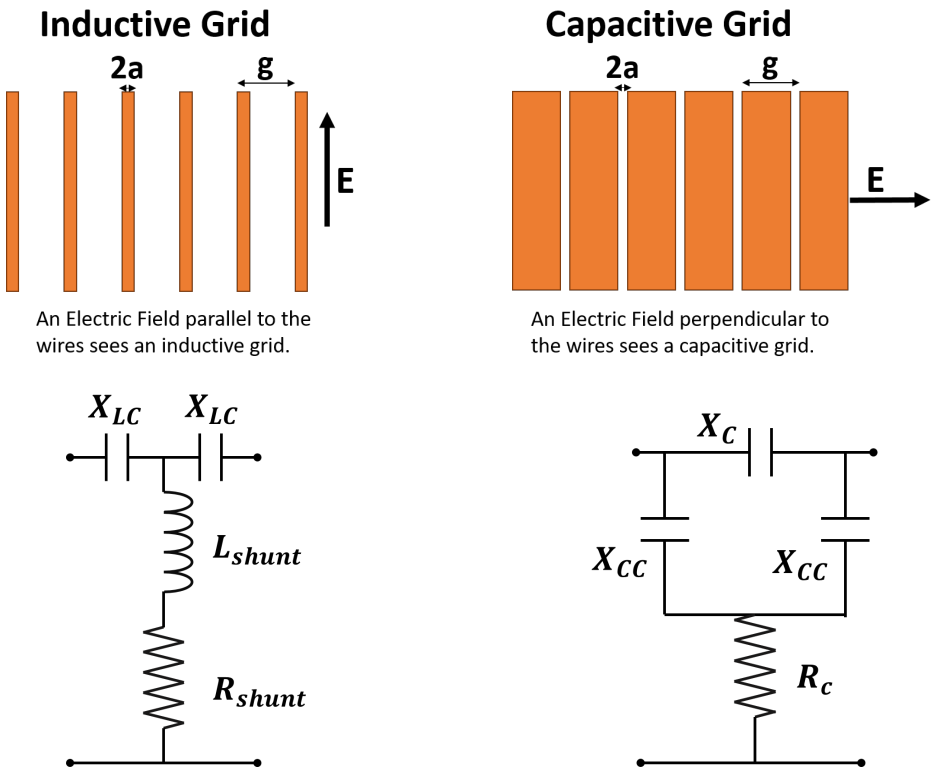

Figure 5.10: The image in the top left shows an inductive wire grid, where the electric field is parallel to the wires. The top right shows the complementary capactitive grid, where the inverse of the inductive grid can be used to directly calculate the reflection and transmission parameters for the electric field perpendicular to the wires (Goldsmith, 1998). The equivalent transmission line descriptions of the inductive and capacitive grids are shown in the bottom row and were adapted from (Marcuvitz, 1951).

(see appendix C on ABCD matrices) for the inductive modes is

$$ABCD_{grid,ind} = \begin{bmatrix} 1 + \frac{iX_{LC}}{R_L + iX_L} & \frac{1}{R_L + iX_L} \\ 2iX_{LC} - \frac{X_{LC}^2}{R_L + iX_L} & 1 + \frac{iX_{LC}}{R_L + iX_L} \end{bmatrix} \tag{5.35}$$

and the capacitive mode ABCD matrix is

$$ABCD_{grid,cap} = \mathcal{N} \begin{bmatrix} iX_C + iX_{CC} + \left(2 + \frac{X_C}{X_{CC}}\right) R_C & (2R_c + iX_{CC})\, iX_C \\ 2 + \frac{X_C}{X_{CC}} & \left(2 + \frac{X_C}{X_C C}\right) R_C + \left(1 + \frac{X_C}{X_{CC}}\right) iX_{CC} \end{bmatrix}$$

$$\mathcal{N} = \frac{1}{iX_{CC} + \left(2 + \frac{X_C}{X_{CC}}\right) R_C}. \tag{5.36}$$

When $2a << g$, it is possible to obtain analytic solutions for the values of the various capaciters, resisters, and inductors in these matricies, however, as $2a$ approaches g the necessary approximations break down (Marcuvitz, 1951). Wire grids used al linear polarizers at microwave wavelengths generall have $2a \sim g$, so Chuss et al. (2012) simulated the various wire grid modes as a function of a and g for values in this range and found numerical relations for the transmission line parameters when $2a \sim g$. In addition, they tested these models with the VPM used for the Hertz instrument that operated at $\lambda = 353$ μm and fit for the various circuit parameters for that VPM.

To model the wire grids for the CLASS telescopes, we scale the circuit parameters fit to the Hertz grid in Chuss et al. (2012) by the ratios of the dimensions describing the CLASS and Hertz wire grids. The values describing the Hertz and CLASS grids

are

$$g_{fac} = \frac{g_{\text{CLASS}}}{g_{\text{Hertz}}} = \frac{160\ \mu\text{m}}{67\ \mu\text{m}}, \qquad a_{fac} = \frac{a_{\text{CLASS}}}{a_{\text{Hertz}}} = \frac{25\ \mu\text{m}}{12.5\ \mu\text{m}},$$
$$\lambda_{fac} = \frac{\lambda_{\text{CLASS}}}{\lambda_{\text{Hertz}}} = \frac{9.0\ \text{mm}}{353\ \mu\text{m}} \rightarrow \frac{1.0\ \text{mm}}{353\ \mu\text{m}}, \qquad \sigma_{fac} = \frac{\sigma_{\text{CLASS}}}{\sigma_{\text{Hertz}}} = \frac{5.96 \times 10^7\ \text{S/m}}{1.97 \times 10^7\ \text{S/m}} \tag{5.37}$$

and the scaling of the different circuit parameters are done as

$$\begin{aligned}
L_{s,CLASS} &= L_{s,Hertz} \times \left(\frac{g_{fac}}{\lambda_{fac}}\right)\left(\frac{g_{fac}}{a_{fac}}\right) \\
R_{s,CLASS} &= R_{s,Hertz}\sqrt{\frac{\lambda_{fac}}{\sigma_{fac}}} \\
X_{LC,CLASS} &= X_{LC,Hertz} \times \left(\frac{g_{fac}}{\lambda_{fac}}\right)\left(\frac{a_{fac}}{g_{fac}}\right)^2 \\
X_{cc,CLASS} &= X_{cc,Hertz} \times \left(\frac{g_{fac}}{\lambda_{fac}}\right)\left(\frac{a_{fac}}{g_{fac}}\right)^2 \\
X_{c,CLASS} &= X_{c,Hertz} \times \left(\frac{\lambda_{fac}}{g_{fac}}\right)\left(\frac{g_{fac}}{a_{fac}}\right)^2 \\
R_{cc,CLASS} &= R_{cc,Hertz} \sim 0
\end{aligned} \tag{5.38}$$

The significant difference in wavelength between the Hertz and CLASS regimes results in most of these circuit parameters being pushed much lower for CLASS than for the Hertz grids, well into the range of ideal operation. The reflection and transmission coefficients for the wire grids can be calculated directly from the the ABCD matrices using equation C.1; accounting for the effective impedance of free space differing for TE and TM modes. $Z_{eff} = Z_0/\cos\theta$ for TE modes and $Z_{eff} = Z_0\cos\theta$ for TM modes. The source of the effective impedance differences comes from calculating how plane waves reflect off surfaces at oblique incidence and determining the required adjustments to the transmission line model (Bronwell, 1944).

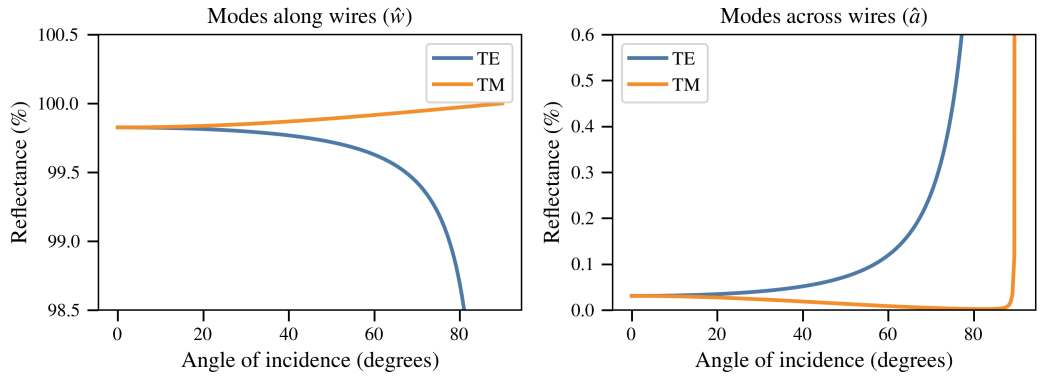

Figure 5.11: The reflection coefficients for different modes incident on a wire grid described by the CLASS circuit parameters at 40 GHz. The reflection for modes along the wires is driven by the value of R_{shunt} that describes the conductivity of the wires. The reflection differences at $\theta = 20^\circ$ are less that 0.3%. The modeling does not account for the change in effective filling factors at large angles of incidence and should not be trusted at high angle on incidence.

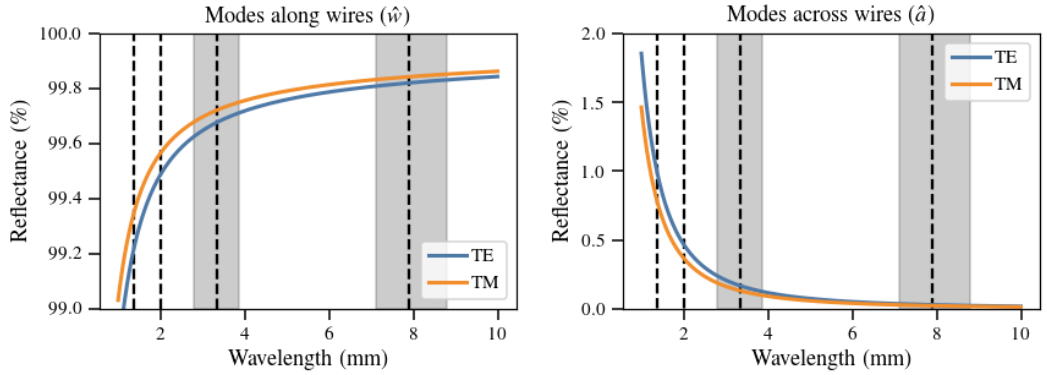

Figure 5.12: The reflection coefficients for the CLASS wire grids with $\theta = 20^\circ$ as a function of wavelength. The dashed lines indicate the center wavelengths of the four CLASS bands while the shaded regions denote the width of the bandpasses for the 40 and 90 GHz detectors. The loss and non-ideal reflection from the wire grids will be much higher for the HF telescope than for the Q or W-band telescopes.

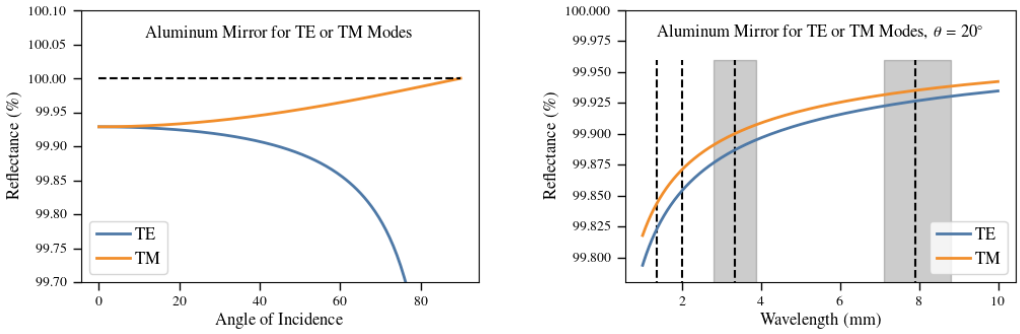

Figure 5.13: The left plot shows the reflectance off an aluminum mirror at 40 GHz as a function of angle of incidence. The difference between the reflection of TE and TM modes causes a slight $T \rightarrow P$ leakage. The right plot shows the reflectance at $\theta = 20^\circ$ as a function of wavelength. The dashed lines indicate the center wavelengths of the four CLASS bands while the shaded regions denote the width of the bandpasses for the 40 and 90 GHz detectors.

Figure 5.11 shows how the reflection along the wires and perpendicular to the wires changes as a function angle of incidence for the different electric field modes at 40 GHz. The difference in reflectance between the TE and TM modes at an angle of incidence of 20° is less than 0.03% for modes parallel and perpendicular to the wires. Figure 5.12 shows the reflectance off the wires for all modes at an angle of incidence of 20° as a function of wavelength, with the center of the CLASS bands marked by black dashed lines. Following the techniques described above, we can calculate all the relevant reflection and transmission coefficients for the wire grid: $r_{w,TE}$, $r_{a,TE}$, $r_{w,TM}$, $r_{a,TM}$, $t_{w,TE}$, $t_{a,TE}$, $t_{w,TM}$, and $t_{a,TM}$.

5.2.2 Mirror Model

Modeling the VPM mirror is much simpler than the wire grid, because the transmission line model of a mirror is just a resistor where the impedance depends on the wavelength, conductivity of the material, and if the electric field is a TE or TM mode (see equation B.13). Figure 5.13 shows the reflectance as a function of angle of

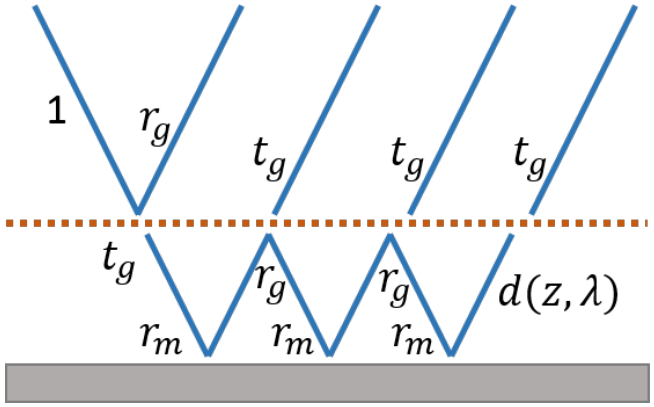

Figure 5.14: An example raytrace from the sky for a real VPM. The ray labeled 1 is the incoming ray while all other outgoing rays must be summed coherently to obtain the complete transfer function.

incidence for Q-band and as a function of wavelength for $\theta = 20°$.

5.2.3 Combined Reflection Model

For realistic wire grids, the transmission of modes parallel to the wires and the reflection of modes perpendicular to the wires are non-zero. The effect of this, shown as a ray trace in figure 5.14, is that modes can become trapped between with wire grid and the mirror. There are several possible ways to calculate the complete reflection off the VPM accounting for these effects. Chuss et al. (2012) calculated a combined ABCD matrix, built from ABCD matrices describing the wire grid, a delay, and the mirror. The reflection coefficients for each mode were then calculated from the equivalent scattering matrix for the combined ABCD matrix. Here, I will use the reflection and transmission coefficients for the wire grid, the reflection coefficients for the mirror, and a delay

$$d_z(\theta, z, \nu) = e^{i\delta}, \tag{5.39}$$

to calculate the reflection coefficients for the VPM. This is mathematically equivalent to the ABCD matrix approach but is more intuitive for describing the emission from the VPM in section 5.3.

As figure 5.14 indicates, the trapped modes in the VPM can reflect many times before escaping the VPM, and since all the rays leaving the VPM are along the same wavevector, they all add coherently. Tracing the electric field through the VPM, we see that

$$\begin{aligned} E_{\text{out}} &= \Gamma_{\text{mode}}\, E_{\text{in}} \\ &= \left(r_g + t_g^2 r_m d + t_g^2 r_g r_m^2 d_z^2 + t_g^2 r_g^2 r_m^2 d_z^3 + \dots \right) E_{\text{in}} \\ &= \left(r_g + t_g^2 \sum_{n=0}^{\infty} (r_m d_z)^{n+1} r_g^n \right) E_{\text{in}} \\ &= \left(r_g + \frac{t_g^2 r_m d_z}{1 - r_g r_m d_z} \right) E_{\text{in}}. \end{aligned} \tag{5.40}$$

Here, r_g and t_g are the coefficents for a single mode (TE or TM, parallel or perpendicular to the wires) and r_m is the reflection coefficient for the mirror in either the TE or TM mode. Γ is calculated in this manner for each of the possible modes and then input into the VPM Jones matrix in equation 5.14.

Figure 5.15 illustrates how the realistic wire grids and mirrors change the modulation functions for the W-band VPM, calculated with a top-hat bandpass for W-band. For ideal VPMs, Stokes I and Q are unmodulated, for realistic VPMs they are. These effects come from a combination of phase shifts on reflection off real metals, a difference in emissivity between copper and aluminum, and non-normal incidence creating $T \rightarrow P$ on reflection. The middle right and bottom right plot in figure 5.15 shows the difference in modulation function for Stokes U and V for between a real and ideal

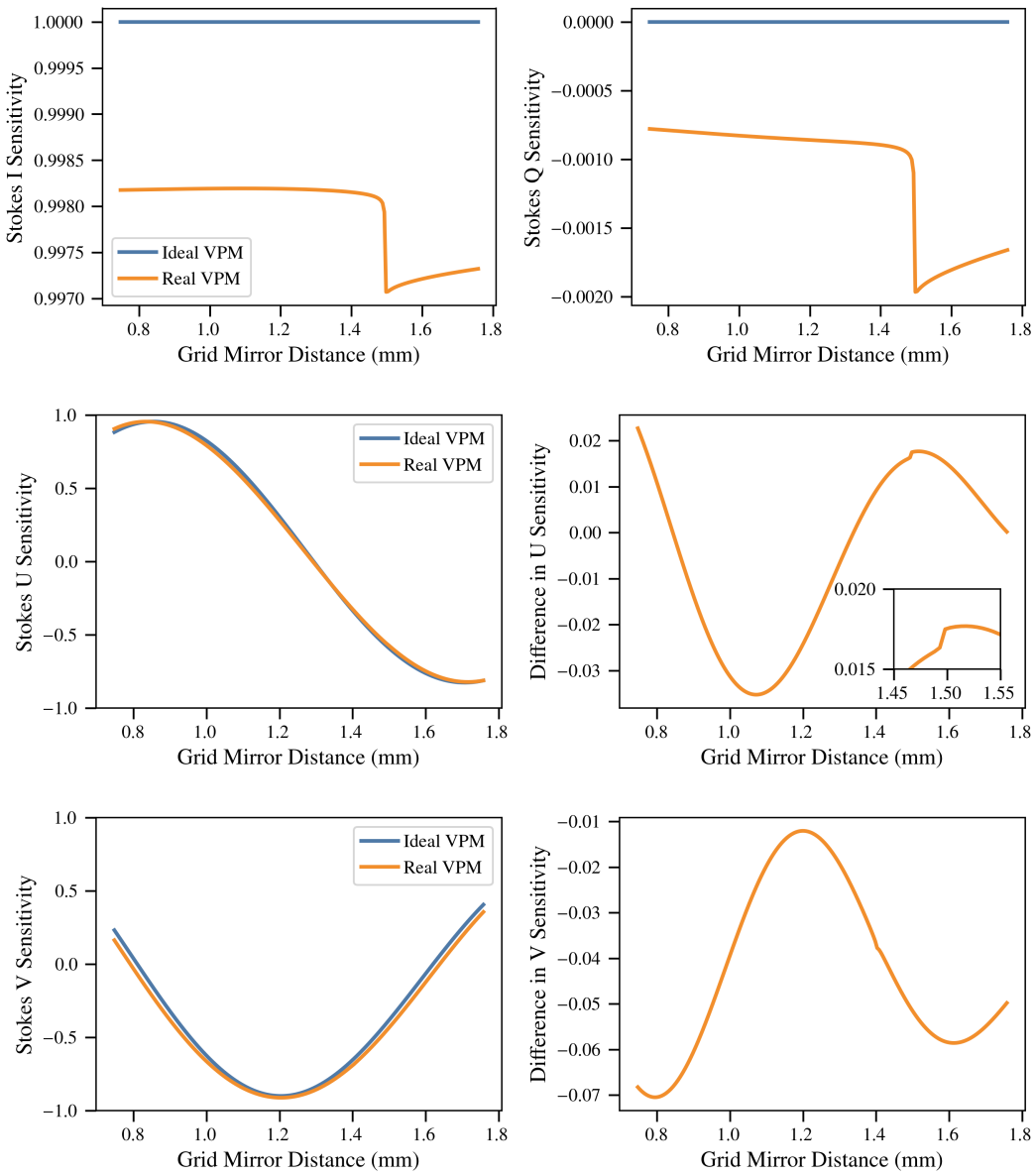

Figure 5.15: The sensitivity to the Stokes parameters for real and ideal VPMs for the W-band telescopes assuming a top-hat bandpass for the W-band detectors. Top left: Stokes I, top right: Stokes Q, middle left: Stokes U, bottom left: Stokes V. The middle right and bottom right show the difference between the real and ideal models for Stokes U and V, respectively.

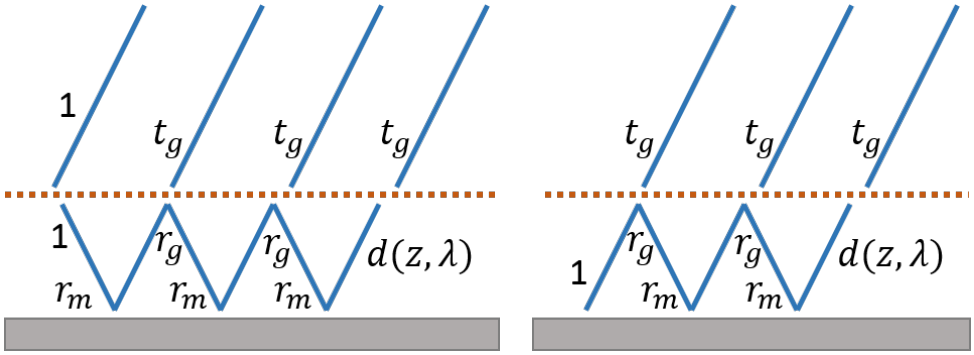

Figure 5.16: And example raytrace for emission coming out of the grid (left) and mirror (right) that will be detected by the detectors in the focal plane. The rays labeled 1 indicate the source of the emission which can then coherently interfere as it is partially reflected, delayed, and transmitted through the VPM.

VPM, an effect which is at a level of about 5% for W-band. All these modulation functions show resonance features which appear at a quarter wavelength delay. The resonance integration across the frequency band creates the square-wave-like nature of the modulation functions of I and Q.

Since the CLASS telescopes are looking through an unpolarized 10 K atmosphere at a largely unpolarized 3 K source, the modulation of Stokes I is one source of a VPM synchronous signal that is present in all CLASS data.

5.3 Emission from VPM

All materials at finite temperatures emit some amount of radiation, and the emissivity of a material is related to the reflection and transmission coefficients through energy conservation,

$$\epsilon = 1 - r^* r - t^* t$$
$$T_{\text{out}} = \epsilon T. \tag{5.41}$$

Thermal emission is incoherent, meaning the emission from various sources can not be coherently summed. However, if emission from some source is partially reflected, delayed, and then transmitted along the same path, that emission will coherently interfere with itself. This is schematically shown in figure 5.16, emission from the wire grid or the mirror goes through a frequency and delay dependent filter based on reflections off the wire grid and mirror. In effect, emission from both the wire grid and the mirror is polarized and modulated due to the interaction between wire grid and mirror surfaces.

Table 5.2 shows another way to draw the sources of emission around the VPM and the slight differences in filters experienced by each source; the filters are calculated analogously to equation 5.40 but consider the number of reflections or transmissions required depending on the source location. Since the filtering by the wire grid occurs for both grid and mirror emission, both sources have four effective modes of emission,

$$\begin{aligned} \Psi_{\mathrm{g,i}} &= \left(1 + \frac{t_{g,i} r_{m,i} d_z}{1 - r_{g,i} r_{m,i} dz}\right) \sqrt{\epsilon_{g,i}} \\ \Psi_{\mathrm{m,i}} &= \left(\frac{t_{g,i}}{1 - r_{g,i} r_{m,i} dz}\right) \sqrt{\epsilon_{m,i}} \end{aligned} \tag{5.42}$$

Where g or m stands for coefficients from the grid or mirror and i is the respective mode (TE/TM and parallel or perpendicular to the wires). Optically, we combine these emission parameters into a Jones-like matrix that aligns each mode to the geometry of the system,

$$\mathcal{E} = \begin{bmatrix} \Psi_{TE,w} \sin^2\phi + \Psi_{TE,a} \cos^2\phi & (\Psi_{TM,w} - \Psi_{TM,a}) \cos\phi \sin\phi & 0 \\ (\Psi_{TE,w} - \Psi_{TE,a}) \cos\phi \sin\phi & \Psi_{TM,w} \cos^2\phi + \Psi_{TM,a} \sin^2\phi & 0 \\ 0 & 0 & 1 \end{bmatrix}. \tag{5.43}$$

Note, there are separate $\mathcal{E}$ matrices describing the emission from the wire grid and

Source	T-line Setup	Response
Sky Power[a]	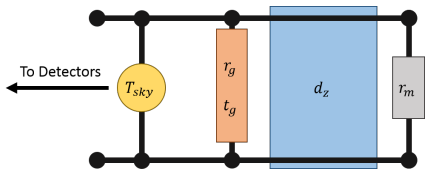	$T_{out} = \left(r_g + \frac{t_g^2 r_m d_z}{1 - r_g r_m d_z}\right) T_{in}$
Grid Emission	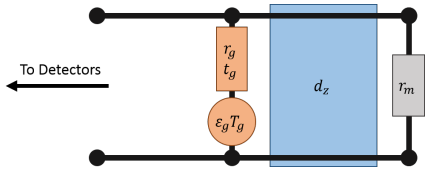	$T_{out} = \left(1 + \frac{t_g r_m d_z}{1 - r_g r_m d_z}\right) \epsilon_g T_g$
Mirror Emission	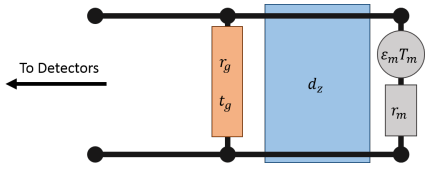	$T_{out} = \left(\frac{t_g}{1 - r_g r_m d_z}\right) \epsilon_m T_m$

Table 5.2: The different transmission line setups for the different sources present in the VPM. The circles represent sources *for a single mode of incidence or emission* while the rectangles are locations of reflection, transmission, or delay. Each the these reflection coefficients must be calculated for all for possible modes.

[a] This transmission line model for power from the sky is not quite correct because no power goes directly from the sky to the detectors, only the reflected power is incident on the detectors. However, this sketch is included here as a comparison to the other two sources of radiation and the listed response is correct because it includes only the terms which have reflected off the VPM at least once.

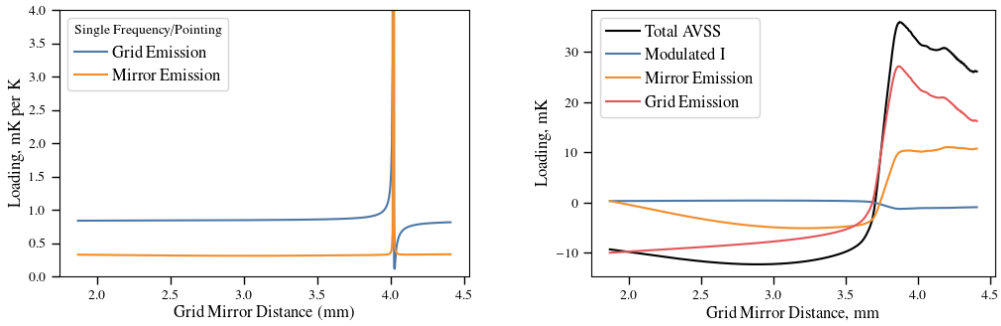

Figure 5.17: (Left) The emission of the grid and mirror for a single frequency and pointing (40 GHz, $\theta = 20°$) plotted as mK of emission per Kelvin of grid/mirror temperature. The emission from the grid is about twice that of the emission from the mirror. Both sources experiences resonances at a half wavelength delay between grid and mirror. (Right) The difference sources of the anomalous VPM synchronous signal (AVSS) integrated across the bandpass of the Q-band detectors and assuming the VPM is at 273 Kelvin and the sky is at 10 K.

emission from the mirror. The projection of each source of emission onto the detectors is

$$E^T_{proj} = E^T_{det} O^T_{sky} O_r \mathcal{E} \tag{5.44}$$

and so the temperature measured by the detectors is

$$T_{det} = \left(E^\dagger_{proj} E_{proj} \right) T_{vpm}. \tag{5.45}$$

The left plot in figure 5.17 shows $E^\dagger_{proj} E_{proj}$ for both the mirror and the grid evaluated at a single frequency and pointing (40 GHz, $\theta = 20°$). The emission from the grid is about twice the level of emission from the mirror, which matches other models of wire grid emission, but there are also resonance features indicating trapped modes between the grid and the mirror. The right plot in figure 5.17 shows the grid and mirror emission, along with modulated Stokes I, when it is integrated across the Q-band bandpass. The grid and mirror emission assumes both the wires and the grid are at 273 K and the modulated stokes I is plotted for a 10 K atmosphere. These

sources add together to produce the Anomalous VPM Synchronous Signal (AVSS), which is the signal that is synchronous with the VPM but is not from modulation of the polarized sky. All the lines in this plot have been high-pass filtered because the mean level of each source is different but the CLASS detectors can only measure the change in this signal as the VPM moves. This model for the AVSS does not completely account for what is observed in the Q-band telescope, which will be discussed in chapter 6.

Figure 5.18 shows how the emission from the wire grid and the mirror changes across the focal plane. The blue lines are for detectors with $\alpha = 45^\circ$ and the orange lines are for detectors with $\alpha = -45^\circ$. As the azimuth offsets of the detectors change, the amount each detector couples to the polarized emission from the wires and the mirror also rotates, causing the amplitude of the AVSS to increase as the azimuth offset increases for the $\alpha = 45^\circ$ detectors while it decreases for the $\alpha = -45^\circ$ detectors. This effect is seen in the measured AVSS for the Q-band system, shown in chapter 6 figure 6.10.

5.4 The Effect of Data Readout

Since the AVSS is a signal that is continuously visible in the CLASS data, it is useful for tracking the status of the detector data (more details in chapter 6). Matching the predicted AVSS shown here with the observed AVSS is still incomplete, however this effort has led to an expanded understanding of the possible sources of AVSS signals and the interaction of those signals with the rest of the data readout chain.

The process of biasing the transition edge sensors (TESs) into the transition region means the detectors can only measure relative changes in power and this bias step

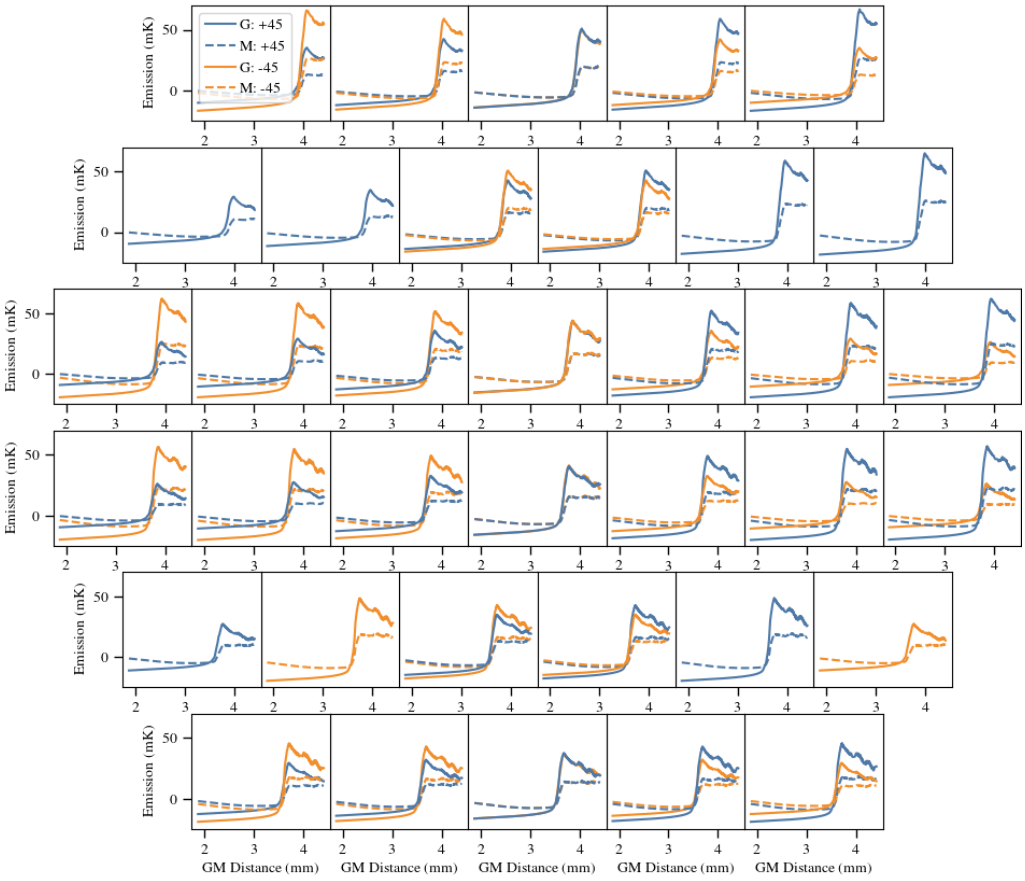

Figure 5.18: The mean-subtracted emission from the grid and mirror across the focal plane. The blue lines are for detectors with $\alpha = 45°$ and the orange lines are for detectors with $\alpha = -45°$. As the azimuth offsets of the detectors change, the amount each detector couples to the polarized emission from the wires and the mirror also rotates, causing the amplitude of the AVSS to increase as the azimuth offset increases for the $\alpha = 45°$ detectors while it decreases for the $\alpha = -45°$ detectors.

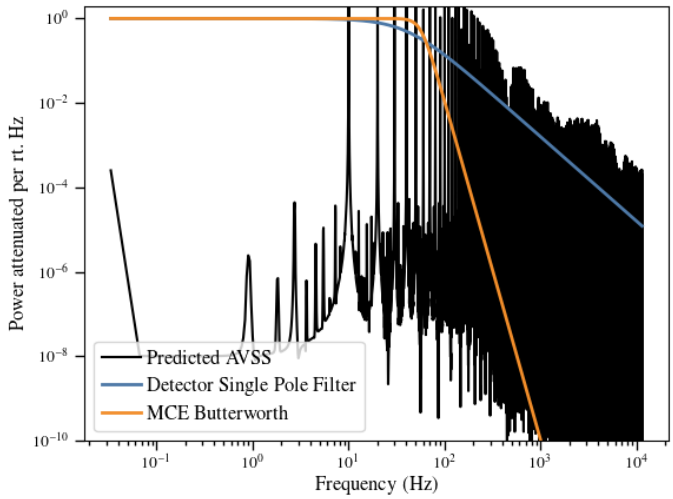

Figure 5.19: The filters applied to the detector timestreams for the CLASS data in comparison to the spectral content of the predicted AVSS. The black lines show the Fourier transform of a synthesized AVSS timestream, which has a significant amount of high-frequency modes since sharp band cutoffs create a nearly square wave signal in time. The blue line shows a single pole low pass filter for a typical detector time constant of 4 ms and the orange line shows the digital Butterworth filter applied by the MCE before the data is downsampled. Both lowpass filters significantly cut into the information content of the AVSS signature.

occurs in situ in the telescope. For this reason, it is not possible to measure the absolute level of the VPM emission and all the AVSS plots shown here are high-pass filtered or mean subtracted to reflect this. In addition, the power that is deposited onto the transition edge sensors and read out into detector timestreams is low-pass filtered twice. The detectors have an optical time constant that depends on the heat capacity of the TES, the thermal conductivity between the TES and the surrounding temperature bath, and the overall optical loading on the detector. This optical time constant functions as a single-pole low-pass filter on all the data. The MCE readout electronics sample the detectors at $\sim$ 23 kHz and then apply a digital Butterworth filter with a cutoff frequency of 50 Hz to prevent aliasing as the detector timestreams are downsampled to 200 Hz and saved to disk. Figure 5.19 shows these filters compared to the Fourier transform of a synthetic detector timestream. These low-pass filters cut out a large portion of the higher order modes predicted to be part of the AVSS.

The detector readout system will shift the AVSS signal as a function of grid mirror distance. Figure 5.20 shows an example of how the AVSS signature is processed. The top row shows the predicted shape of the AVSS as a function of grid mirror distance and the synthetic, zero-noise, time stream of detector data created assuming the VPM is moving at 9.97 Hz along the ideal mirror throw. The middle row shows what this data would look like as it is recorded in the CLASS data files. This is after a single-pole low-pass filter with a time constant of 4 ms and the digital MCE Butterworth has been applied to the data and it has been downsampled to 200 Hz. Assuming the filters applied to the data are known, they can be deconvolved from the recorded data. This is shown in the bottom row of figure 5.20 where perfectly matched filters

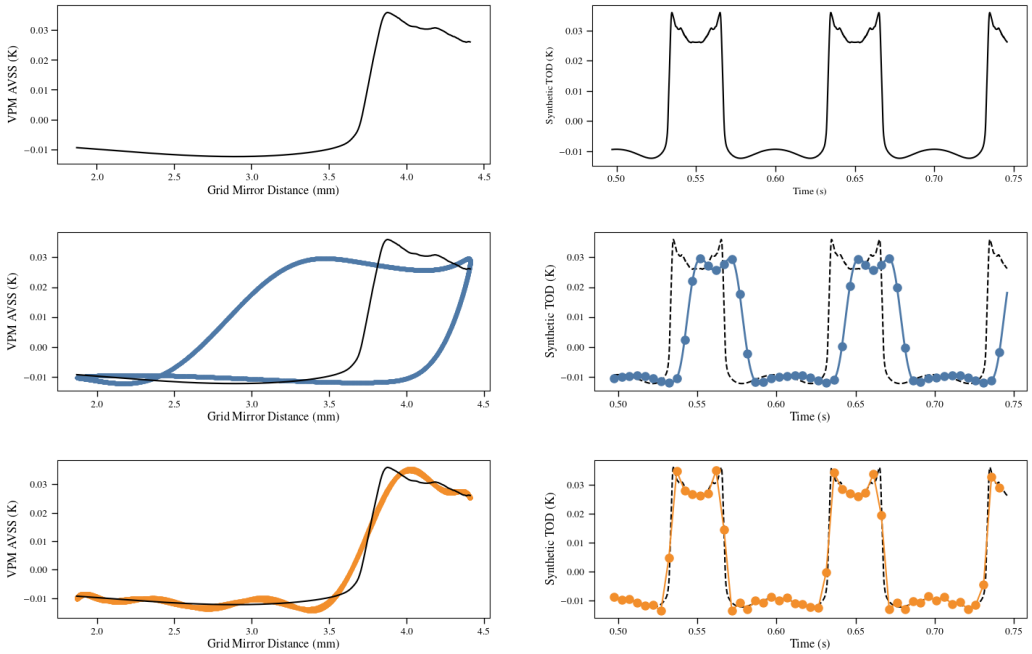

Figure 5.20: The effect of the detector readout system on the measured AVSS signature for the VPM. The top row shows the AVSS signal as a function of grid mirror distance on the left and a synthetic time stream of this signal on the right. The presence of resonances in the VPM emission structure and the sharpness of the detector bandpass creates a nearly square wave signal as a function of time. The middle row shows the same data after it has been low-pass filtered by the detector time constant and MCE Butterworth filter and downsampled to 200 Hz. These causal filters shift the AVSS in time with respect to the VPM position and downsampling removes the information about the higher frequency modes. The bottom row shows the same data when perfectly matched time constant and Butterworth filters have been deconvolved from the timestream.

have been deconvolved from the recorded data. While all filters used in this example are linear, the process of downsampling has caused a loss of information that results in a smoothing out of the AVSS signature.

Chapter 6

Data Analysis with a VPM

The CLASS telescopes implement a VPM as the first optical element from the sky to move the signal band of the data up to 10 Hz, above the $1/f$ knee of the instrument noise and to enable a significant amount of systematics rejection in the data. The first "era" for the Q-band CLASS telescope was between June 2016 and March 2018, when it was the only CLASS telescope on sky. The second era began in June 2018, where the Q-band telescope is now co-pointed with the first W-band telescope and both telescopes are taking data full time.

This chapter summarizes the analysis setup for CLASS data, particularly with regards to the VPM. Figure 6.1 sketches the analysis pipeline necessary to process time ordered data from the detectors. The blue boxes are aspects of the analysis that will always be required, the orange boxes are types of "data products" that are calculated and saved for all sections of data, green are aspects of the pipeline that can be done in various ways and are still being optimized, and yellow are test results that can be produced to feedback into the setup of the instrument itself or the development of the analysis pipeline. This chapter discusses the databases and data products built for quick and easy access to the detector data, the detector time constants, the AVSS

templates, the demodulation procedure, and shows initial data stability results.

6.1 Data Selection

6.1.1 Databases

We have built two SQL databases to track the status of the instrument and standardize how data is found and accessed through-out the collaboration.

The first database, called the data package database, is built directly off the custom data packaging software used by the CLASS telescopes. Data packages are created every 10 minutes and include all the possible data from the class site; this includes temperature data from the cryostats, telescope pointing, detector data, VPM positions, VPM controller data, weather data, etc. This data packaging is continuous whether or not any of the telescopes are observing and only rarely experiences interruptions during events such as power outages. The data package database has a row for every one of these 10 minute data packages and columns for the median value of every data type as well as booleans for information such as whether or not the detectors were taking data and if the VPM was on. The data package table has another connected table that has a row per detector per 10 minute data package where data is being acquired. Columns in this table include any per detector value of interest, such as variance, time constant(s), and fraction of data cut by our standard cut routines.

The comprehensiveness of the data package database has made it easy to create site status monitors such as the weekly observational summary shown in figure 6.2 and the daily detector status monitor shown in 6.3. These plots are automatically generated and posted daily to an internal page on the CLASS website to allow all members of the CLASS team to see what has been occurring with the observations

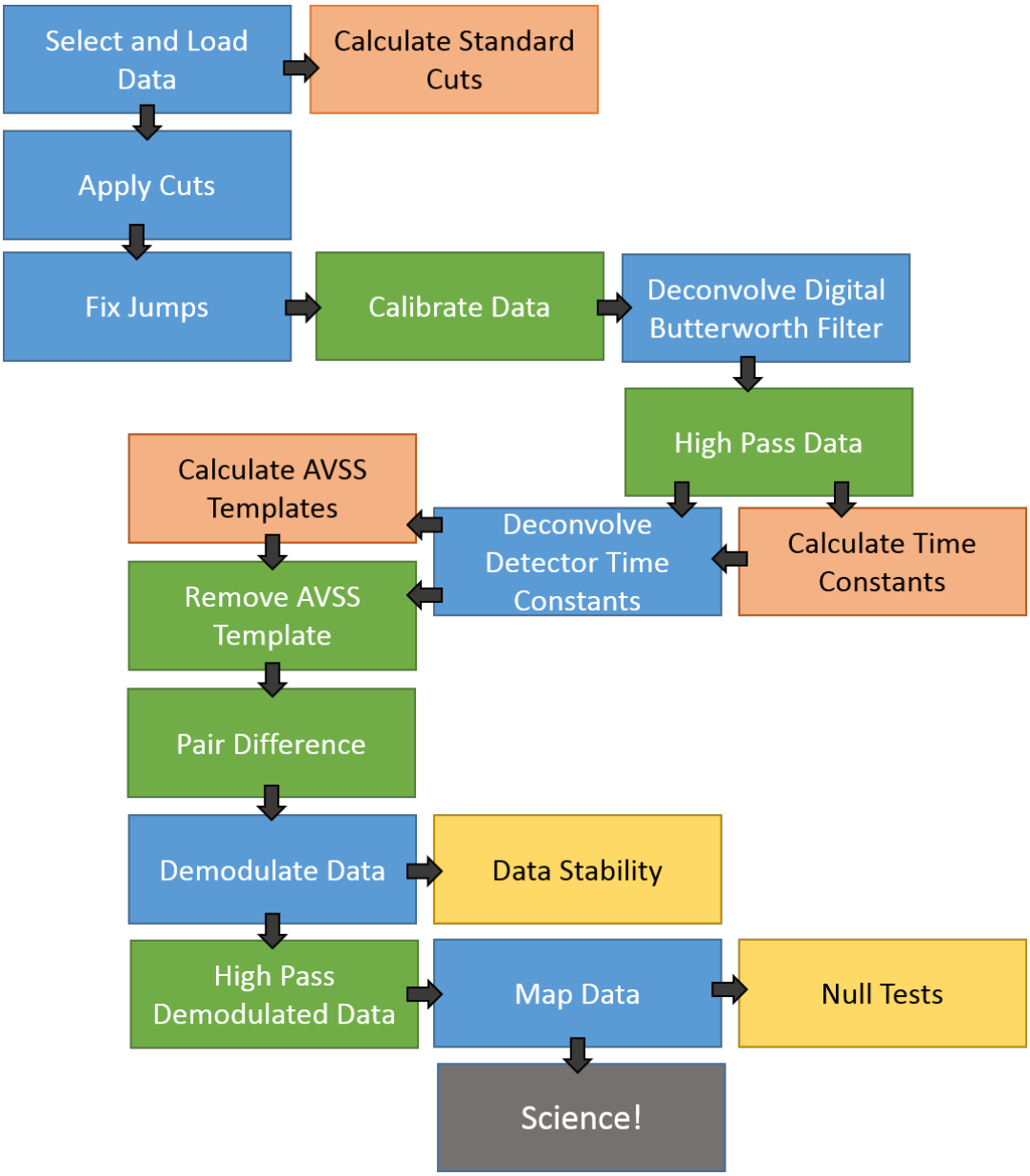

Figure 6.1: A flow chart describing the analysis pipeline for CLASS data. Blue are things which have to be done, Orange are data products saved for each set of data to decrease computation time, Green are steps which are optional/can be done in various ways, and Yellow are results which can be used to feed back into the rest of the setup to improve instrument or analysis setup.

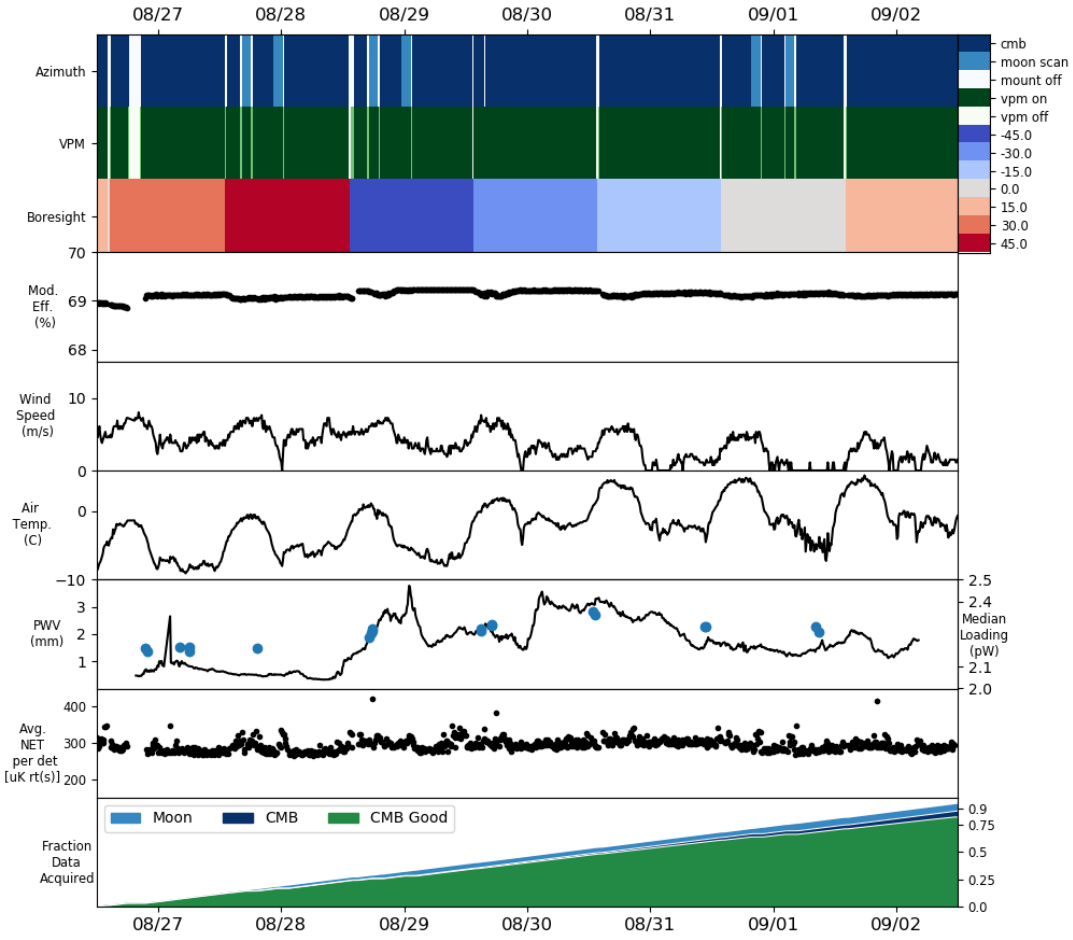

Figure 6.2: An example of the plot, automatically generated and posted daily to an internal CLASS webpage, used to summarize the status of the site during the last seven days. This plot includes information such as what types of observations were occurring during the week, if the VPM was performing as desired, the weather, and some detector status metrics such as the array averaged NET and the fraction of data passing our current data cuts.

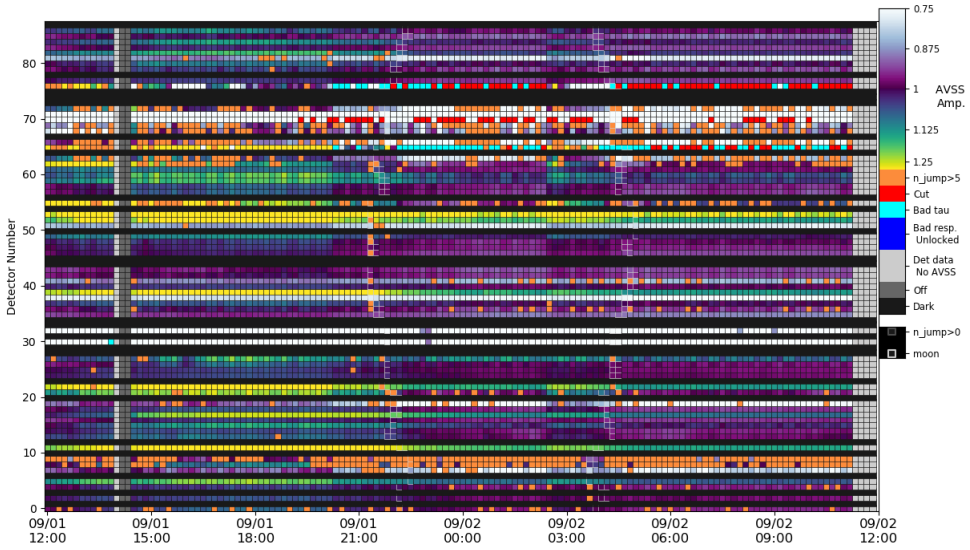

Figure 6.3: An example of the daily detector status plot that is automatically generated every day and summarizes the previous 24 hours of observing. This plot has a row per detector and a column per 10 minute data package over a 24 hour period. There are colors for many types of flags which would require the entire 10 minute period for that detector to be cut, and, if the detector passes all of those, the colors are an indication of the observed amplitude of the VPM synchronous signal.

for the week and the overall status of the detector data. The creation and continual upkeep of the data package database, in particular for the creation of the data status monitor plots, requires a significant portion of the standardized analysis scripts to be continually run on all incoming data, meaning there is often a very short time delay between when the overall status of the instrument changes and when we discover it changed.

The second SQL database we utilize, called the `AzSweep` database, is one based more formally on the observations the telescope is making. Observations of the telescopes are first divided into constant elevation scans (`CESs`), which are sections of uninterrupted CMB observation at a single elevation and boresight angle. During

CESs the telescope is scanning at 1° per second in azimuth at 45° elevation. The boresight angle is stepped 15° every day, so the longest CESs are about 24 hours. However, many are shorter than that due to work occurring at the site or targeted calibration observations. The top plot in figure 6.4 shows a week of CESs with their associated boresight angle and azimuth position during the CES. The second from the top plot in figure 6.4 shows the azimuth position during a single $\sim$ 24 hour CES. The periods of time when the range in azimuth covered by the telescope is limited to less that 360° is when sun avoidance is active. The CES table in the AzSweep database includes a row per CES with columns containing various observation parameters describing the CES as a whole.

The CES scans are divided into AzSweeps, where the telescope was scanning in only one direction. The lower middle plot in figure 6.4 is a zoom in to 2 hours of observing and shows how the AzSweep cutoffs are based on azimuth position. When sun avoidance is not required, AzSweeps are about 720° and 12 minutes long. The AzSweep table in the AzSweep database has a row per AzSweep and columns similar to that of the data package database such as weather, site, and VPM information. A third table, also analogous to the data package database, has a row per detector per AzSweep and includes all values relevant for indexing over particular detectors.

6.1.2 Data Products

Another tool that has been built to facilitate the analysis of detector time-ordered data is a suite of "data products." The distinguishing feature of these products is the software system managing them. This system will calculate products on-the-fly the first time they are requested, but will then automatically save and recall the data product for all subsequent requests. This setup significantly reduces the computation

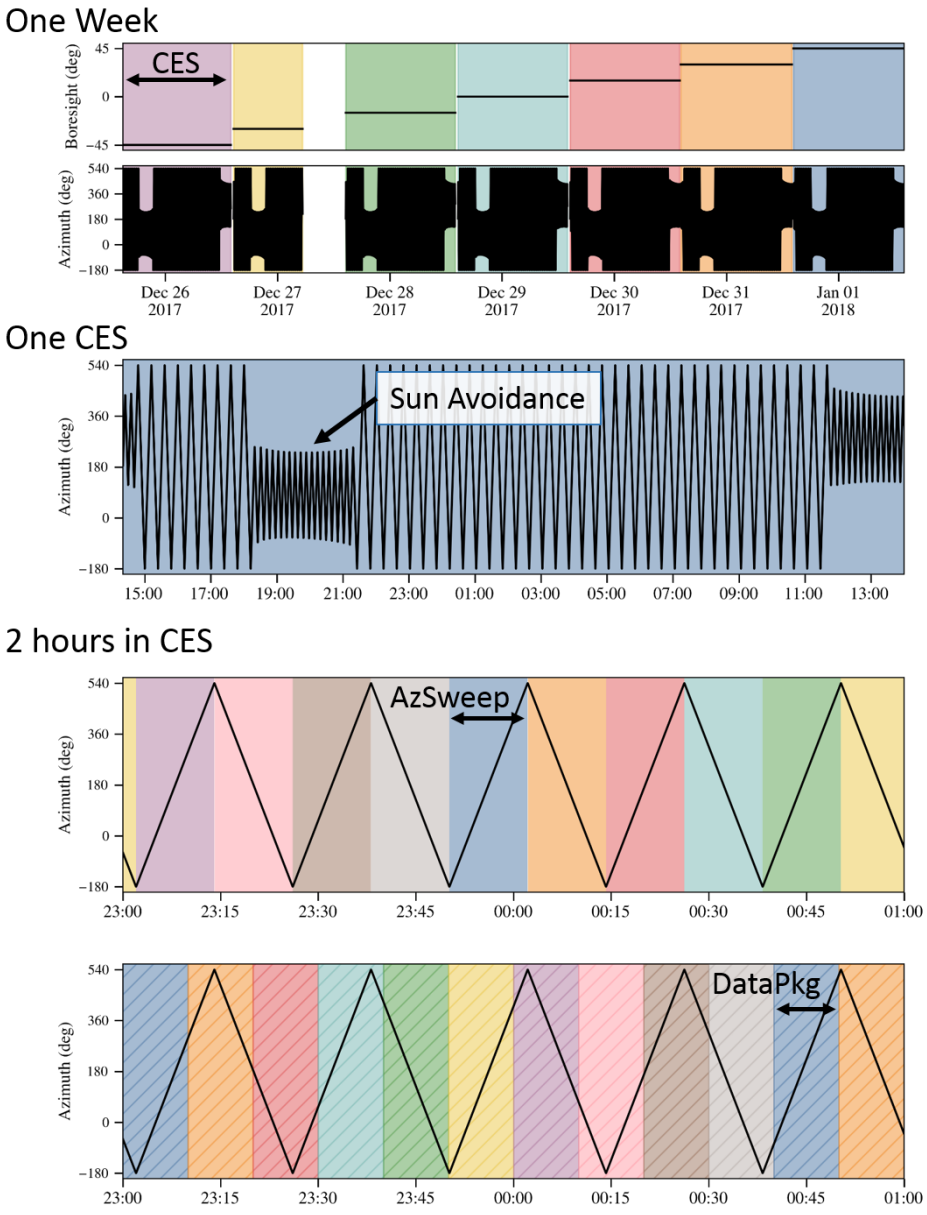

Figure 6.4: A summary of how data is divided within the `AzSweep` database. The top plot shows a week of observations divided into constant elevation scans (`CES`) at a single boresight. The second from the top plot shows the position of the azimuth axis for a single $\sim$ 24 hour `CES` scan including times when sun avoidance is active. The second from the bottom plot has a zoom-in of 2 hours of observations and the colored backgrounds denote difference `AzSweeps`, times when the mount is moving in a single direction. The bottom plot shows the same time range but the colored background denote the data package delineations for the same time period.

Cut	Description	Options
Observation State	Cut based on the reported observation state of the mount	All, CMB, Drift
Data Valid	Cut based on the reported data valid flag from the MCE	
Constant Detectors	Cut detectors that are constant (off)	
Unlocked Detectors	Divides data into N segments and cuts detectors for a segment where they cover the entire range of the DAC[a]	$N = 20$
VPM On	Cuts all detectors for time periods where the VPM was off	
Moon Distance	Cuts detectors when they are within θ_{min} of the moon	$\theta_{\text{min}} = 5^\circ$
Running Variance	Calculates a probability distribution, P_v, of the variance of the data over N periods of the VPM. Builds cuts on the data where the variance is above a level, Δ, set by a percentile threshold in the probability distribution.	$N = 1, 3, 20$, $\Delta = 3(P_v > 68\%)$

Table 6.1: The set of default cuts currently implemented by the CLASS analysis pipeline. If the data is not flagged by any of these metrics and valid VPM time constants (see section 6.2) can be found, the data is considered good.

[a] The signal measured by the MCE is the feedback required to keep the SQUID readout in the linear regime, this is a signal fed into a Digital-to-Analog Converter, hence DAC counts really are the basic unit of MCE data

time required for the initial loading and filtering of the data once it has been completed the first time. In addition, the software is modular and easily adaptable to add or subtract data products as our understanding of the time ordered data increases.

The majority of these data products are a standard set of cuts applied to the detectors. This set, listed in table 6.1, is fairly successful at flagging periods of bad data from the detectors. As the analysis pipeline for the CLASS telescopes develops, this suite of standard cuts and flags will likely be expanded and optimized.

6.2 Detector Time Constants

As discussed in section 5.4, the response time of the detectors creates phase shifts in the time ordered data with respect to the VPM position. The optical time constants associated with a single-pole low-pass filter used to model the detector response, must be calculated for every observation and then deconvolved from the data to align the VPM grid mirror positions with the time ordered data.

6.2.1 Calculating Time Constants

The anomalous VPM synchronous signal (AVSS) is the power observed by the detectors that is synchronous with the VPM but not caused by polarization on the sky. Some of the sources of the AVSS were outlined in chapter 5. The presence of the AVSS is used to calculate the optical detector time constants for each observation. The top plot in figure 6.5 shows example detector data on the same axis as the VPM position. This data has already had the MCE Butterworth low-pass filter deconvolved. The bottom left plot in figure 6.5 shows the same data when it is split into segments of positive and negative VPM velocity and binned with respect to the VPM position.

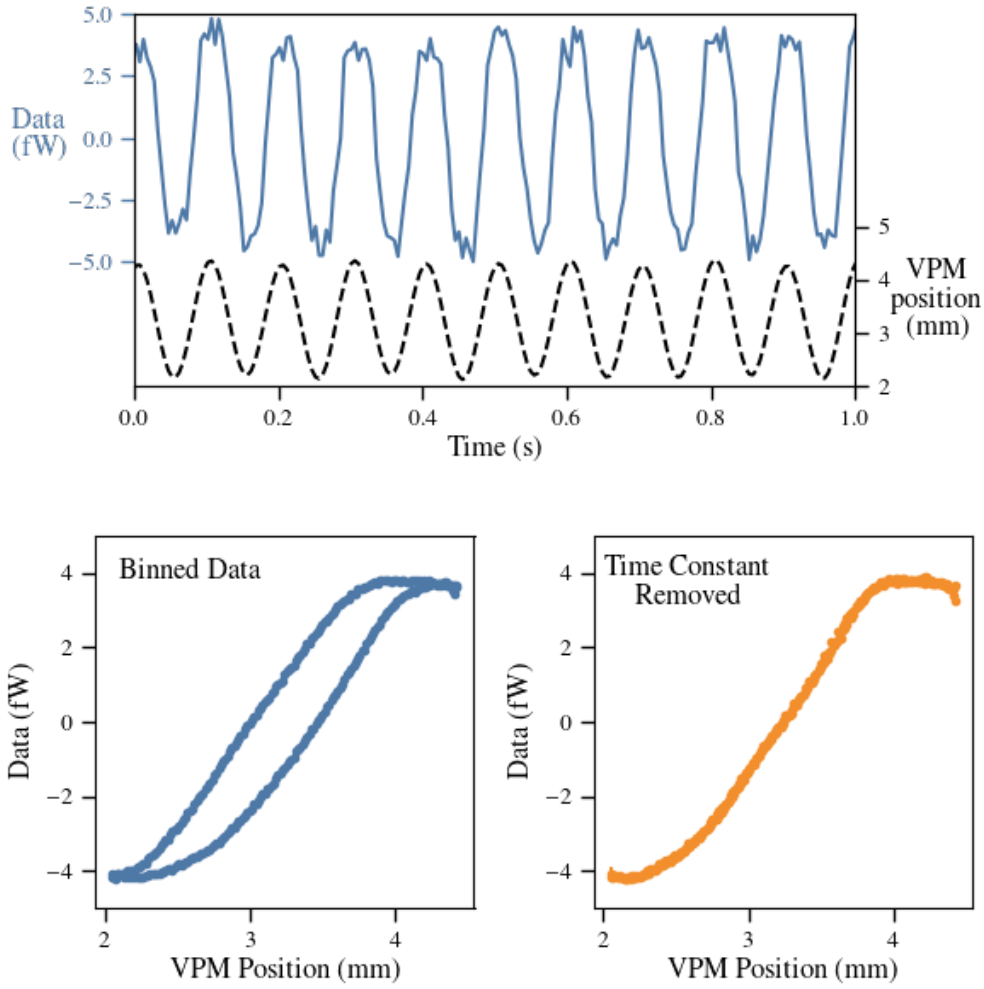

Figure 6.5: Top: An example timestream of data that has been de-butterworthed and high-passed plotted with the VPM position from the same time. The data shows the AVSS, which synchronous with the VPM and present in all CLASS data. Bottom Left: The same data when it has been split into segments of positive and negative VPM velocity and binned in grid-mirror distance. The hysteresis is an effect of the detector response time. Bottom Right: the same data and binning procedure as the bottom left plot, but after a single-pole low-pass filter with $\tau \sim 4$ ms has been deconvolved from the data. This shows an example of how a detector time constant can be fit and removed from the CLASS data.

This plot shows a distinct hysteresis effect, where the finite response time of the detector has caused a phase shift in time ordered data.

Since there is nothing in the theoretical VPM signal that should depend on the velocity of the VPM, we use the presence of hysteresis with respect to the VPM position to fit for and remove the time constants. The data is first pre-processed using the pipeline described in figure 6.1, so any jumps or discontinuities have been fixed and the data has been calibrated, de-Butterworthed, and high-passed. A χ^2 minimization routine deconvolves various single-pole low-pass filters, defined as

$$\mathcal{F}_\tau = \frac{1}{1 + 2i\pi\nu\tau}, \tag{6.1}$$

from the data which is then binned into positions across the VPM throw, and the level of residual hysteresis after time constant removal is calculated as

$$\chi^2 = \sum_{i=0}^{N_{\text{bins}}} \frac{(d_{+,i} - d_{-,i})^2}{\sigma_{+,i}^2 + \sigma_{-,i}^2}. \tag{6.2}$$

In this equation $d_{\pm,i}$ is the mean value of a particular grid-mirror distance bin when the VPM is moving forward $(+)$ or backward $(-)$. This minimization routine can be run on sections of data of varying length, however, the shorter the section the less accurate the fit, and the longer the section the longer the routine takes to run.

Figure 6.6 shows how the time interval of the time constant fit affects the resulting values. For this plot, sections of data ranging in length from 10 s to 1 hour were fit for time constant values across a night. The smaller intervals of 10 s and 30 s show significant scatter in successive measurements; this scatter is too large to be physical and indicates there is insufficient data to extract a time constant. The intervals of 1 min, 5 min, and 10 min coalesce into trend line that is a good description of how the detector time constants are changing with time. The 1 hour intervals do calculate

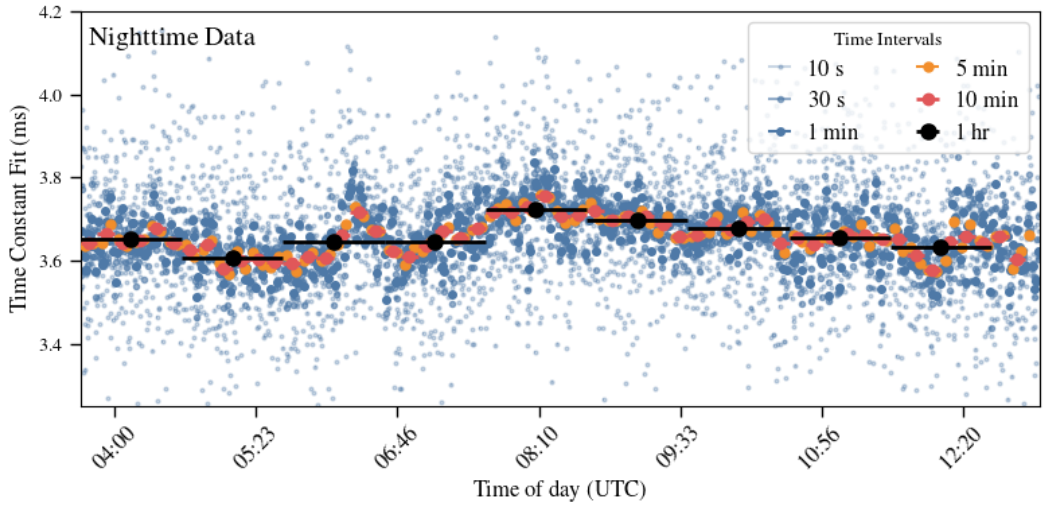

Figure 6.6: The time constants measured from a set of data using a variety of time intervals for the measurements. The smaller intervals, using less data, show significant scatter around the values measured for the longer intervals. Data is from the night of August 1st 2017.

time constant values along the tend observed in the shorter intervals, however, the longer intervals are too long to extract some of the shorter lived features. Further experimentation resulted in the understanding that intervals $\sim$ 3 min long resulted in time constant fits that had low scatter between successive measurements while also extracting features and variations of the data that appeared to be real.

While 3 minute time constant intervals were found to more completely capture the variation of the detector time constants, the structure of the 10 minute data packaging system and the database built off it motivated calculating time constants at 10 minute intervals as well. These 10 minute time constants are the mean value during that interval and can be imported into the database structure to enable analysis of time constants with respect to other observation parameters.

Figure 6.7 shows the distribution of time constants throughout the Q-band focal plane for the first era of observing. Some detectors show significantly more scatter

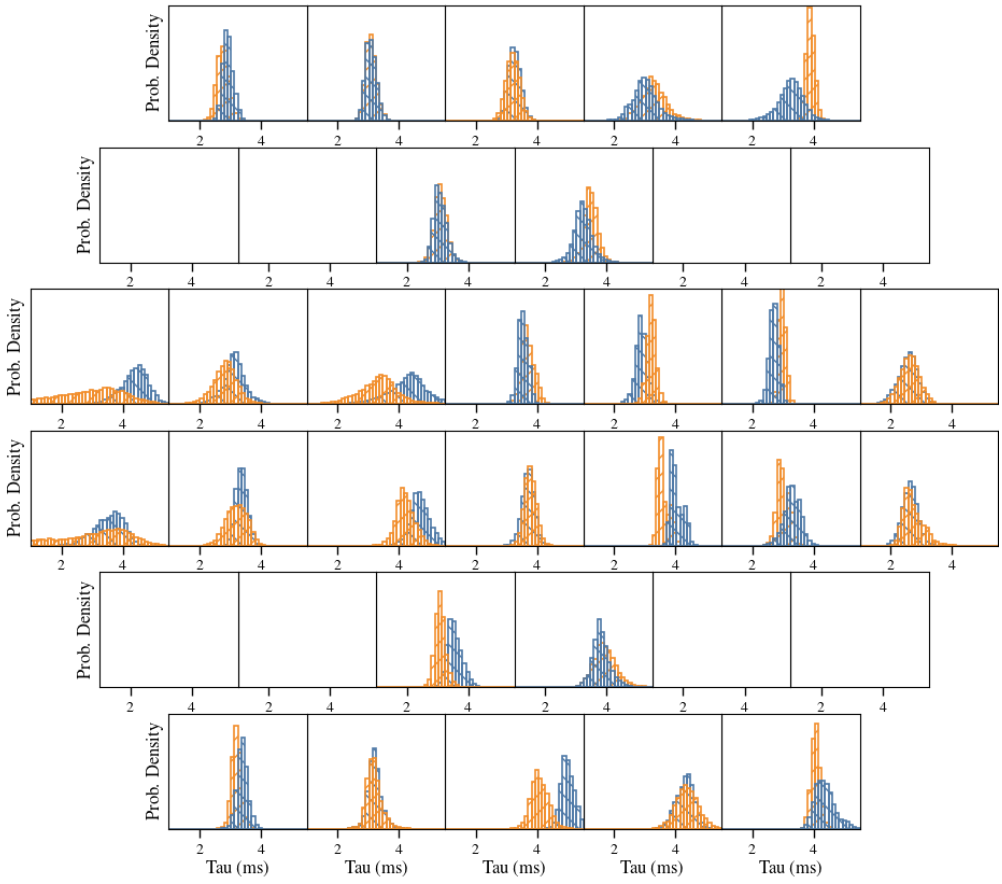

Figure 6.7: The distribution of time constants measured for each detector and each 10 min data package for the Q-band telescope over Era 1. While the median values for all detectors are between 2 and 5 ms, some detectors show significantly more scatter than other detectors.

than others, likely depending on various detector and readout parameters such as the detector loading, stability in the electro-thermal feedback within the detectors, and the overall noise level in the detector data.

Some selected detector time constants are shown in figure 6.8 plotted with respect to the time of day, air temperature, and boresight position. The discontinuities in time of day around 13:00 UTC are a result of that time usually marking the daily boresight rotations but the overnight peaks between ∼01:00 and 05:00 are unexplained. The positive trend with air temperature could be a result of loading variation on the detectors or a temperature effect within the electronics controlling and reading out the detectors. The optical time constant of the detectors depends on the electro-thermal feedback holding them on transition, so variations in the performance of the biasing electronics with temperature could change the detector time constants. The boresight dependent trends are different for every detector pair and could be a result of boresight changes rotating the elevation of the detectors and altering the atmospheric loading.

One of the current analysis efforts is determining the optimum method of deconvoling the effect of the detector time constants from the CLASS data. We have found that these time constants vary on times scales on the order of $\sim$ 3 minutes and correcting for these time constants is necessary to extract the correct Stokes parameters from the sky. A changing time constant as the telescope scans could produces a bias on the measured Stokes parameters on the larger angular scales. Ongoing analysis work will be examining how precisely the time constants must be determined and to determine methods of removing changing time constants from the detector data.

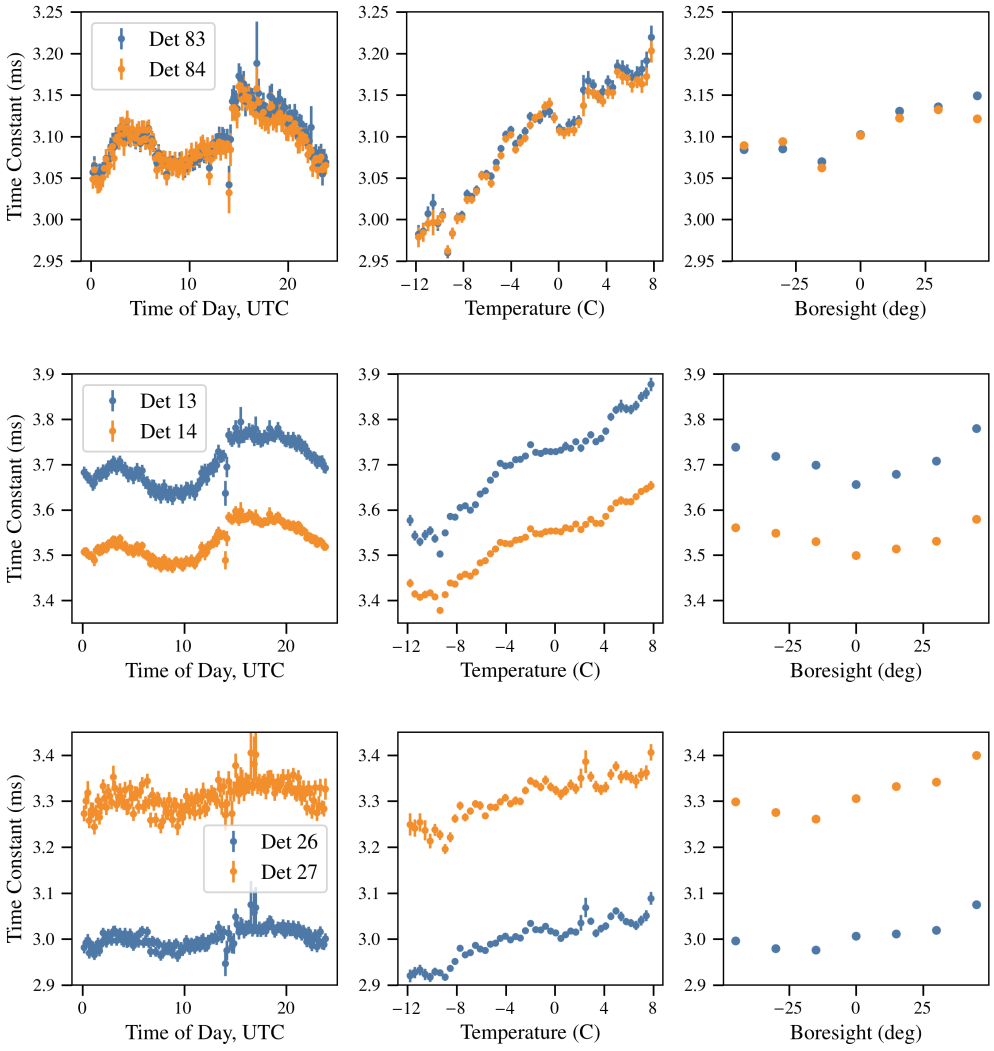

Figure 6.8: Detector time constants from the data package database binned with respect to time of day, temperature, and boresight position. Each row shows a pair of detectors at different elevation offsets within the Q-band focal plane, 83 and 84 have the highest elevation offset and 26 and 27 have the lowest elevation offset of these three pairs. The discontinuities in time of day around 13:00 UTC are a result of that time usually marking the daily boresight rotations. The positive trend with air temperature could be a result of loading variation on the detectors or a temperature effect within the readout electronics. The boresight dependent trends are different for every detector pair.

6.3 AVSS Templates

Following along the analysis pipeline in figure 6.1, once the detector time constants have been calculated and deconvolved it is possible to bin the AVSS just as a function of grid-mirror distance. As with the time constants, there is a broad range of time intervals were this can be done, but the results here are shown for the 10 minute sections of data that coincide with the data package database.

Figure 6.9 shows the templates calculated as the weighted mean of every AVSS measurement from the first 6 months of data in era one. These templates contain a variety of interesting features, neither the shape nor the amplitude directly match the predicted AVSS shapes from figures 5.17 and 5.18. The predicted amplitude of ~ 50 mK is about a factor of two smaller than the measured amplitudes of ~ 110 mK, and reasonable changes to the material parameters in the AVSS model cannot account for this discrepancy. The shapes are also much smoother than the square-wave-like shapes shown in chapter 5. The smoothing added by accounting for the detector readout is insufficient to match the shapes here, and the other understood method of broadening, increasing the detector bandpass, would require bandpass changes that are much larger than the constraints from independent bandpass measurements.

One of the features that does match the predicted AVSS is the left-right variation across the focal plane, the amplitudes for one detector sign are larger on one side of the focal plane and decrease toward the opposite side. This change reflects the projection of the detector electric fields onto the VPM wires and indicates at least a portion of the AVSS sources depend on this effect. There are ongoing efforts to expand the VPM modeling to include more realistic effects such as grid-mirror tilts and large angle of incidence spill from the VPM as an attempt to understand the

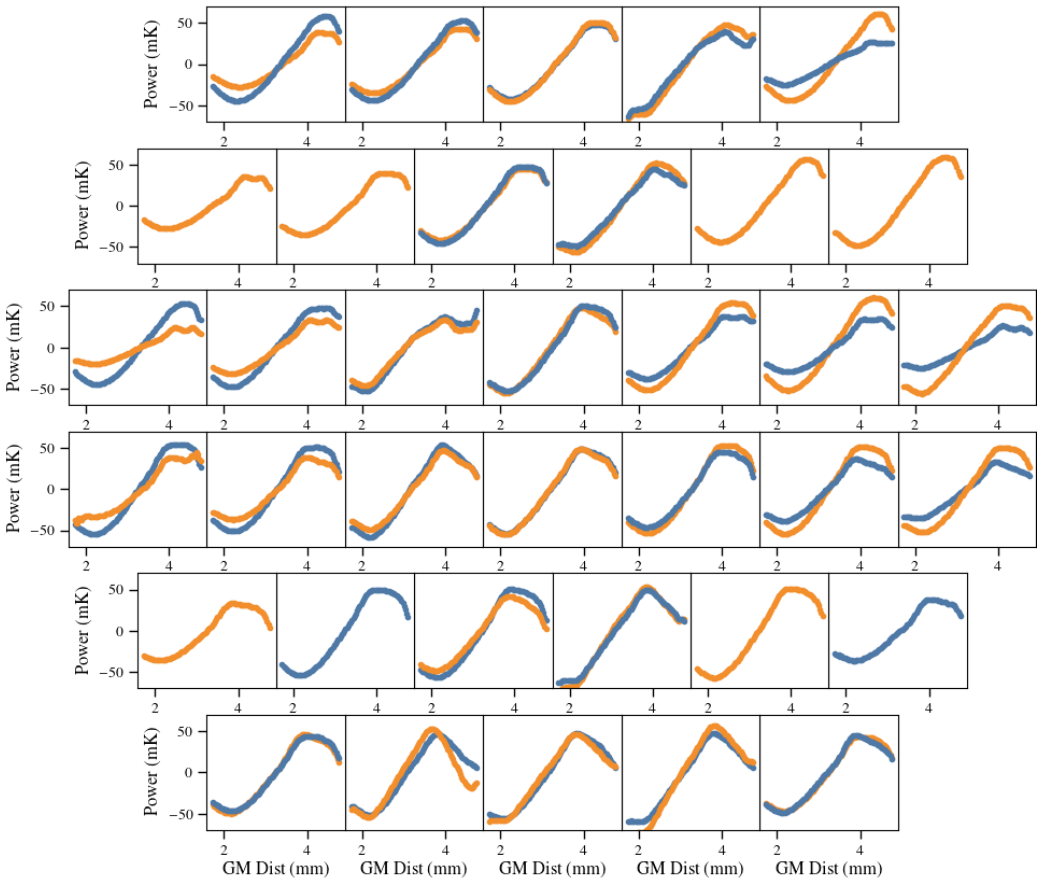

Figure 6.9: The templates of the AVSS for each detector in the Q-band focal plane. These templates were created using the combined measured templates for the first 6 months of data during era 1. These templates have a different shape than those predicted in figure 5.18, even when accounting for the effect of the detector time constant. However, they are extremely stable and one of the best measures available for determining the status of detector data. The blues lines are for detectors with $\alpha = +45°$ and the orange lines are for detectors with $\alpha = -45°$

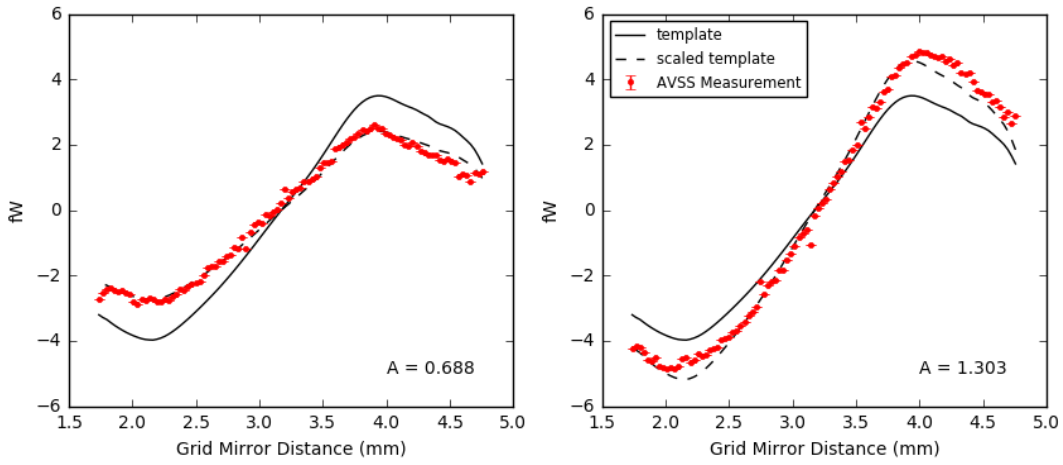

Figure 6.10: Two examples of fitting individual AVSS measurements to the templates for the AVSS. The red points are the measured AVSS for two different data packages and the dashed line is the AVSS template scaled by the amplitude value fit from that data. The AVSS amplitudes are input into the data package database to be correlated with other observables.

additional sources of AVSS in the data.

Although the exact shape and amplitude of the AVSS is not completely understood, it is possible to look for correlations in the AVSS with other observation parameters such as the temperature of the VPM. If the majority of the AVSS came from emission from the VPM, it would scale with VPM temperature. To look for this scaling, each 10 minute AVSS measurement is fit to the AVSS templates in figure 6.9 to obtain a relative amplitude for that 10 minutes. Figure 6.10 shows two examples of these fits. The red data points are the AVSS measurements for two data packages, the solid black line is the template for that detector and the dashed line is that template scaled by an amplitude values. These amplitude values are a way of reducing the AVSS measurements into a single number that can be correlated with other observables.

Figure 6.11 shows the amplitude value for the AVSS binned with time of day, temperature, and boresight for the same detectors as shown for the time constants in figure 6.8. The changes in the AVSS amplitudes are much more dramatic than for the

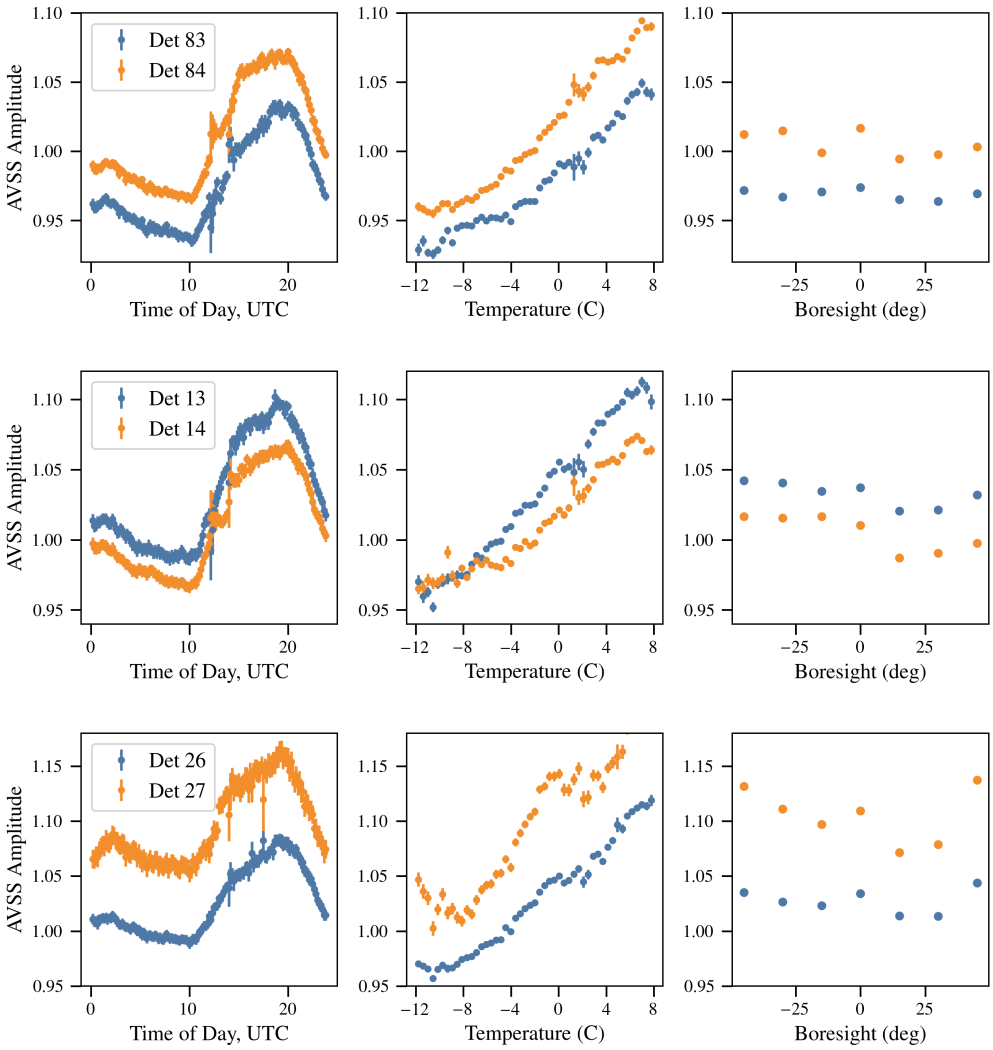

Figure 6.11: The AVSS amplitudes binned with time of day, air temperature, and boresight angle for three pairs of detectors in the focal plane of the Q-band telescope. Each row shows a pair of detectors at different elevation offsets within the Q-band focal plane, 83 and 84 have the highest elevation offset, and 26 and 27 have the lowest elevation offset of these three pairs. The variation in the AVSS amplitude with temperature is also reflected in the changes based on the time of day. The boresight variations are small and have different shapes for each detector.

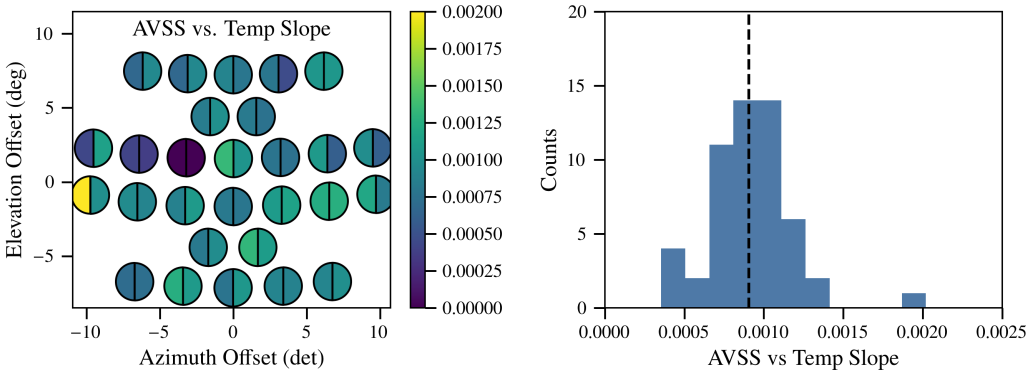

Figure 6.12: Left: The fitted slope to the amplitude of the AVSS as a function of air temperature across the focal plane. This fit gives a type of effective emissivity of the VPM which can be compared to the VPM theoretical model. Right: A histogram of the effective emissivity measurements which have a median value at 0.00966 amp/°C or about 0.0011 K/K, much lower than emissivities of metals in the microwave wavelengths.

time constants. The AVSS is expected to directly correlate with the temperature of the VPM and the middle column of plots show that air temperature is a good proxy for that measure.

The amplitude of the AVSS as a function of temperature was fit to a line to extract the effective emissivity of the VPM. The fits across the focal plane and the histogram of their values are in figure 6.12. The median effective emissivity is

$$\epsilon_{\mathrm{VPM}} = 0.0011\ \mathrm{K}/^{\circ}\mathrm{C}. \tag{6.3}$$

This effective emissivity cannot be directly compared to the emissivity of metals because the AVSS measurements only account for the change in power across the VPM throw and do not measure the absolute value of the emission. However, we can compare this emission to the predicted emission from the models developed in chapter 5. Simulating an identical measurement produces an effective emissivity of $\epsilon_{\mathrm{model}} = 0.0023\ \mathrm{K}/^{\circ}\mathrm{C}$, which is twice the level observed. The amplitude of the AVSS

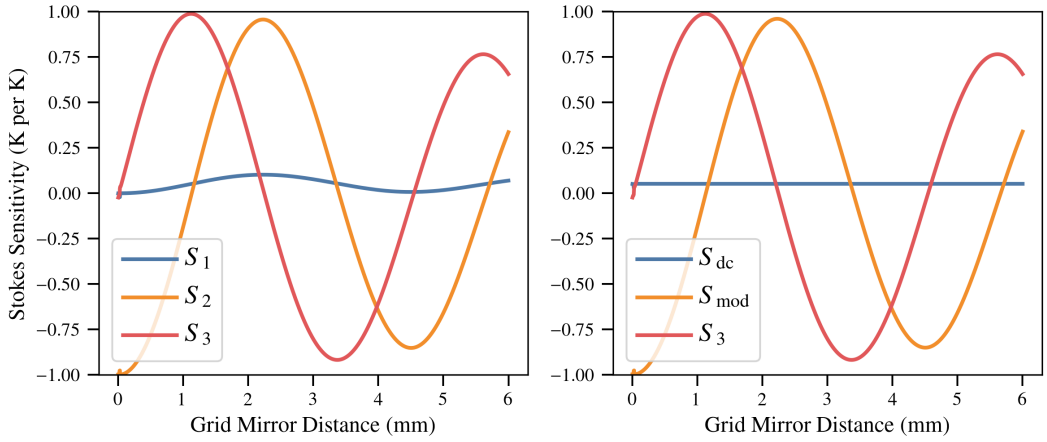

Figure 6.13: Left: The modulation functions, where S_x denotes sensitivity to Stokes Q, U, and V, respectively, for detector 81 in the corner of the Q-band focal plane. These functions illustrate the covariance in the modulation functions for Q and U when they are in the sky basis. Right: The modulation functions for detector 81 that have been rotated to orthogonalize the two linear polarizations, S_{mod} is the axis of maximum polarization modulation and S_{DC} is the orthogonal axis that has some residual but unmodulated polarization sensitivity.

is about twice what the model predicts but varies with temperature at half the level expected. This is incongruous with all of the AVSS resulting from emission or spill and requires further investigation. The measurement and prediction do not account for any changes with sky temperature, however, the sky temperature at Q-band is not expected to change by more than a few Kelvin. The combination of the AVSS amplitude being higher than predicted and its variation with temperature being lower than expected is not understood at this point.

6.4 Demodulation

Demodulation of data from the VPM is the mechanism for taking the detector timestreams and the VPM positions and extracting the modulated Stokes parameters as a function of time. There are several methods for accomplishing this demodulation, but first it requires accounting for the covariance within the modulation functions

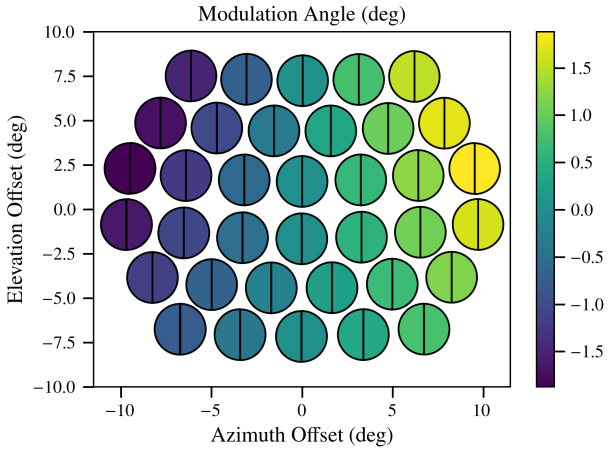

Figure 6.14: The angle ψ describing the necessary rotations to orthogonalize the modulation functions. This is the effective modulation angle with respect to the wire grid and acts like an addition rotation of the detector on the sky.

introduced in chapter 5. The left plot of figure 6.13 shows the modulation functions for a detector on the edge of the Q-band focal plane, with some of the largest azimuth and elevation offsets. S_1, S_2, and S_3 are the modulation functions for Stokes Q, U, and V, respectively, all in the basis of the detector on the sky. The modulation functions for Q and U are covariant and fitting for parameters with covariant functions produces covariant and unconstrained results. Instead, there must exist some angle ψ that can be used to rotate these functions to maximize the modulation for one axis and minimize the modulation for the other:

$$\begin{aligned} S_{\text{mod}} &= -S_1 \sin 2\psi + S_2 \cos 2\psi \\ S_{\text{DC}} &= S_1 \cos 2\psi + S_2 \sin 2\psi. \end{aligned} \tag{6.4}$$

This angle ψ is the angle the rotates the sky basis vectors into basis vectors aligned with the co-pol and cross-pol unit vectors defined with respect to the VPM wire grid (Ludwig, 1973). For the coordinate definitions set up in chapter 5, ψ can be calculated as

$$\tan\psi = \frac{-\sin(\Theta+el) + \tan(az)\tan(\Phi) - \sin(az)\tan(\Phi)\cos(\Theta+el) - \tan(az)\sin(az)\cot(\Theta+el)}{\tan(\Phi)\sin(\Theta+el) + \tan(az) - \sin(az)\cos(\Theta+el) + \tan(az)\sin(az)\tan(\Phi)\cot(\Theta+el)} \tag{6.5}$$

and figure 6.14 shows these angles plotted across the focal plane.

The rotation by ψ is like a rotation by an additional detector angle for the modulated axis, however, there is a residual unmodulated but non-zero sensitivity to the orthogonal axis which must be taken into account in calibration measurements or other points where the data is not high-passed.

To demodulate the detector data, a timestream of the modulation function is created using the measured VPM encoder positions $z(t)$. The modulation function timestream is then processed identically to the detector timestream, which generally requires some form of high-pass filter $\mathcal{F}_{\rm HP}$,

$$S^{\rm HP}_{\rm mod}(t) = \mathcal{F}_{\rm HP}\left[S_{\rm mod}[z(t)]\right]. \tag{6.6}$$

The demodulated timestream can then be calculated using the detector timestream $d(t)$ and a low-pass filter, $\mathcal{F}_{\rm LP}$, with frequency cutoff sufficiently below the modulation frequency of the VPM,

$$S_{\rm demod}(t) = \frac{\mathcal{F}_{\rm LP}\left[d(t) \times S^{\rm HP}_{\rm mod}(t)\right]}{\mathcal{F}_{\rm LP}\left[(S^{\rm HP}_{\rm mod}(t))^2\right]}. \tag{6.7}$$

Figure 6.15 shows an example of this process for an hour of CLASS data and a comparison pair differenced example that would be the method of calculating the polarization timestream if CLASS did not implement a modulator. The pair differenced data has had the VPM AVSS templates subtracted from it so the remaining signal is polarization measured by the subtraction of the two orthogonal detectors. The data is then low-pass filtered to match the filtering of the demodulated data. This data contains long time scale drifts and unmodulated temperature to polarization leakage that are indicative of the difficulties of mapping the largest angular scales

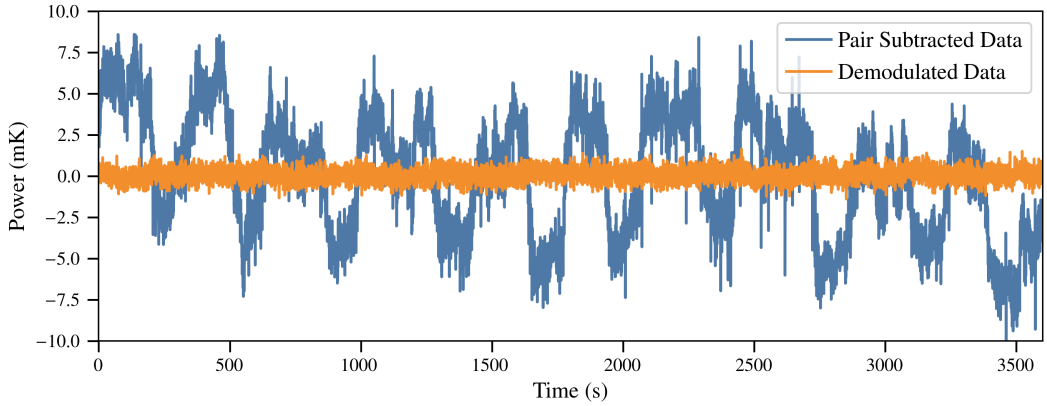

Figure 6.15: An example demodulated timestream compared to the pair differenced (AVSS subtracted) data from the same time. The pair differenced data is low-pass filtered in the same was as the demodulated data and imitates how to measure the polarization if CLASS did not implement a modulator. The pair differenced data shows significant long time scale variations and unmodulated temperature to polarization leakage. The demodulated data significantly reduces the long time scale drifts in the system and has no obvious trends or features.

on the sky. The demodulated data shows the same pair differenced data when it has been demodulated following the procedure outlined above. The white noise in the demodulated data is what CLASS would expect to see on these time scales; when observing the CMB polarization the signal is so faint all good data looks like, and primarily is, white noise.

Successfully demonstrating the demodulation of CLASS data and thus significantly reducing the level of $1/f$ noise and instrument temperature polarization is a critical step in validating the design of the CLASS instrument and the overall survey strategy along with the design and understanding of the VPMs. Future work will be continuing this effort; The analysis will be expanded to longer time scales and will more quantitatively evaluate the performance of the data CLASS will use to map of the largest angular scales of the CMB polarization. These polarization maps and their associated power spectra will make a nearly cosmic variance limited measurement

of the optical depth to reionization and detect or set limits on the amplitude of the inflationary gravitational waves in the early universe.

Appendices

Appendix A

Polarization

The polarization of light describes the direction of the electric field vector with respect to some set of basis vectors. To define all the relevant terms, start with a plane wave electric field traveling along the wavevector $\hat{k} = [0, 0, 1]$

$$\vec{E} = \left(E_x \hat{x} + E_y \hat{y}\right) e^{-jkz} \tag{A.1}$$

where here we are using $\hat{x}$ and $\hat{y}$ as basis vectors. E_x and E_y are any two complex scalars. The light will be *linearly polarized* if the complex phases of E_x and E_y are equal. Linear polarization can be horizontal or vertical when $E_y = 0$ or $E_x = 0$ and for other directions there is a polarization angle defined as the angle offset from the x axis, $\tan\alpha = E_y/E_x$. The polarization angle of linear polarization has 2-fold symmetry, where rotations around π have the same polarization. Light is called *circularly polarized* if the difference in the phases is exactly equal to $\pm\pi/2$. Left-handed and right-handed circular polarization are defined by the sign of the phase shift and the direction of propagation of the light. All other values for E_x and E_y are elliptically polarized, which can be viewed as a superposition of linear and circular polarization.

Since $\hat{x}$ and $\hat{y}$ are basis vectors for the polarization, we can use them to define a Jones vector $\vec{j} = [E_x, E_y]^T$ to describe the polarization state and Jones Matrices $\vec{j}_{out} = \boldsymbol{J} \cdot \vec{j}_{in}$ to describe the effects of polarization interacting with surfaces or materials. Table A.1 lists common Jones vectors and matrices. Jones vectors and matrices describe the electric field of single plane waves and are therefore an ideal method of tracking polarized light through a system where the relative phase change between the two linear polarizations is extremely important. The drawback is Jones matrices can only be used with light that is monochromatic and 100% polarized.

In most cases in astronomy, light is a bundle of many plane waves and the average of these plane waves is not 100% polarized. To describe the polarization properties of this light we need a way of statistically describing all the incoming plane waves. This is done using Stokes Parameters

$$\begin{aligned} I &= \langle E_x^* E_x \rangle + \langle E_y^* E_y \rangle \qquad & Q &= \langle E_x^* E_x \rangle - \langle E_y^* E_y \rangle \\ U &= \langle E_x E_y^* \rangle + \langle E_x^* E_y \rangle \qquad & V &= -i \left(\langle E_x E_y^* \rangle - \langle E_x^* E_y \rangle \right). \end{aligned} \tag{A.2}$$

The Stokes parameters can be combined into a vector $\vec{S} = [I, Q, U, V]$ which then allows us to define a Mueller Matrix analogously to Jones Matrices, $\vec{S}_{out} = M \cdot \vec{S}_{in}$. The Jones matrix for a single frequency plane wave can be directly converted into a Mueller matrix using

$$M = A(J \otimes J^*)A^{-1} \quad \text{with} \quad A = \begin{bmatrix} 1 & 0 & 0 & 1 \\ 1 & 0 & 0 & -1 \\ 0 & 1 & 1 & 0 \\ 0 & -i & i & 0 \end{bmatrix}. \tag{A.3}$$

Unlike Jones matrices, Mueller matrices and the associated Stokes vectors can be integrated over frequency or wavevector to obtain the average effects across a bandpass.

Polarization	Jones Vector	Stokes Vector
Horizontal	$\begin{pmatrix} 1 \\ 0 \end{pmatrix}$	$[1, 1, 0, 0]$
Vertical	$\begin{pmatrix} 0 \\ 1 \end{pmatrix}$	$[1, -1, 0, 0]$
$\pm 45^\circ$ Linear	$\frac{1}{\sqrt{2}} \begin{pmatrix} 1 \\ \pm 1 \end{pmatrix}$	$[1, 0, \pm 1, 0]$
Right/Left Circular	$\frac{1}{\sqrt{2}} \begin{pmatrix} 1 \\ \pm i \end{pmatrix}$	$[1, 0, 0, \pm 1]$

Optical Element[a]	Jones Matrix	Muller Matrix
Linear Polarizer ($\psi = 0^\circ$)	$\begin{bmatrix} 1 & 0 \\ 0 & 0 \end{bmatrix}$	$\frac{1}{2} \begin{bmatrix} 1 & 1 & 0 & 0 \\ 1 & 1 & 0 & 0 \\ 0 & 0 & 0 & 0 \\ 0 & 0 & 0 & 0 \end{bmatrix}$
Translation (ℓ)	$\begin{bmatrix} e^{ik\ell} & 0 \\ 0 & e^{ik\ell} \end{bmatrix}$	$\begin{bmatrix} 1 & 0 & 0 & 0 \\ 0 & 1 & 0 & 0 \\ 0 & 0 & 1 & 0 \\ 0 & 0 & 0 & 1 \end{bmatrix}$
Rotation (ψ)	$\begin{bmatrix} \cos\psi & \sin\psi \\ -\sin\psi & \cos\psi \end{bmatrix}$	$\begin{bmatrix} 1 & 0 & 0 & 0 \\ 0 & \cos 2\psi & \sin 2\psi & 0 \\ 0 & -\sin 2\psi & \cos 2\psi & 0 \\ 0 & 0 & 0 & 1 \end{bmatrix}$
Linear Retarder (ψ=0, δ)	$\begin{bmatrix} 1 & 0 \\ 0 & e^{i\delta} \end{bmatrix}$	$\begin{bmatrix} 1 & 0 & 0 & 0 \\ 0 & 1 & 0 & 0 \\ 0 & 0 & \cos\delta & -\sin\delta \\ 0 & 0 & \sin\delta & \cos\delta \end{bmatrix}$

Table A.1: The 2D polarization reference guide

[a] ψ is always the angle with respect to the x axis. δ is an induced phase shift between polarization parallel and perpendicular to linear polarization along ψ

Appendix B

Plane wave reflection

This appendix derives the results of a plane wave obliquely incident on some surface boundary and established the definition of various standard equations used in other parts of this thesis. The majority of these derivations and equations follow those laid out in (Pozar, 2012).

We start with a general plane wave, like that defined in table B.1, traveling along some wavevector $\vec{k}_i$ in some linear isotropic medium defined by ϵ_1 and μ_1, with $\sigma_1 = 0$ to prevent significant loss along the incident wavevector. The plane wave is incident on a boundary surface with normal $\hat{n}$ and positioned where $\hat{n} \cdot \vec{z}_0 = 0$. Beyond this boundary there is a second medium with ϵ_2, μ_2, and σ_2. This setup is shown in B.1. From conservation of energy, the plane wave at the boundary can be reflected, transmitted, or both. We define generic reflection and transmission coefficients where

$$\vec{E}_r = r\vec{E}_i \quad \text{and} \quad \vec{E}_t = t\vec{E}_i. \tag{B.1}$$

From the boundary conditions listed in table B.1, the tangential portion of the electric fields and the magnetic flux densities must be continuous across the surface. If we extract just the tangential portions of the electric fields at the surface boundary we

Maxwell's Equations	
$\nabla \cdot \vec{\mathcal{D}} = \rho$	$\nabla \times \vec{\mathcal{E}} = -\frac{\partial \vec{\mathcal{B}}}{\partial t}$
$\nabla \cdot \vec{\mathcal{B}} = 0$	$\nabla \times \vec{\mathcal{H}} = \vec{\mathcal{J}} + \frac{\partial \vec{\mathcal{D}}}{\partial t}$
Phasor Notation[a]	Wave Equation[b]
$\vec{\mathcal{E}}(t, \vec{x}) = \mathbb{R}\left(\vec{E}(\vec{x})\, e^{j\omega t}\right)$	$\nabla^2 \vec{E} + \omega^2 \mu \epsilon \vec{E} = 0$

Variable Definitions			
Electric Field	$\vec{\mathcal{E}}$	Magnetic Field	$\vec{\mathcal{H}}$
Electric Flux Density	$\vec{\mathcal{D}}$	Magnetic Flux Density	$\vec{\mathcal{B}}$
Electric Charge Density	ρ	Electric Current Density	$\vec{\mathcal{J}}$

Universal Constants	
Speed of Light	$c = 2.99 \times 10^8$ m/s
Permittivity of Free Space	$\epsilon_0 = 8.85 \times 10^{-12}$ F/m
Permeability of Free Space	$\mu_0 = 4\pi \times 10^7$ H/m

Material Properies			
Permittivity	ϵ	Dielectric Constant[c]	ϵ_r
Conductivity	σ	Loss Tangent	$\tan\delta$
Permeability	μ	Relative Permeability	μ_r
Magnetic Loss Tangent	$\tan\delta_\mu$		

For Linear Isotropic Media		
$\vec{D} = \epsilon \vec{E}$	$\vec{B} = \mu \vec{H}$	$\vec{J} = \sigma \vec{E}$
$\epsilon = \epsilon_0(\epsilon_r - j\tan\delta)$		$\mu = \mu_0(\mu_r - j\tan\delta_\mu)$

Boundary Conditions	
$\hat{n} \cdot (\vec{D}_2 - \vec{D}_1) = \rho_s$	$\hat{n} \cdot (\vec{B}_2 - \vec{B}_1) = 0$
$(\vec{E}_2 - \vec{E}_1) \times \hat{n} = 0$	$\hat{n} \times (\vec{H}_2 - \vec{H}_1) = \vec{J}_s$

General Plane Wave Solutions	
$\vec{E}(\vec{x}) = \vec{E}_0\, e^{-\vec{\gamma}\cdot\vec{x}}$	$\vec{H}(\vec{x}) = \hat{k} \times \vec{E}/\eta$
$\vec{k} \cdot \vec{E}_0 = 0$	$\sigma = 0 \rightarrow \gamma = jk = j\omega\sqrt{\mu\epsilon} \quad \hat{k} = \vec{k}/k$
$\eta = \sqrt{\mu/\epsilon}$	$\sigma \neq 0 \rightarrow \gamma = j\omega\sqrt{\mu\epsilon_0\epsilon_r}\sqrt{1 - j\frac{\sigma}{\omega\epsilon_0\epsilon_r}}$

Table B.1: A summary of standard definitions and equations used for electromagnetic plane waves. Derivations all in (Pozar, 2012)

[a] This is the engineering convention, the standard for most microwave applications
[b] In source free, linear, isotropic, and homogeneous media
[c] Also called Relative Permittivity

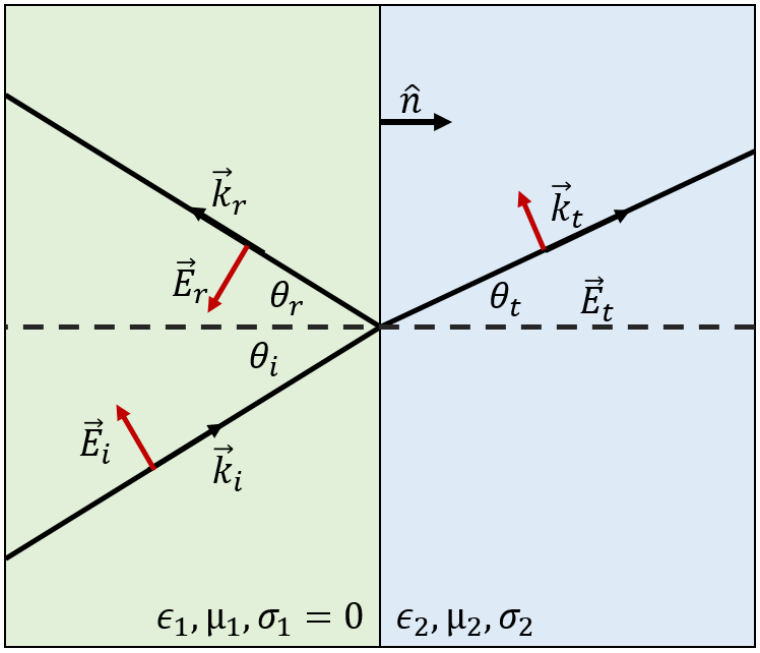

Figure B.1: The setup for a plane wave incident on some surface boundary, which is then reflected or transmitted.

get

$$\vec{E}_{i,\parallel}\, e^{-\vec{\gamma}_i \cdot \vec{z}_0} + \vec{E}_{r,\parallel}\, e^{-\vec{\gamma}_r \cdot \vec{z}_0} = \vec{E}_{t,\parallel}\, e^{-\vec{\gamma}_t \cdot \vec{z}_0}. \tag{B.2}$$

From the definition of a plane wave, none of the $\vec{E}_{x,\parallel}$s change along the boundary surface, so for equation B.2 to hold at all values along the boundary surface, the phases must always match:

$$\vec{\gamma}_i \cdot \vec{z}_0 = \vec{\gamma}_r \cdot \vec{z}_0 = \vec{\gamma}_t \cdot \vec{z}_0. \tag{B.3}$$

We can also define a *plane of incidence* as the plane made by $\vec{\gamma}_i$ and $\hat{n}$, $\vec{\gamma}_r$ and $\vec{\gamma}_t$ must also lie on this plane. The angles of incidence, reflection, and transmission are defined with $\cos\theta_x = |\vec{\gamma}_x \cdot \hat{n}|$. Adding these definitions into equation B.3 and noting that

$|\vec{\gamma}_i| = |\vec{\gamma}_r| = \gamma_1$ leads to the requirement that

$$\begin{aligned} \hat{k}_r &= \hat{k}_i - 2(\hat{k}_i \cdot \hat{n})\hat{n} \\ \theta_i &= \theta_r \\ \gamma_1 \sin\theta_i &= \gamma_2 \sin\theta_t. \end{aligned} \tag{B.4}$$

This is a way of writing Snell's law.

Since the continuity of electric and magnetic fields across the boundary surface depends on the direction of the field at the surface, it is standard practice to decompose the electric fields into modes that are perpendicular to the plane of incidence (the transverse electric field modes or TE modes) and parallel to the plane of incidence (the transverse magnetic field modes or TM modes). Both these modes must be perpendicular to the wavevector of the total electric field. Mathematically these modes can be described by the basis vectors

$$\hat{e}_{TE} = \frac{\hat{k} \times \hat{n}}{|\hat{k} \times \hat{n}|} \quad \text{and} \quad \hat{e}_{TM} = \hat{k} \times \hat{e}_{TE} = \frac{\hat{k}(\hat{k} \cdot \hat{n}) - \hat{n}}{|\hat{k} \times \hat{n}|} \quad \text{with} \quad |\hat{k} \cdot \hat{n}| = \cos\theta. \tag{B.5}$$

Since the associated magnetic fields are the cross products of the electric fields with the wavevectors, there are an analogous set of basis vectors, $\hat{h}_{TE} = \hat{e}_{TM}$ and $\hat{h}_{TM} = -\hat{e}_{TE}$. The reflection and transmission across a boundary depends on if the plane wave is a TE or TM mode, so we will define reflection coefficients in terms of these basis vectors.

$$\begin{aligned} \vec{E}_i \cdot \hat{e}_{TE} &= r_{TE} \left(\vec{E}_r \cdot \hat{e}_{TE} \right) \\ \vec{E}_i \cdot \hat{e}_{TM} &= r_{TM} \left(\vec{E}_r \cdot \hat{e}_{TM} \right). \end{aligned} \tag{B.6}$$

To get away from all the vector math now, we will define $\hat{n} = [0, 0, 1]$, $\vec{z}_0 = [x, y, 0]$

and $\hat{k}_i = [\sin\theta_i, 0, \cos\theta_i]$ as any other orientation could be rotated into this one. Substituting into equation B.5 gives us:

	$\hat{k}$	$\hat{e}_{TE}$	$\hat{e}_{TM}$
Incident	$[\sin\theta_i, 0, \cos\theta_i]$	$[0, -1, 0]$	$[\cos\theta_i, 0, -\sin\theta_i]$
Transmitted	$[\sin\theta_t, 0, \cos\theta_t]$	$[0, -1, 0]$	$[\cos\theta_t, 0, -\sin\theta_t]$

The reflection and transmission coefficients for the TE mode of the plane wave are calculated by requiring the continuity of the electric and magnetic fields across the boundary. We assume the phase matching criteria and Snell's law (equation B.4) holds in all cases so only the amplitudes of the fields must be matched.

$$\begin{aligned} \frac{\vec{E}_{TE,1}}{E_{TE,i}} &= \hat{e}_{TE,i} + r_{TE}\ \hat{e}_{TE,i} = -\hat{y} - r_{TE}\ \hat{y} \\ \frac{\vec{E}_{TE,2}}{E_{TE,i}} &= t_{TE}\ \hat{e}_{TE,t} = -\hat{y}\ t_{TE} \end{aligned} \tag{B.7}$$

and

$$\begin{aligned} \frac{\vec{H}_{TE,1}}{H_{TE,i}} &= \frac{\hat{h}_{TE,i}}{\eta_1} + r_{TE}\ \frac{\hat{h}_{TE,r}}{\eta_1} = \frac{\hat{x}\cos\theta_i - \hat{z}\sin\theta_i}{\eta_1} + r_{TE}\ \frac{-\hat{x}\cos\theta_i - \hat{z}\sin\theta_i}{\eta_1} \\ \frac{\vec{H}_{TE,2}}{H_{TE,i}} &= t_{TE}\ \frac{\hat{h}_{TE,t}}{\eta_2} = t_{TE}\ \frac{\hat{x}\cos\theta_t - \hat{z}\sin\theta_t}{\eta_2} \end{aligned} \tag{B.8}$$

Setting $E_{TE,1,y} = E_{TE,2,y}$ and $H_{TE,1,x} = H_{TE,2,x}$ and solving for r_{TE} and t_{TE} results in

$$\begin{aligned} r_{TE} &= \frac{\eta_2\cos\theta_i - \eta_1\cos\theta_t}{\eta_1\cos\theta_t + \eta_2\cos\theta_i} \\ t_{TE} &= \frac{2\eta_2\cos\theta_i}{\eta_1\cos\theta_t + \eta_2\cos\theta_i} \end{aligned} \tag{B.9}$$

An analogous method is used to solve for the reflection and transmission coefficients of the TM modes, which results in

$$r_{TM} = \frac{\eta_2 \cos\theta_t - \eta_1 \cos\theta_i}{\eta_1 \cos\theta_i + \eta_2 \cos\theta_t}$$
$$t_{TM} = \frac{2\eta_2 \cos\theta_i}{\eta_1 \cos\theta_i + \eta_2 \cos\theta_t}. \tag{B.10}$$

Equations B.9 and B.10 are the Fresnel Equations for describing the reflection and transmission of light at the interface between two different optical media.

B.1 Special Case: Oblique Incidence on a Conductor

This is basically an electric field incident on a flat mirror made of a real material. For a conductor with $\sigma >> \omega\epsilon$, the propagation constant in material 2 (γ_2) is $(1+j)\sqrt{\omega\mu\sigma/2}$ which makes the effective impedance of the material $\eta_2 = (1+j)\sqrt{\omega\mu/2\sigma}$. Using these definitions, the electric field in material 2 is

$$\vec{E}_2 = \vec{E}_t \exp\left(\left(\hat{k}_t \cdot \hat{x}_n\right)(1+j)\sqrt{\frac{\omega\mu\sigma}{2}}\right). \tag{B.11}$$

phase matching $\vec{E}_2$ to $\vec{E}_1$ requires

$$k_1 \sin\theta_i = \sin\theta_t (1+j)\sqrt{\frac{\omega\mu\sigma}{2}} \tag{B.12}$$

where for typical values for conductors in the microwave, $\sigma >> k_1$ and $\theta_t \to 0$. Substituting this into equations B.9 and B.10 results in[1]

$$r_{TE} = \frac{\eta_2 \cos\theta_i - \eta_1}{\eta_2 \cos\theta_i + \eta_1} \quad \text{and} \quad r_{TM} = \frac{\eta_2 - \eta_1 \cos\theta_i}{\eta_1 \cos\theta_i + \eta_2}. \tag{B.13}$$

For perfect conductors, $\eta_2 \to 0$ and $r_{TE} = -1$ and $r_{TM} = -1$.

[1] While the values for t_{TE} and t_{TM} are also nonzero in this setup, the large real part in the propagation coefficient causes these fields to decay quite quickly.

Appendix C

ABCD and Scattering Matrices

The transmission or reflection of a wave at a single junction of boundary is usually straightforward to solve using the methods described in appendix B, however, with each successive material the phase matching criteria becomes more complicated. For problems with many layers of dielectrics (ie. AR coated plastics) or many polarization selective surfaces (ie. the VPM) it is often easier to abstract the problem into a transmission line analysis that makes use of the analogy between $\vec{H} = \hat{k} \times \vec{E}/\eta$ and $I = V/Z$. With electric fields we have to deal with polarization, so the analogy requires an additional split with $H_{TM} = E_{TM}/\eta_{TM}$ and $H_{TE} = E_{TE}/\eta_{TE}$, but this lets us use transmission line analysis for optical problems.

Figure C.1 shows a standard two-port network where electric fields (voltages) are entering and leaving some "black box," representing a type of material or surface. Figure C.1 also defines the two types of matrices used to represent two port networks, $ABCD$ matrices and scattering matrices. $ABCD$ matrices are extremely useful because they encode the fields on both sides of the port and make it easy to stack many layers of material in sequence. Scattering matrices are easy to expand to N ports in a junction and also have a more straightforward interpretation where $S_{00} = r$ and $S_{01} = t$ for

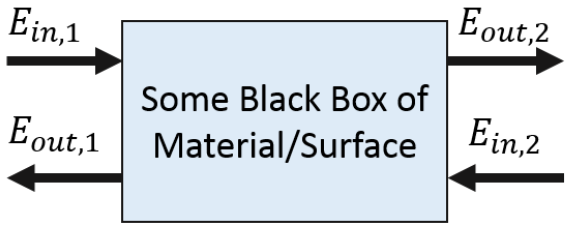

$$E_1 = E_{in,1} + E_{out,1} \qquad E_2 = E_{in,2} + E_{out,2}$$

ABCD Matrix

$$\begin{bmatrix} E_1 \\ H_1 \end{bmatrix} = \begin{bmatrix} A & B \\ C & D \end{bmatrix} \begin{bmatrix} E_2 \\ H_2 \end{bmatrix}$$

Scattering Matrix

$$\begin{bmatrix} E_{out,1} \\ E_{out,2} \end{bmatrix} = \begin{bmatrix} S_{00} & S_{01} \\ S_{10} & S_{11} \end{bmatrix} \begin{bmatrix} E_{in,1} \\ E_{in,2} \end{bmatrix}$$

Figure C.1: An illustration of a two port network and the definitions for how ABCD matrices and scattering are used to define that network.

Circuit	ABCD Parameters	
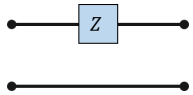	$A = 1$	$B = Z$
	$C = 0$	$D = 1$
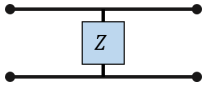	$A = 1$	$B = 0$
	$C = \frac{1}{Z}$	$D = 1$
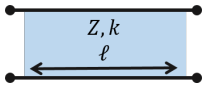	$A = \cos k\ell$	$B = jZ \sin k\ell$
	$C = \frac{j}{Z} \sin k\ell$	$D = \cos k\ell$
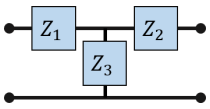	$A = 1 + \frac{Z_1}{Z_3}$	$B = Z_1 + Z_2 + \frac{Z_1 Z_2}{Z_3}$
	$C = \frac{1}{Z_3}$	$D = 1 + \frac{Z_2}{Z_3}$
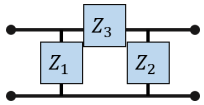	$A = 1 + \frac{Z_3}{Z_2}$	$B = Z_3$
	$C = \frac{1}{Z_1} + \frac{1}{Z_2} + \frac{Z_3}{Z_1 Z_2}$	$D = 1 + \frac{Z_3}{Z_1}$

Table C.1: Typical two-port junctions encountered in transmission line analysis and their associated ABCD matrix parameters. From (Pozar, 2012)

an incident field from side one. For two-port networks it is also straightforward to convert from an $ABCD$ matrix implementation to a scattering matrix implementation. For any $ABCD$ matrix, the S_{00} and S_{01} parameters are

$$\begin{aligned} S_{00} &= r_{mode} = \frac{A + B/\eta - \eta C - D}{A + B/\eta + \eta C + D} \\ S_{01} &= t_{mode} = \frac{2}{A + B/\eta + \eta C + D} \end{aligned} \tag{C.1}$$

Extensions to transmission line models for plane waves at oblique incidence are done by calculating solutions and then seeing how we have to change to make the transmission line solution match (Bronwell, 1944). This requires

$$\begin{aligned} \eta_{TM} &= \eta \cos\theta_i \\ \eta_{TE} &= \eta / \cos\theta_i \\ \lambda_{eff} &= \lambda / \cos\theta_i \end{aligned} \tag{C.2}$$

The wavelength change is analogous to having all distances increased by a factor of $\cos\theta_i$.

References

Abazajian, K. N., K. Arnold, J. Austermann, B. A. Benson, C. Bischoff, J. Bock, J. R. Bond, J. Borrill, I. Buder, D. L. Burke, E. Calabrese, J. E. Carlstrom, C. S. Carvalho, C. L. Chang, H. C. Chiang, S. Church, A. Cooray, T. M. Crawford, B. P. Crill, K. S. Dawson, S. Das, M. J. Devlin, M. Dobbs, S. Dodelson, O. Doré, J. Dunkley, J. L. Feng, A. Fraisse, J. Gallicchio, S. B. Giddings, D. Green, N. W. Halverson, S. Hanany, D. Hanson, S. R. Hildebrandt, A. Hincks, R. Hlozek, G. Holder, W. L. Holzapfel, K. Honscheid, G. Horowitz, W. Hu, J. Hubmayr, K. Irwin, M. Jackson, W. C. Jones, R. Kallosh, M. Kamionkowski, B. Keating, R. Keisler, W. Kinney, L. Knox, E. Komatsu, J. Kovac, C.-L. Kuo, A. Kusaka, C. Lawrence, A. T. Lee, E. Leitch, A. Linde, E. Linder, P. Lubin, J. Maldacena, E. Martinec, J. McMahon, A. Miller, V. Mukhanov, L. Newburgh, M. D. Niemack, H. Nguyen, H. T. Nguyen, L. Page, C. Pryke, C. L. Reichardt, J. E. Ruhl, N. Sehgal, U. Seljak, L. Senatore, J. Sievers, E. Silverstein, A. Slosar, K. M. Smith, D. Spergel, S. T. Staggs, A. Stark, R. Stompor, A. G. Vieregg, G. Wang, S. Watson, E. J. Wollack, W. L. K. Wu, K. W. Yoon, O. Zahn, and M. Zaldarriaga (2015). "Inflation physics from the cosmic microwave background and large scale structure". In: *Astroparticle Physics* 63, pp. 55–65. DOI: 10.1016/j.astropartphys.2014.05.013. arXiv: 1309.5381.

Albrecht, A. and P. J. Steinhardt (1982). "Cosmology for grand unified theories with radiatively induced symmetry breaking". In: *Physical Review Letters* 48, pp. 1220–1223. DOI: 10.1103/PhysRevLett.48.1220.

Allison, R., P. Caucal, E. Calabrese, J. Dunkley, and T. Louis (2015). "Towards a cosmological neutrino mass detection". In: Phys. Rev. D 92.12, 123535, p. 123535. DOI: 10.1103/PhysRevD.92.123535. arXiv: 1509.07471.

Appel, J. W., A. Ali, M. Amiri, D. Araujo, C. L. Bennet, F. Boone, M. Chan, H.-M. Cho, D. T. Chuss, F. Colazo, E. Crowe, K. Denis, R. Dünner, J. Eimer, T. Essinger-Hileman, D. Gothe, M. Halpern, K. Harrington, G. Hilton, G. F. Hinshaw, C. Huang, K. Irwin, G. Jones, J. Karakula, A. J. Kogut, D. Larson, M. Limon, L. Lowry, T. Marriage, N. Mehrle, A. D. Miller, N. Miller, S. H. Moseley, G. Novak, C. Reintsema, K. Rostem, T. Stevenson, D. Towner, K. U-Yen, E. Wagner, D. Watts, E. Wollack, Z. Xu, and L. Zeng (2014). "The cosmology large angular scale surveyor

(CLASS): 38-GHz detector array of bolometric polarimeters". In: *Millimeter, Submillimeter, and Far-Infrared Detectors and Instrumentation for Astronomy VII*. Vol. 9153. Proc. SPIE, 91531J. DOI: 10.1117/12.2056530. arXiv: 1408.4789 [astro-ph.IM].

Ata, M., F. Baumgarten, J. Bautista, F. Beutler, D. Bizyaev, M. R. Blanton, J. A. Blazek, A. S. Bolton, J. Brinkmann, J. R. Brownstein, E. Burtin, C.-H. Chuang, J. Comparat, K. S. Dawson, A. de la Macorra, W. Du, H. du Mas des Bourboux, D. J. Eisenstein, H. Gil-Marín, K. Grabowski, J. Guy, N. Hand, S. Ho, T. A. Hutchinson, M. M. Ivanov, F.-S. Kitaura, J.-P. Kneib, P. Laurent, J.-M. Le Goff, J. E. McEwen, E.-M. Mueller, A. D. Myers, J. A. Newman, N. Palanque-Delabrouille, K. Pan, I. Pâris, M. Pellejero-Ibanez, W. J. Percival, P. Petitjean, F. Prada, A. Prakash, S. A. Rodríguez-Torres, A. J. Ross, G. Rossi, R. Ruggeri, A. G. Sánchez, S. Satpathy, D. J. Schlegel, D. P. Schneider, H.-J. Seo, A. Slosar, A. Streblyanska, J. L. Tinker, R. Tojeiro, M. Vargas Magaña, M. Vivek, Y. Wang, C. Yèche, L. Yu, P. Zarrouk, C. Zhao, G.-B. Zhao, and F. Zhu (2018). "The clustering of the SDSS-IV extended Baryon Oscillation Spectroscopic Survey DR14 quasar sample: first measurement of baryon acoustic oscillations between redshift 0.8 and 2.2". In: MNRAS 473, pp. 4773–4794. DOI: 10.1093/mnras/stx2630. arXiv: 1705.06373.

Bal-tech (2018). *Flexural Encyclopedia*. URL: http://www.precisionballs.com/Flexural_Encyclopedia.php (visited on 05/08/2018).

Barkats, D., C. Bischoff, P. Farese, T. Gaier, J. O. Gundersen, M. M. Hedman, L. Hyatt, J. J. McMahon, D. Samtleben, S. T. Staggs, E. Stefanescu, K. Vanderlinde, and B. Winstein (2005). "Cosmic Microwave Background Polarimetry Using Correlation Receivers with the PIQUE and CAPMAP Experiments". In: ApJS 159, pp. 1–26. DOI: 10.1086/430208. eprint: astro-ph/0503329.

Bennett, C. L., D. Larson, J. L. Weiland, N. Jarosik, G. Hinshaw, N. Odegard, K. M. Smith, R. S. Hill, B. Gold, M. Halpern, E. Komatsu, M. R. Nolta, L. Page, D. N. Spergel, E. Wollack, J. Dunkley, A. Kogut, M. Limon, S. S. Meyer, G. S. Tucker, and E. L. Wright (2013). "Nine-year Wilkinson Microwave Anisotropy Probe (WMAP) Observations: Final Maps and Results". In: ApJS 208, 20, p. 20. DOI: 10.1088/0067-0049/208/2/20. arXiv: 1212.5225 [astro-ph.CO].

BICEP2/Keck Array Collaborations, P. A. R. Ade, Z. Ahmed, R. W. Aikin, K. D. Alexander, D. Barkats, S. J. Benton, C. A. Bischoff, J. J. Bock, R. Bowens-Rubin, J. A. Brevik, I. Buder, E. Bullock, V. Buza, J. Connors, B. P. Crill, L. Duband, C. Dvorkin, J. P. Filippini, S. Fliescher, J. Grayson, M. Halpern, S. Harrison, G. C. Hilton, H. Hui, K. D. Irwin, K. S. Karkare, E. Karpel, J. P. Kaufman, B. G. Keating, S. Kefeli, S. A. Kernasovskiy, J. M. Kovac, C. L. Kuo, E. M. Leitch, M. Lueker, K. G. Megerian, C. B. Netterfield, H. T. Nguyen, R. O'Brient, R. W. Ogburn, A. Orlando, C. Pryke, S. Richter, R. Schwarz, C. D. Sheehy, Z. K. Staniszewski, B. Steinbach, R. V. Sudiwala, G. P. Teply, K. L. Thompson, J. E. Tolan, C. Tucker, A. D. Turner, A. G. Vieregg, A. C. Weber, D. V. Wiebe, J. Willmert, C. L. Wong, W. L. K. Wu, and K. W. Yoon (2016). "Improved Constraints on Cosmology and Foregrounds from BICEP2 and

Keck Array Cosmic Microwave Background Data with Inclusion of 95 GHz Band". In: *Phys. Rev. Lett.* 116 (3), p. 031302. DOI: 10.1103/PhysRevLett.116.031302. URL: http://link.aps.org/doi/10.1103/PhysRevLett.116.031302.

Bronwell, A. (1944). "Transmission-Line Analogies of Plane Electromagnetic-Wave Reflections". In: *Proceedings of the IRE* 32.4, pp. 233–241. ISSN: 0096-8390. DOI: 10.1109/JRPROC.1944.230657.

Chuss, D. T., J. R. Eimer, D. J. Fixsen, J. Hinderks, A. J. Kogut, J. Lazear, P. Mirel, E. Switzer, G. M. Voellmer, and E. J. Wollack (2014). "Variable-delay polarization modulators for cryogenic millimeter-wave applications". In: *Review of Scientific Instruments* 85.6, 064501, p. 064501. DOI: 10.1063/1.4879499. arXiv: 1403.1652 [astro-ph.IM].

Chuss, D. T., E. J. Wollack, R. Henry, H. Hui, A. J. Juarez, M. Krejny, S. H. Moseley, and G. Novak (2012). "Properties of a variable-delay polarization modulator". In: Appl. Opt. 51, p. 197. DOI: 10.1364/AO.51.000197. arXiv: 1106.5984 [astro-ph.IM].

Clesse, S., L. Lopez-Honorez, C. Ringeval, H. Tashiro, and M. H. G. Tytgat (2012). "Background reionization history from omniscopes". In: Phys. Rev. D 86.12, 123506, p. 123506. DOI: 10.1103/PhysRevD.86.123506. arXiv: 1208.4277 [astro-ph.CO].

Committee for a Decadal Survey of Astronomy and Astrophysics, National Research Council (2010). *New Worlds, New Horizons in Astronomy and Astrophysics*. The National Academies Press. ISBN: 9780309157995. URL: http://www.nap.edu/openbook.php?record_id=12951.

Coughlin, K. P., J. J. McMahon, K. T. Crowley, B. J. Koopman, K. H. Miller, S. M. Simon, and E. J. Wollack (2018). "Pushing the Limits of Broadband and High-Frequency Metamaterial Silicon Antireflection Coatings". In: *Journal of Low Temperature Physics*. DOI: 10.1007/s10909-018-1955-7. arXiv: 1804.08368 [astro-ph.IM].

Crites, A. T., J. W. Henning, P. A. R. Ade, K. A. Aird, J. E. Austermann, J. A. Beall, A. N. Bender, B. A. Benson, L. E. Bleem, J. E. Carlstrom, C. L. Chang, H. C. Chiang, H.-M. Cho, R. Citron, T. M. Crawford, T. de Haan, M. A. Dobbs, W. Everett, J. Gallicchio, J. Gao, E. M. George, A. Gilbert, N. W. Halverson, D. Hanson, N. Harrington, G. C. Hilton, G. P. Holder, W. L. Holzapfel, S. Hoover, Z. Hou, J. D. Hrubes, N. Huang, J. Hubmayr, K. D. Irwin, R. Keisler, L. Knox, A. T. Lee, E. M. Leitch, D. Li, C. Liang, D. Luong-Van, J. J. McMahon, J. Mehl, S. S. Meyer, L. Mocanu, T. E. Montroy, T. Natoli, J. P. Nibarger, V. Novosad, S. Padin, C. Pryke, C. L. Reichardt, J. E. Ruhl, B. R. Saliwanchik, J. T. Sayre, K. K. Schaffer, G. Smecher, A. A. Stark, K. T. Story, C. Tucker, K. Vanderlinde, J. D. Vieira, G. Wang, N. Whitehorn, V. Yefremenko, and O. Zahn (2015). "Measurements of E-Mode Polarization and Temperature-E-Mode Correlation in the Cosmic Microwave Background from 100 Square Degrees of SPTpol Data". In: ApJ 805, 36, p. 36. DOI: 10.1088/0004-637X/805/1/36. arXiv: 1411.1042.

Dahal, S., A. Ali, J. W. Appel, T. Essinger-Hileman, C. L. Bennett, M. Brewer, R. Bustos, M. Chan, D. T. Chuss, J. Cleary, F. Colazo, J. Couto, K. Denis, R. Dünner, J. Eimer, T. Engelhoven, P. Fluxa, M. Halpern, K. Harrington, K. Helson, G. Hilton, G. F. Hinshaw, J. Hubmayr, J. Iuliano, J. Karakla, B. Marquez, T. Marriage, J. McMahon, N. T. Miller, C. Nuñez, I. Padilla, G. Palma, L. Parker, M. Petroff, R. Reeves, C. Reintsema, K. Rostem, M. Sagliocca, K. U-Yen, D. Valle, B. Wang, Q. Wang, D. Watts, J. Weiland, E. Wollack, Z. Xu, Z. Yan, and L. Zeng (2018). "Design and characterization of the Cosmology Large Angular Scale Surveyor (CLASS) 93 GHz focal plane". In: *Millimeter, Submillimeter, and Far-Infrared Detectors and Instrumentation for Astronomy IX*. Vol. 10708. Proc. SPIE.

Eimer, J. R., C. L. Bennett, D. T. Chuss, T. Marriage, E. J. Wollack, and L. Zeng (2012). "The cosmology large angular scale surveyor (CLASS): 40 GHz optical design". In: *Millimeter, Submillimeter, and Far-Infrared Detectors and Instrumentation for Astronomy VI*. Vol. 8452. Proc. SPIE, p. 845220. DOI: 10.1117/12.925464. arXiv: 1211.0041 [astro-ph.IM].

Essinger-Hileman, T., A. Ali, M. Amiri, J. W. Appel, D. Araujo, C. L. Bennett, F. Boone, M. Chan, H.-M. Cho, D. T. Chuss, F. Colazo, E. Crowe, K. Denis, R. Dünner, J. Eimer, D. Gothe, M. Halpern, K. Harrington, G. C. Hilton, G. F. Hinshaw, C. Huang, K. Irwin, G. Jones, J. Karakla, A. J. Kogut, D. Larson, M. Limon, L. Lowry, T. Marriage, N. Mehrle, A. D. Miller, N. Miller, S. H. Moseley, G. Novak, C. Reintsema, K. Rostem, T. Stevenson, D. Towner, K. U-Yen, E. Wagner, D. Watts, E. J. Wollack, Z. Xu, and L. Zeng (2014). "CLASS: the cosmology large angular scale surveyor". In: *Society of Photo-Optical Instrumentation Engineers (SPIE) Conference Series*. Vol. 9153. Society of Photo-Optical Instrumentation Engineers (SPIE) Conference Series, p. 1. DOI: 10.1117/12.2056701. arXiv: 1408.4788 [astro-ph.IM].

Feldman, G. J., J. Hartnell, and T. Kobayashi (2013). "Long-baseline neutrino oscillation experiments". In: *Adv. High Energy Phys.* 2013, p. 475749. DOI: 10.1155/2013/475749. arXiv: 1210.1778 [hep-ex].

Goldsmith, P. (1998). *Quasioptical Systems*. IEEE Press.

Guth, A. H. (1981). "Inflationary universe: A possible solution to the horizon and flatness problems". In: Phys. Rev. D 23, pp. 347–356. DOI: 10.1103/PhysRevD.23.347.

Halpern, M., H. P. Gush, E. Wishnow, and V. de Cosmo (1986). "Far infrared transmission of dielectrics at cryogenic and room temperatures - Glass, Fluorogold, Eccosorb, Stycast, and various plastics". In: Appl. Opt. 25, pp. 565–570. DOI: 10.1364/AO.25.000565.

Hanson, D., S. Hoover, A. Crites, P. A. R. Ade, K. A. Aird, J. E. Austermann, J. A. Beall, A. N. Bender, B. A. Benson, L. E. Bleem, J. J. Bock, J. E. Carlstrom, C. L. Chang, H. C. Chiang, H.-M. Cho, A. Conley, T. M. Crawford, T. de Haan, M. A. Dobbs, W. Everett, J. Gallicchio, J. Gao, E. M. George, N. W. Halverson, N. Harrington, J. W. Henning, G. C. Hilton, G. P. Holder, W. L. Holzapfel, J. D. Hrubes, N. Huang,

J. Hubmayr, K. D. Irwin, R. Keisler, L. Knox, A. T. Lee, E. Leitch, D. Li, C. Liang, D. Luong-Van, G. Marsden, J. J. McMahon, J. Mehl, S. S. Meyer, L. Mocanu, T. E. Montroy, T. Natoli, J. P. Nibarger, V. Novosad, S. Padin, C. Pryke, C. L. Reichardt, J. E. Ruhl, B. R. Saliwanchik, J. T. Sayre, K. K. Schaffer, B. Schulz, G. Smecher, A. A. Stark, K. T. Story, C. Tucker, K. Vanderlinde, J. D. Vieira, M. P. Viero, G. Wang, V. Yefremenko, O. Zahn, and M. Zemcov (2013). "Detection of B-Mode Polarization in the Cosmic Microwave Background with Data from the South Pole Telescope". In: *Physical Review Letters* 111.14, 141301, p. 141301. DOI: 10.1103/PhysRevLett.111.141301. arXiv: 1307.5830 [astro-ph.CO].

Harrington, K., J. Eimer, D. T. Chuss, M. Petroff, J. Cleary, M. DeGeorge, T. W. Grunberg, A. Ali, J. W. Appel, C. L. Bennett, M. Brewer, R. Bustos, M. Chan, J. Couto, S. Dahal, K. Denis, R. Dünner, T. Essinger-Hileman, P. Fluxa, M. Halpern, G. Hilton, G. F. Hinshaw, J. Hubmayr, J. Iuliano, J. Karakla, T. Marriage, J. McMahon, N. T. Miller, C. Nuñez, I. L. Padilla, G. Palma, L. Parker, B. Pradenas, R. Reeves, C. Reintsema, K. Rostem, D. Valle, T. Van Engelhoven, B. Wang, Q. Wang, D. Watts, J. Weiland, E. Wollack, Z. Xu, Z. Yan, and L. Zeng (2018). "Variable-delay Polarization Modulators for the for the CLASS Telescopes". In: *Millimeter, Submillimeter, and Far-Infrared Detectors and Instrumentation for Astronomy IX*. Vol. 10708. Proc. SPIE, pp. 10708–92.

Harrington, K., T. Marriage, A. Ali, J. W. Appel, C. L. Bennett, F. Boone, M. Brewer, M. Chan, D. T. Chuss, F. Colazo, S. Dahal, K. Denis, R. Dünner, J. Eimer, T. Essinger-Hileman, P. Fluxa, M. Halpern, G. Hilton, G. F. Hinshaw, J. Hubmayr, J. Iuliano, J. Karakla, J. McMahon, N. T. Miller, S. H. Moseley, G. Palma, L. Parker, M. Petroff, B. Pradenas, K. Rostem, M. Sagliocca, D. Valle, D. Watts, E. Wollack, Z. Xu, and L. Zeng (2016). "The Cosmology Large Angular Scale Surveyor". In: *Millimeter, Submillimeter, and Far-Infrared Detectors and Instrumentation for Astronomy VIII*. Vol. 9914. Proc. SPIE, 99141K. DOI: 10.1117/12.2233125. arXiv: 1608.08234 [astro-ph.IM].

Hinshaw, G., D. Larson, E. Komatsu, D. N. Spergel, C. L. Bennett, J. Dunkley, M. R. Nolta, M. Halpern, R. S. Hill, N. Odegard, L. Page, K. M. Smith, J. L. Weiland, B. Gold, N. Jarosik, A. Kogut, M. Limon, S. S. Meyer, G. S. Tucker, E. Wollack, and E. L. Wright (2013). "Nine-year Wilkinson Microwave Anisotropy Probe (WMAP) Observations: Cosmological Parameter Results". In: ApJS 208, 19, p. 19. DOI: 10.1088/0067-0049/208/2/19. arXiv: 1212.5226.

Howell, L. L., S. P. Magleby, and B. M. Olsen (2013). *Handbook of Compliant Mechanisms*. 1st ed. John Wiely & Sons Ltd.

Hu, W. and S. Dodelson (2002). "Cosmic Microwave Background Anisotropies". In: ARA&A 40, pp. 171–216. DOI: 10.1146/annurev.astro.40.060401.093926. eprint: astro-ph/0110414.

Hu, W. and M. White (1997). "A CMB polarization primer". In: New A 2, pp. 323–344. DOI: 10.1016/S1384-1076(97)00022-5. eprint: astro-ph/9706147.

Irwin, K. D., L. R. Vale, N. E. Bergren, S. Deiker, E. N. Grossman, G. C. Hilton, S. W. Nam, C. D. Reintsema, D. A. Rudman, and M. E. Huber (2002). "Time-division SQUID multiplexers". In: *Low Temperature Detectors* 605, pp. 301–304. DOI: 10.1063/1.1457650.

Keisler, R., S. Hoover, N. Harrington, J. W. Henning, P. A. R. Ade, K. A. Aird, J. E. Austermann, J. A. Beall, A. N. Bender, B. A. Benson, L. E. Bleem, J. E. Carlstrom, C. L. Chang, H. C. Chiang, H.-M. Cho, R. Citron, T. M. Crawford, A. T. Crites, T. de Haan, M. A. Dobbs, W. Everett, J. Gallicchio, J. Gao, E. M. George, A. Gilbert, N. W. Halverson, D. Hanson, G. C. Hilton, G. P. Holder, W. L. Holzapfel, Z. Hou, J. D. Hrubes, N. Huang, J. Hubmayr, K. D. Irwin, L. Knox, A. T. Lee, E. M. Leitch, D. Li, D. Luong-Van, D. P. Marrone, J. J. McMahon, J. Mehl, S. S. Meyer, L. Mocanu, T. Natoli, J. P. Nibarger, V. Novosad, S. Padin, C. Pryke, C. L. Reichardt, J. E. Ruhl, B. R. Saliwanchik, J. T. Sayre, K. K. Schaffer, E. Shirokoff, G. Smecher, A. A. Stark, K. T. Story, C. Tucker, K. Vanderlinde, J. D. Vieira, G. Wang, N. Whitehorn, V. Yefremenko, and O. Zahn (2015). "Measurements of Sub-degree B-mode Polarization in the Cosmic Microwave Background from 100 Square Degrees of SPTpol Data". In: ApJ 807, 151, p. 151. DOI: 10.1088/0004-637X/807/2/151. arXiv: 1503.02315.

Kovac, J. M., E. M. Leitch, C. Pryke, J. E. Carlstrom, N. W. Halverson, and W. L. Holzapfel (2002). "Detection of polarization in the cosmic microwave background using DASI". In: Nature 420, pp. 772–787. DOI: 10.1038/nature01269. eprint: astro-ph/0209478.

Krejny, M., D. Chuss, C. D. D'Aubigny, D. Golish, M. Houde, H. Hui, C. Kulesa, R. F. Loewenstein, S. H. Moseley, G. Novak, G. Voellmer, C. Walker, and E. Wollack (2008). "The Hertz/VPM polarimeter: design and first light observations". In: Appl. Opt. 47, p. 4429. DOI: 10.1364/AO.47.004429. arXiv: 0803.3759.

Lamb, James W. (1996). "Miscellaneous Data on Materials for Millimetre and Submillimetre Optics". In: *Int. J. IR and Millimeter Waves* 17.12.

Linde, A. D. (1982). "A new inflationary universe scenario: A possible solution of the horizon, flatness, homogeneity, isotropy and primordial monopole problems". In: *Physics Letters B* 108, pp. 389–393. DOI: 10.1016/0370-2693(82)91219-9.

Liu, A., J. R. Pritchard, R. Allison, A. R. Parsons, U. Seljak, and B. D. Sherwin (2016). "Eliminating the optical depth nuisance from the CMB with 21 cm cosmology". In: Phys. Rev. D 93.4, 043013, p. 043013. DOI: 10.1103/PhysRevD.93.043013. arXiv: 1509.08463.

Ludwig, A. C. (1973). "The definition of cross polarization." In: *IEEE Transactions on Antennas and Propagation* 21, pp. 116–119.

Marcuvitz, N., ed. (1951). *Waveguide Handbook*. New York: McGraw-Hil.

Mather, J. C., E. S. Cheng, R. E. Eplee Jr., R. B. Isaacman, S. S. Meyer, R. A. Shafer, R. Weiss, E. L. Wright, C. L. Bennett, N. W. Boggess, E. Dwek, S. Gulkis, M. G. Hauser, M. Janssen, T. Kelsall, P. M. Lubin, S. H. Moseley Jr., T. L. Murdock, R. F. Silverberg,

G. F. Smoot, and D. T. Wilkinson (1990). "A preliminary measurement of the cosmic microwave background spectrum by the Cosmic Background Explorer (COBE) satellite". In: ApJ 354, pp. L37–L40. DOI: 10.1086/185717.

Miller, N. J., D. T. Chuss, T. A. Marriage, E. J. Wollack, J. W. Appel, C. L. Bennett, J. Eimer, T. Essinger-Hileman, D. J. Fixsen, K. Harrington, S. H. Moseley, K. Rostem, E. R. Switzer, and D. J. Watts (2016). "Recovery of Large Angular Scale CMB Polarization for Instruments Employing Variable-delay Polarization Modulators". In: ApJ 818, 151, p. 151. DOI: 10.3847/0004-637X/818/2/151. arXiv: 1509.04628 [astro-ph.IM].

Naess, S., M. Hasselfield, J. McMahon, M. D. Niemack, G. E. Addison, P. A. R. Ade, R. Allison, M. Amiri, N. Battaglia, J. A. Beall, F. de Bernardis, J. R. Bond, J. Britton, E. Calabrese, H.-m. Cho, K. Coughlin, D. Crichton, S. Das, R. Datta, M. J. Devlin, S. R. Dicker, J. Dunkley, R. Dünner, J. W. Fowler, A. E. Fox, P. Gallardo, E. Grace, M. Gralla, A. Hajian, M. Halpern, S. Henderson, J. C. Hill, G. C. Hilton, M. Hilton, A. D. Hincks, R. Hlozek, P. Ho, J. Hubmayr, K. M. Huffenberger, J. P. Hughes, L. Infante, K. Irwin, R. Jackson, S. Muya Kasanda, J. Klein, B. Koopman, A. Kosowsky, D. Li, T. Louis, M. Lungu, M. Madhavacheril, T. A. Marriage, L. Maurin, F. Menanteau, K. Moodley, C. Munson, L. Newburgh, J. Nibarger, M. R. Nolta, L. A. Page, C. Pappas, B. Partridge, F. Rojas, B. L. Schmitt, N. Sehgal, B. D. Sherwin, J. Sievers, S. Simon, D. N. Spergel, S. T. Staggs, E. R. Switzer, R. Thornton, H. Trac, C. Tucker, M. Uehara, A. Van Engelen, J. T. Ward, and E. J. Wollack (2014). "The Atacama Cosmology Telescope: CMB polarization at $200 < \ell < 9000$". In: J. Cosmology Astropart. Phys. 10, 007, p. 7. DOI: 10.1088/1475-7516/2014/10/007. arXiv: 1405.5524.

Novak, G., J. L. Sundwall, and R. J. Pernic (1989). "Far infrared polarizing grids for use at cryogenic temperatures". In: Appl. Opt. 28, pp. 3425–3427. DOI: 10.1364/AO.28.003425.

Planck Collaboration et al. (2016a). "Planck 2015 results. I. Overview of products and scientific results". In: A&A 594, A1, A1. DOI: 10.1051/0004-6361/201527101.

Planck Collaboration et al. (2016b). "Planck 2015 results. X. Diffuse component separation: Foreground maps". In: A&A 594, A10, A10. DOI: 10.1051/0004-6361/201525967.

Planck Collaboration et al. (2016c). "Planck 2015 results. XIII. Cosmological parameters". In: A&A 594, A13, A13. DOI: 10.1051/0004-6361/201525830.

Planck Collaboration et al. (2016d). "Planck 2015 results. XXIV. Cosmology from Sunyaev-Zeldovich cluster counts". In: A&A 594, A24, A24. DOI: 10.1051/0004-6361/201525833.

Planck Collaboration et al. (2016e). "Planck intermediate results. XLVI. Reduction of large-scale systematic effects in HFI polarization maps and estimation of the reionization optical depth". In: A&A 596, A107, A107. DOI: 10.1051/0004-6361/201628890. arXiv: 1605.02985.

Planck Collaboration et al. (2016f). "Planck intermediate results. XLVII. Planck constraints on reionization history". In: A&A 596, A108, A108. DOI: 10.1051/0004-6361/201628897. arXiv: 1605.03507.

Polarbear Collaboration, P. A. R. Ade, Y. Akiba, A. E. Anthony, K. Arnold, M. Atlas, D. Barron, D. Boettger, J. Borrill, S. Chapman, Y. Chinone, M. Dobbs, T. Elleflot, J. Errard, G. Fabbian, C. Feng, D. Flanigan, A. Gilbert, W. Grainger, N. W. Halverson, M. Hasegawa, K. Hattori, M. Hazumi, W. L. Holzapfel, Y. Hori, J. Howard, P. Hyland, Y. Inoue, G. C. Jaehnig, A. H. Jaffe, B. Keating, Z. Kermish, R. Keskitalo, T. Kisner, M. Le Jeune, A. T. Lee, E. M. Leitch, E. Linder, M. Lungu, F. Matsuda, T. Matsumura, X. Meng, N. J. Miller, H. Morii, S. Moyerman, M. J. Myers, M. Navaroli, H. Nishino, A. Orlando, H. Paar, J. Peloton, D. Poletti, E. Quealy, G. Rebeiz, C. L. Reichardt, P. L. Richards, C. Ross, I. Schanning, D. E. Schenck, B. D. Sherwin, A. Shimizu, C. Shimmin, M. Shimon, P. Siritanasak, G. Smecher, H. Spieler, N. Stebor, B. Steinbach, R. Stompor, A. Suzuki, S. Takakura, T. Tomaru, B. Wilson, A. Yadav, and O. Zahn (2014). "A Measurement of the Cosmic Microwave Background B-mode Polarization Power Spectrum at Sub-degree Scales with POLARBEAR". In: ApJ 794, 171, p. 171. DOI: 10.1088/0004-637X/794/2/171. arXiv: 1403.2369.

Pozar, David M. (2012). *Microwave Engineering*. 4th ed. John Wiley & Sons, Inc.

Riess, A. G., L. M. Macri, S. L. Hoffmann, D. Scolnic, S. Casertano, A. V. Filippenko, B. E. Tucker, M. J. Reid, D. O. Jones, J. M. Silverman, R. Chornock, P. Challis, W. Yuan, P. J. Brown, and R. J. Foley (2016). "A 2.4% Determination of the Local Value of the Hubble Constant". In: ApJ 826, 56, p. 56. DOI: 10.3847/0004-637X/826/1/56. arXiv: 1604.01424.

Rostem, K., A. Ali, J. W. Appel, C. L. Bennett, A. Brown, M.-P. Chang, D. T. Chuss, F. A. Colazo, N. Costen, K. L. Denis, T. Essinger-Hileman, R. Hu, T. A. Marriage, S. H. Moseley, T. R. Stevenson, K. U-Yen, E. J. Wollack, and Z. Xu (2016). "Silicon-based antenna-coupled polarization-sensitive millimeter-wave bolometer arrays for cosmic microwave background instruments". In: *Millimeter, Submillimeter, and Far-Infrared Detectors and Instrumentation for Astronomy VIII*. Vol. 9914. Proc. SPIE, p. 99140D. DOI: 10.1117/12.2234308. arXiv: 1608.08891 [astro-ph.IM].

The Astropy Collaboration et al. (2018). "The Astropy Project: Building an inclusive, open-science project and status of the v2.0 core package". In: *ArXiv e-prints*. arXiv: 1801.02634 [astro-ph.IM].

Voellmer, G. M., C. Bennett, D. T. Chuss, J. Eimer, H. Hui, S. H. Moseley, G. Novak, E. J. Wollack, and L. Zeng (2008). "A large free-standing wire grid for microwave variable-delay polarization modulation". In: *Ground-based and Airborne Instrumentation for Astronomy II*. Vol. 7014. Proc. SPIE, 70142A. DOI: 10.1117/12.787979.

Watts, D. J., D. Larson, T. A. Marriage, M. H. Abitbol, J. W. Appel, C. L. Bennett, D. T. Chuss, J. R. Eimer, T. Essinger-Hileman, N. J. Miller, K. Rostem, and E. J. Wollack (2015). "Measuring the Largest Angular Scale CMB B-mode Polarization with

Galactic Foregrounds on a Cut Sky". In: ApJ 814, 103, p. 103. DOI: 10.1088/0004-637X/814/2/103. arXiv: 1508.00017.

Watts, D. J., B. Wang, A. Ali, J. W. Appel, C. L. Bennett, D. T. Chuss, S. Dahal, J. R. Eimer, T. Essinger-Hileman, K. Harrington, G. Hinshaw, J. Iuliano, T. A. Marriage, N. J. Miller, I. L. Padilla, M. Petroff, K. Rostem, E. J. Wollack, and Z. Xu (2018). "A Projected Estimate of the Reionization Optical Depth Using the CLASS Experiment's Sample-Variance Limited E-Mode Measurement". In: *ArXiv e-prints*. arXiv: 1801.01481.

Weinberg, S (2008). *Cosmology*. Oxford University Press.

Yun, Garam, Karlton Crabtree, and Russell A. Chipman (2011a). "Three-dimensional polarization ray-tracing calculus I: definition and diattenuation". In: *Appl. Opt.* 50.18, pp. 2855–2865. DOI: 10.1364/AO.50.002855. URL: http://ao.osa.org/abstract.cfm?URI=ao-50-18-2855.

Yun, Garam, Stephen C. McClain, and Russell A. Chipman (2011b). "Three-dimensional polarization ray-tracing calculus II: retardance". In: *Appl. Opt.* 50.18, pp. 2866–2874. DOI: 10.1364/AO.50.002866. URL: http://ao.osa.org/abstract.cfm?URI=ao-50-18-2866.

Kathleen (Katie) Harrington

Bloomberg 251, 3400 N. Charles St , Baltimore, MD 21218, kharrington@jhu.edu, (859) 433-7381

Education

Johns Hopkins University — *Baltimore, MD*
Ph.D., Physics and Astronomy — July 2018
M.A., Physics and Astronomy — May 2014

Massachusetts Institute of Technology — *Cambridge, MA*
B.S., Physics — June 2012

Fellowships and Awards

NASA Space Technology Research Fellowship — 2014 - 2018

Rowland Research Fellowship — 2012 - 2013

Thomas J. Watson Memorial Scholarship — 2008 - 2012

National Merit Scholarship Recipient — 2008

Research Experience

Cosmology Large Angular Scale Surveyor — 2012 - Present
Graduate Researcher, Advisor: Tobias Marriage — *Baltimore, MD*
– Designed, assembled, and fielded the CLASS variable-delay polarization modulators (VPMs) novel front-end, microwave polarization modulators uniquely suited to facilitate the recovery of faint polarization signals across the full sky.
– Designed and manufactured simulated dielectric anti-reflection coatings for the CLASS plastic cryogenic optics.
– Built automated daily and weekly data status monitors to consolidate observation information and quickly detect telescope changes.

MIT Junior Lab — 2011 - 2012
Lab Assistant — *Cambridge, MA*
– Rebuilt 21 cm radio telescope to ensure operation, on campus, around strong radio sources and created an entirely new motion control system for an old radio antenna mount.

MINICLEAN Collaboration — 2011 - 2012
Undergraduate Thesis, Advisor: J. Formaggio — *Cambridge, MA*
– Thesis on perfecting the expected neutron background for the MINICLEAN Liquid Argon WIMP detector. Used Monte Carlo simulations to investigate discrepancies in the neutron-argon scattering cross sections in G4NDL3.13 and ENDF/B-VII.

Skills

Python, Java, ROOT, C, C++, GEANT4, LaTeX, MATLAB, SQL, Mathematica, Machining, CNC Machining, Solidworks, Electronics, Soldering, Arduino Microcontrollers Zeemax, HFSS

Community Service/Leadership

Graduate Representative Organization Summer Sports Coordinator — 2017

Physics and Astronomy Intramural Softball Captain — 2016 - 2017

JHU Physics and Astronomy Student Machine Shop Committee 2014 - Present

Clash of Clans (video game), Clan Leader, Reddit Clan System Council 2014 - Present

– Lead 2 global teams of ~ 90 players. Organize matches with other teams, moderate disagreements, and manage administrative positions within the team.

– Member of administrative council for the largest English-speaking clan system in the world, comprising ~ 50 teams and ~ 2500 people. Organize tournaments and events across the entire system.

JHU PAGS Diversity Committee 2014 - 2016

Community Service/Leadership cont.

JHU PAGS Outreach 2012 - Present

Vice President, 2014 - 2015

– Led construction of two portable World Wide Telescope Planetariums for shows at Southwest Baltimore Charter School, STEM Achievement in Baltimore City Schools (SABES) events, Roots and Branches School, and JHU Physics and Astronomy department.

– Regularly visited Baltimore Talent Development High School to give demos of physics concepts

Varsity Softball, MIT 2008 - 2012
Captain, 2012

Teaching and Advising

JHU CLASS Lab 2012 - Present
Advised and oversaw 5 undergraduate and 3 graduate students on various semester and year-long projects.

MIT Junior Lab, Undergraduate Teaching Assistant 2011 - 2012
Helped students perform experiments and advised them on analysis methods

Conferences and Talks

"Variable-delay Polarization Modulators for the CLASS telescopes," Poster delivered at SPIE Astronomical Telescopes and Instrumentation Conference, June 2018

"Variable-delay Polarization Modulators for the CLASS telescopes," Talk delivered at American Astronomical Society's (AAS) Winter Meeting, January 2018

"Variable-delay Polarization Modulators for the CLASS telescopes," Poster delivered at American Astronomical Society's (AAS) Winter Meeting, January 2017

"The Cosmology Large Angular Scale Surveyor," Presentation delivered at SPIE Astronomical Telescopes and Instrumentation Conference, July 2016

"The Cosmology Large Angular Scale Surveyor," Talk for JHU Center for Astrophysical Sciences' Wine and Cheese Seminar, March 2015

"Cosmology Large Angular Scale Surveyor: Instrument Overview," Poster delivered at Cosmology with the CMB and its Polarization Conference, January 2015

"The Cosmology Large Angular Scale Surveyor," Presentation at JHU - NASA Goddard Space Flight Center Integration Day, November 2014

"Variable-delay Polarization Modulators for the CLASS telescopes," Poster delivered at AAS Winter Meeting, January 2014

Publications

9 D. J. Watts, B. Wang, A. Ali, J. W. Appel, C. L. Bennett, D. T. Chuss, S. Dahal, J. R. Eimer, T. Essinger-Hileman, **K. Harrington**, G. Hinshaw, J. Iuliano, T. A. Marriage, N. J. Miller, I. L. Padilla, M. Petroff, K. Rostem, E. J. Wollack, and Z. Xu, A Projected Estimate of the Reionization Optical Depth Using the CLASS Experiment's Sample-Variance Limited E-Mode Measurement. Accepted by ApJ, Aug. 2018.

8 **K. Harrington**, J. Eimer, D. T. Chuss, M. Petroff, J. Cleary, M. DeGeorge, T. W. Grunberg, A. Ali, J. W. Appel, C. L. Bennett, M. Brewer, R. Bustos, M. Chan, J. Couto, S. Dahal, K. Denis, R. Dünner, T. Essinger-Hileman, P. Fluxa, M. Halpern, G. Hilton, G. F. Hinshaw, J. Hubmayr, J. Iuliano, J. Karakla, T. A. Marriage, B. P. Márquez, J. J. McMahon, N. T. Miller, C. Nuñez, I. L. Padilla, G. Palma, L. Parker, R. Reeves, C. Reintsema, K. Rostem, D. A. N. Valle, T. Van Engelhoven, B. Wang, Q. Wang, D. J, Watts, J. Weiland, E. J. Wollack, Z. Xu, Z. Yan, and L. Zeng. Variable-delay Polarization Modulators for the for the CLASS Telescopes. In *Millimeter, Submillimeter, and Far-Infrared Detectors and Instrumentation for Astronomy IX*, volume 10708 of Proc. SPIE. page 10708-92. Jun 2018.

7 J. Iuliano, J. Eimer, L. Parker, A. Ali, J. W. Appel, C. L. Bennett, M. Brewer, R. Bustos, D. T. Chuss, J. Cleary, J. Couto, S. Dahal, K. Denis, R. Dünner, T. Essinger-Hileman, P. Fluxa, M. Halpern, **K. Harrington**, K. Helson, G. Hilton, G. Hinshaw, J. Hubmayr, J. Karakla, T. A. Marriage, B. P. Márquez, N. J. Miller, J. J, McMahon, C. Nuñez, I. L. Padilla, G. Palma, M. Petroff, R. Reeves, C. Reintsema, K. Rostem, D. A. N. Valle, T. Van Engelhoven, B. Wang, Q. Wang, D. J. Watts, J. Weiland, E. J. Wollack, Z. Xu, Z. Yan, and L. Zeng. The Cosmology Large Angular Scale Surveyor Receiver Design. In *Millimeter, Submillimeter, and Far-Infrared Detectors and Instrumentation for Astronomy IX*, volume 10708 of Proc. SPIE. Jun 2018.

6 S. Dahal, A. Ali, J. W. Appel, T. Essinger-Hileman, C. L. Bennett, M. Brewer, R. Bustos, M. Chan, D. T. Chuss, J. Cleary, F. Colazo, J. Couto, K. Denis, R. Dünner, J. Eimer, P. Fluxa, M. Halpern, **K. Harrington**, K. Helson, G. Hilton, G. F. Hinshaw, J. Hubmayr, J. Iuliano, J. Karakla, B. P. Márquez, T. A. Marriage, J. J. McMahon, N. T. Miller, C. Nuñez, I. L. Padilla, G. Palma, L. Parker, M. Petroff, R. Reeves, C. Reintsema, K. Rostem, M. Sagliocca, K. U-Yen, D. A. N. Valle, T. Van Engelhoven, B. Wang, Q. Wang, D. J. Watts, J. Weiland, E. J. Wollack, Z. Xu, Z. Yan, and L. Zeng. Design and characterization of the Cosmology Large Angular Scale Surveyor (CLASS) 93 GHz focal plane. In *Millimeter, Submillimeter, and Far-Infrared Detectors and Instrumentation for Astronomy IX*, volume 10708 of Proc. SPIE. Jun 2018.

5 D. T. Chuss, A. Ali, M. Amiri, J. W. Appel, C. L. Bennett, F. Colazo, K. L. Denis, R. Dünner, T. Essinger-Hileman, J. Eimer, P. Fluxa, D. Gothe, M. Halpern, **K. Harrington**, G. Hilton, G. Hinshaw, J. Hubmayr, J. Iuliano, T. A. Marriage, N. Miller, S. H. Moseley, G. Mumby, M. Petroff, C. Reintsema, K. Rostem, K. U-Yen, D. Watts, E. Wagner, E. J. Wollack, Z. Xu, and L. Zeng. Cosmology Large Angular Scale Surveyor (CLASS) Focal Plane Development. Journal of Low Temperature Physics, Volume 184, Issue 3-4, pp. 759-764, Aug. 2016

4 **K. Harrington**, T. A. Marriage, A. Ali, J. W. Appel, C. L. Bennett, F. Boone, M. Brewer, M. Chan, D. T. Chuss, F. Colazo, S. Dahal, K. Denis, R. Dunner, J. Eimer, T. Essinger-Hileman, P. Fluxa, M. Halpern, G. Hilton, G. F. Hinshaw, J. Hubmayr, J. Iuliano, J. Karakla, J. McMahon, N. T. Miller, S. H. Moseley, G. Palma, L. Parker, M. Petroff, B. Pradenas, K. Rostem, M. Sagliocca, D. Valle, D. Watts, E. Wollack, Z. Xu, and L. Zeng. The Cosmology Large Angular Scale Surveyor. In *Millimeter, Submillimeter, and Far-Infrared Detectors and Instrumentation for Astronomy VIII*, volume 9914 of Proc. SPIE, page 99141K, July 2016.

3 N. J. Miller, D. T. Chuss, T. A. Marriage, E. J. Wollack, J.W. Appel, C. L. Bennett, J. R. Eimer, T. Essinger-Hileman, D. J Fixsen, **K. Harrington**, S. H. Moseley, K. Rostem,

E. R. Switzer, and D. J. Watts. Recovery of Large Angular Scale CMB Polarization for Instruments Employing Variable-delay Polarization Modulators. ApJ, 818:151, February 2016.

2 J. W. Appel, A. Ali, M. Amiri, D. Araujo, C. L. Bennet, F. Boone, M. Chan, H.-M. Cho, D. T. Chuss, F. Colazo, E. Crowe, K. Denis, R. Dunner, J. Eimer, T. Essinger-Hileman, D. Gothe, M. Halpern, **K. Harrington**, G. Hilton, G. F. Hinshaw, C. Huang, K. Irwin, G. Jones, J. Karakula, A. J. Kogut, D. Larson, M. Limon, L. Lowry, T. Marriage, N. Mehrle, A. D. Miller, N. Miller, S. H. Moseley, G. Novak, C. Reintsema, K. Rostem, T. Stevenson, D. Towner, K. U-Yen, E. Wagner, D. Watts, E. Wollack, Z. Xu, and L. Zeng. The cosmology large angular scale surveyor (CLASS): 38-GHz detector array of bolometric polarimeters. In *Society of Photo-Optical Instrumentation Engineers (SPIE) Conference Series*, volume 9153 of *Society of Photo-Optical Instrumentation Engineers (SPIE) Conference Series*, page 1, July 2014.

1 T. Essinger-Hileman, A. Ali, M. Amiri, J.W. Appel, D. Araujo, C. L. Bennett, F. Boone, M. Chan, H.-M. Cho, D. T. Chuss, F. Colazo, E. Crowe, K. Denis, R. Dunner, J. Eimer, D. Gothe, M. Halpern, **K. Harrington**, G. C. Hilton, G. F. Hinshaw, C. Huang, K. Irwin, G. Jones, J. Karakla, A. J. Kogut, D. Larson, M. Limon, L. Lowry, T. Marriage, N. Mehrle, A. D. Miller, N. Miller, S. H. Moseley, G. Novak, C. Reintsema, K. Rostem, T. Stevenson, D. Towner, K. UYen, E. Wagner, D. Watts, E. J. Wollack, Z. Xu, and L. Zeng. CLASS: the cosmology large angular scale surveyor. In *Society of Photo-Optical Instrumentation Engineers (SPIE) Conference Series*, volume 9153 of *Society of Photo-Optical Instrumentation Engineers (SPIE) Conference Series*, page 1, July 2014.